# ADVANCING FIELD EMISSION TECHNOLOGY FOR HIGH POWER INJECTORS OPERATING IN GHZ AND BEYOND

By

Mitchell E. Schneider

# A DISSERTATION

Submitted to
Michigan State University
in partial fulfillment of the requirements
for the degree of

Electrical Engineering—Doctor of Philosophy Physics—Dual Major

2022

#### **ABSTRACT**

# ADVANCING FIELD EMISSION TECHNOLOGY FOR HIGH POWER INJECTORS OPERATING IN GHZ AND BEYOND

By

#### Mitchell E. Schneider

As the next generation of electron injectors pushes to achieve higher gradient fields than ever before (>300 MV/m), they are driven to operate at higher frequencies (C-band through W-band). This shrinks the fabrication dimensions of these cavities, making field emission cathodes (FECs) an electron source of choice. Photoemission and thermionic sources are increasingly less suited as the complex laser transport schemes and heating source powering these injectors cannot provide the necessary beam quality and may cause damage to the cathode or the injector itself. Carbon-based FECs have dominated the field emission sources R&D portfolio at DOD and DOE for the past 30 years across various high-power vacuum electronic device activities. Compared to traditional metal cathode technology, carbon-based technology cathodes are able to produce higher charge at low electric fields. Small intrinsic electron momentum and simple fabrication means these can become a leading technology, e.g., in the case of carbon nanotubes, nanoscale emitters make them attractive for producing high brightness beams. Specifically, diamond-based cathodes can handle extreme temperature and mechanical stresses that can occur under high gradient conditions.

Most promising is a unique form of diamond, ultra-nano-crystalline diamond (UNCD) due to its material and electrical properties, which include being the most conductive form of diamond due to having the largest amount of grain boundaries. This cathode material allows us to explore new frontiers of cathode physics research, revealing a new field emission mechanism that diverges from classical Fowler Nordheim, termed space charge dominated Fowler Nordheim. This form of

Fowler Nordheim is space charge dominated but can surpass the 1D Child Langmuir limit and approaches the 2D limit. This is not space charge limited Fowler Nordheim. This ability to decouple the extracted current from the space charge effects allows for the production of extremely bright beams. This can be achieved by expanding the current cathode testing facilities beyond L band into C band so as to access these high fields and explore the temporal dynamics of a field emission source. This will yield the new physics knowledge needed to construct the world's first custom-built injector specifically designed for field emission sources.

Furthermore, exploring other forms of diamond cathode such as Diamond Field Emitter Arrays (DFEA) yields insight into the applications of transversely shaped beams for advanced accelerator applications such as emittance exchange beam lines. DFEA's allow for the exploration of additional materials effects on the cathode performance such as the ballast resistance. This ultimately allows the derivation of a comprehensive concept map for the field emission dynamic regimes needed for the design of RF injectors. Previously, the theoretical assumption was that everything operated under classical Fowler Nordheim without any additional contributions from other materials properties or beam effects.

This thesis is dedicated to my late father and grandfather Michael E. Schneider and Richard L. Tock

#### **ACKNOWLEDGMENTS**

I would like to acknowledge that this work would not be possible without the support of my team, not only at Michigan State, but also around the country at various national laboratories, in particular Argonne National Laboratory, Los Alamos National laboratory, and SLAC National Accelerator Facility. Above all else, I would like to thank my undergraduate research assistant, Emily Jevarjian, who has truly been my second in command, a great support through this project in all aspects and a great friend. I am pleased to say that I look forward to being on her thesis committee as she continues on her doctorate as a follow-on to this research. Other members that I would like to include are Benjamin Sims, Tanvi Nikhar, Taha Posos, and Ryan Fleming.

Beyond my team, I would also like to acknowledge the national laboratory mentors that gave me the skills and knowledge that I needed to succeed. Their mentoring guidance and support throughout these 3 ½ years is greatly appreciated and cannot be expressed easily in words. I would like to extend my greatest gratitude to Jiahang Shao, Emilio Nanni, Sami Tantawi, Valery Dolgashev, Jenya Simakov, and John Lewellen.

Last but not least, I would like to thank all the time and effort that my advisor gave to me. Without Sergey Baryshev I would not be the person I am today. Sergey now enters my grateful list of mentors who got me to this point which started as a student with disability. It took a lot to get to this end and I am grateful for the people who cared throughout high school, undergraduate, undergraduate research at the Air Force Institute of Technology and the loving support of my family.

# TABLE OF CONTENTS

LIST OF FIGURES	viii
CHAPTER 1 INTRODUCTION	1
1.1 Next Generation Injector Technology	
1.1.1 Introduction to field emission theory	
1.1.2 High-frequency injectors implications of source development	
1.1.3 FEC bright beams and dark current effects	
1.2 Advancement in polycrystalline diamond fabrication technology	
REFERENCES	
CHAPTER 2 TECHNICAL RELEVANCE	22
CHAPTER 2 L-BAND CATHODE TESTING FACILITIES AND DEVELOPMENT OF	22
CATHODE CONDITIONING PROCEDURES	23
2.1 The Argonne Cathode Teststand (ACT)	
2.1.1 Optimal Conditioning Procedure	
REFERENCES	
CHAPTER 3 TECHNICAL RELEVANCE	21
CHAPTER 3 CREATION OF THE FEMASTER SERIES: A COMPREHENSIVE FIELD	54
EMISSION BEAM ANALYSIS AND MODELING TOOLKIT.	35
3.1 FEgen:	
3.1.1 Momentum Distribution	
3.1.2 Spatio-temporal Distribution	
3.1.3 Outlook modeling of non-Fowler Nordheim conditions	
3.2 FEbeam:	
3.2.1 Obtaining Q-E Curves	
3.2.2 Determining Fowler-Nordheim parameters:	
3.3 FEpic	
3.4 FEbreak	63
3.4.1 Introduction	64
3.4.2 CERF-NM facility	65
3.4.3 FPGA scope for real-time breakdown analysis	66
REFERENCES	
CHAPTER 4 TECHNICAL RELEVANCE	76
CHAPTER 4 PRODUCTION OF AMPERE-CLASS UNCD AND EVIDENCE FOR NEW	
EMISSION PHYSICS	
4.1 Ampere-Class beam and non-Fowler Nordheim conditions	
4.1.1 Section 4.1.1: Cathode Fabrication	
4.1.2 Image Processing and Beam Dynamics	
4.2 Surpassing the Child Langmuir limit and Development of the space charge dominate	
Fowler Nordheim regime	86

4.2.1 Production of bright beams	92
4.3 Effects of Geometry and Material Properties on Production of Transversely Shaped	
Beams using Diamond Field Emission Array Cathodes	94
4.3.1 Evidence for negligible role of Geometry effects on FEC performance	99
4.3.2 Materials Properties of FEC performance	. 101
APPENDICES	. 107
APPENDIX A: Processed images indicating the number of local maxima found for each	
image from FEpic	. 108
APPENDIX B: Fowler Nordheim plots, knee point decision plots, and Millikan plots	. 110
REFERENCES	. 116
CHAPTER 5 DISCUSSION: PATHWAY TOWARDS A FIELD EMISSION ACCELERAT	OR
FACILITY BEAMLINE	. 120
5.1 UNCD Cathode Engineering	. 121
5.2 Development of Field Emission Emittance Teststand	. 122
5.3 Development of next generation custom-built field emission injectors beyond L band	1123
5.4 Theoretical work beyond Fowler Nordheim	. 123
5.5 Field emission cathodes for advanced accelerator applications	. 124
REFERENCES	. 125

# LIST OF FIGURES

Figure 1.0.1 The goals of the community to build field emission injectors and the current challenges faced and resolved by this thesis (in blue).
Figure 1.1.1 diagram for the emission mechanisms comparing thermionic emission, photoemission, and field emission
Figure 1.1.2 example of a classical Fowler Nordheim plot with no deviation using the RF coordinates
Figure 1.1.3 FEC RF phase window from J. Qui and S. Baryshev, IEEE Transactions on Electron Devises 65, 1132 (2018) [15]. The IEEE does not require individuals working on a thesis to obtain a formal reuse license.
Figure 1.1.4: SLAC's 110 GHz field emission injector with a 1mm beam aperture taken from S. Lewis proceedings IPAC 2019 [20]. All JACOW conference proceedings are published under the Creative Commons Attribution 3.0 license (CC-BY 3.0) to copy and redistribute the material in any medium or format
Figure 1.2.1 UNCD cathode operated in a L-band SRF injector would turn on field at 0.6 MV/m [31]. AIP Publishing grants a license for all orders
Figure 1.2.2 copper normal conducting X-band injector with cathode plug and field map using a UNCD field emission cathode [33]. The IEEE does not require individuals working on a thesis to obtain a formal reuse license
Figure 1.2.3 SEM images showing the relative grain size between different forms of polycrystalline diamond being that of micro, nano, and UNCD from [34]. Ability to reprint figure under the license number <b>5192220196519.</b>
Figure 1.2.4 DFEA growth process [37]. All JACOW conference proceedings are published under the Creative Commons Attribution 3.0 license (CC-BY 3.0) to copy and redistribute the material in any medium or format
Figure 1.2.5 Diagram of the UNCD growth chamber used at Michigan State University and the Fraunhofer Institute [38]. This figure has been approved to be reprinted in accordance with approval from the author Tanvi Nikhar MS.
Figure 2.1.1 (a) transverse cross-sectional photo of ACT gun showing the beam aperture and the cathode holder. Photo was taken before brazing the two sections of the cavity into one part. (b) shows a longitudinal cross-section of the 3D model of the ACT gun [1]. Ability to reprint figure under the license number <b>5192550991050</b> .
Figure 2.1.2 E field map line concourse of ACT gun concavity of field lines shows where the field is most off-axis [1]. Ability to reprint figure under the license number <b>5192550991050</b> 25

Figure 2.1.3 (a) ACT field profile for the magnitude of the electric field, (b) magnetic field where dashed line represents the exit of the gun
Figure 2.1.4 Beamline diagram for the ACT showing all three of the solenoids and the location of the cathode with respect to the rest of the beam line and the three imaging stations. Not shown is the RF system before the gun [2]. It is not necessary to obtain permission to reuse this article or its components as it is available under the terms of the Creative Commons Attribution 4.0 International license
Figure 2.1.5 Capture ratio for UNCD for $E_h$ = 43 MV/m (black line) compared with simulation values for capture ratio of $\mid E_h \mid$ (red line) and $E_{h \; max}$ [2]. It is not necessary to obtain permission to reuse this article or its components as it is available under the terms of the Creative Commons Attribution 4.0 International license.
Figure 2.1.6 (a) maximum capture ratio as a function of conditioning field $E_c$ and the corresponding optical magnetic field of the focusing solenoid on the ACT beamline (b) [2]. It is not necessary to obtain permission to reuse this article or its components as it is available under the terms of the Creative Commons Attribution 4.0 International license
Figure 3.0.1 Workflow diagram of FEmaster. 35
Figure 3.1.1 (a) isotropic distribution in momentum space. The single point above the sphere is the test particle where all of the momentum is in the z direction; (b) the distribution for the magnitude of the momentum vector [2]
Figure 3.1.2 (a) Radial distribution calculated using (b) and (c) compare between x and y distributions obtained FEgen [2]
Figure 3.1.3: FEgen interface for initial particle distribution generation. Functionalities include 1) rf and dc pulsed power environments, ability to design 2) uniformly spaced grid of emitters and 3) custom grid of emitters. Note Pulsed power function uses the pulse length of a dc system and the current to calculate the charge. As in any dc environment, the output current is constant with respect to time and does not follow the Gaussian-like distribution associated with the Fowler-Nordheim equation containing time varying electric field. FEgen interface functionality for (a) rf and (b) dc pulsed power environments [2]
Figure 3.1.4 Temporal distribution [2]
Figure 3.2.1 FEbeam's workflow map showing how the data processing algorithm (in blue) takes the raw data from input files (in green) to the output data (in red) and the output figures (in yellow) [1]. AIP Publishing grants a license for all orders
Figure 3.2.2 The initial window to select data to be processed; (b) Display screen that allows for the timestamp of the dataset to be associated with the conditioning gradient that will be later used to rename and group the files. AIP Publishing grants a license for all orders
Figure 3.2.3 The main interface of FEbeam. The top portion sets the rf parameters to translate the raw data into Q-E curves. AIP Publishing grants a license for all orders

Figure 3.2.4 (a) Faraday Cup Settings display interface for selecting the time constant for the low charge case. (b) Plot where red square and circle denote the location of the minimum and maximum threshold values corresponding to 90% and 10% of the maximum value [1]. AIP Publishing grants a license for all orders
Figure 3.2.5 (a) Parameter File Settings for entering the rf parameters to calculate the Q-E curves; (b) waveforms for a low charge scenario; (c) waveforms for a high charge scenario. Red marks denote the region that was considered in the Faraday cup to calculate the charge. AIP Publishing grants a license for all orders. 48
Figure 3.2.6 Emission profile within one rf cycle based on Eq. 3.1.1 (blue solid line) and its Gaussian distribution approximation (red dashed line). Inset: The standard deviation of the Gaussian distribution as a function the maximum microscopic cathode field [1]. AIP Publishing grants a license for all orders.
Figure 3.2.7 Blue: the normalized cathode field amplitude  Ec(t)  measured by the rf pickup. Red: the predicted average emission current IF (t) by Eq. 9. Black: the square pulse approximation of the emission profile. Inset: The width of the square emission profile as a function of βEc,max. Reproduced from Ref.3. AIP Publishing grants a license for all orders
Figure 3.2.8 The emission pulse length ( $\tau$ ) as a function of the local field plotted in the entire fitting range from 0 to 50 GV/m, inset is a zoom-in view of the pulse length within the physically meaningful local field range, from 0 to 10 GV/m. (b) In red is the rf envelope after frequency filter was applied, in blue is the actual pulse measured using pickup in the gun. AIP Publishing grants a license for all orders.
Figure 3.2.9 (a) Display interface for the Fowler-Nordheim fitting; (b) example of an R2 plot; (c) example of a Fowler-Nordheim plot showing the fitting of the two different regions emphasizing the knee point. AIP Publishing grants a license for all orders.
Figure 3.3.1 FEpic inside of FEmaster options for selecting minimum and maximum threshold for image visualization. Options include all three YAG on the ACT and YAG3 having two options one with and without the aperture
Figure 3.3.2 Illustration of closely packed emitters extracted from data for A-class UNCD FECs form the experiment outlined in CH4.
Figure 3.3.3 (a) example of image processing results. (b) decision plot green line shows actual emitters, black line shows the noise, and red line shows the undefined region that is a mixture of noise emitters and actual emitters. (c) machine learning algorithms final decision for decision boundary Gaussian fitting function
Figure 3.4.1 (a) CAD model of waveguide components and diagnostics, (b) a photograph of the current state of the part of the CERF-NM facility in lead box enclosure. All JACOW conference proceedings are published under the Creative Commons Attribution 3.0 license (CC-BY 3.0) to copy and redistribute the material in any medium or format

Figure 3.4.2 Block diagram of FEbreak. All JACOW conference proceedings are published under the Creative Commons Attribution 3.0 license (CC-BY 3.0) to copy and redistribute the material in any medium or format
Figure 3.4.3 User interface for FEbreak. All JACOW conference proceedings are published under the Creative Commons Attribution 3.0 license (CC-BY 3.0) to copy and redistribute the material in any medium or format.
Figure 3.4.4 Nominal (a) and breakdown condition (b) pulses showing the forward, reflected, and Faraday cup signals. All JACOW conference proceedings are published under the Creative Commons Attribution 3.0 license (CC-BY 3.0) to copy and redistribute the material in any medium or format.
Figure 3.4.5 Block diagram of the fully integrated FEmaster. All JACOW conference proceedings are published under the Creative Commons Attribution 3.0 license (CC-BY 3.0) to copy and redistribute the material in any medium or format
Figure 4.1.1 Raman spectrum and SEM micrograph of as-grown sample [33]. It is not necessary to obtain permission to reuse this article or its components as it is available under the terms of the Creative Commons Attribution 4.0 International license.
Figure 4.1.2 Comparison of transverse electron patterns (a) as simulated in GPT and (b) as obtained experimentally, both at YAG3 position. The input emitter distribution was generated and imported using a pattern captured in dc, see Figure 1 in Ref. [6]. Image (b) was processed with FEpic, and counted emitters are labeled by red marks. All other images with local maxima identified and labeled as emitters can be found in Appendix A [33]. It is not necessary to obtain permission to reuse this article or its components as it is available under the terms of the Creative Commons Attribution 4.0 International license
Figure 4.1.3 The Q-E curves for phase one and phase two separated into two regions corresponding to the experiment runs. In the legend, the numerical values label the maximal conditioning gradient achieved per Q-E curve (referred to as $E_h$ ). The inset shows <i>in situ</i> taken image of the major breakdown event, located on the outer edge of the cathode puck at 1 o'clock (labeled with an arrow) that stopped the phase one session [33]. It is not necessary to obtain permission to reuse this article or its components as it is available under the terms of the Creative Commons Attribution 4.0 International license
Figure 4.1.4 Comparison between emission patterns on YAG3 at 70 MV/m taken in Phase 1 (left) and Phase 2 (right, rotated CCW by 50 degrees). The images are placed with respect to the origin: since there is slight <i>y</i> -offset in the left image the right rotated image rests below against the right image [33]. It is not necessary to obtain permission to reuse this article or its components as it is available under the terms of the Creative Commons Attribution 4.0 International license.
Figure 4.1.5 (a) FN plot and (b) R <sup>2</sup> plot exampled for 45 MV/m. For all FN plot Appendix B. [33] It is not necessary to obtain permission to reuse this article or its components as it is available under the terms of the Creative Commons Attribution 4.0 International license.

Figure 4.1.6 Field emission conditioning parameters: (a) field enhancement factor, (b) local field on the cathode surface, and (c) effective emission area for both the FN-like (low field) and non-FN (high field) regions [33]. It is not necessary to obtain permission to reuse this article or its components as it is available under the terms of the Creative Commons Attribution 4.0 International license.
Figure 4.2.1 Maximum charge and the number of emitters determined at the maximum of every conditioning Q-E curve as functions of E <sub>h</sub> . The purple horizontal area represents one standard deviation around the mean value of the emitter number count [33]. It is not necessary to obtain permission to reuse this article or its components as it is available under the terms of the Creative Commons Attribution 4.0 International license
Figure 4.2.2 Millikan plot for 100 MV/m (red) showing the parallel shift denoted with an arrow and is indicative of a space charge dominated regime that differs from the Child Langmuir law (blue). Additional Millikan plots can be seen in Appendix B. It is not necessary to obtain permission to reuse this article or its components as it is available under the terms of the Creative Commons Attribution 4.0 International license
Figure 4.2.3 Brightness dynamics inside the gun for (a) Phase 1 and (c) Phase 2 (0.45 ns timestamp corresponds to the physical end of the gun cavity) and along the entire beamline from the cathode to YAG3 for (b) Phase 1 and (d) Phase 2. For reference, the gun exit corresponds to the time stamp of 0.6 ns for all the figures [33]. It is not necessary to obtain permission to reuse this article or its components as it is available under the terms of the Creative Commons Attribution 4.0 International license
Figure 4.3.1 SEM image of a single emitter pyramid showing the sharpness of the emitter tip for cathode A and cathode B
Figure 4.3.2 QE curves for cathode A and cathode B respectfully
Figure 4.3.3 FN plots for cathode A and cathode B both conditioned to 40 MV/m showing ideal linearity.
Figure 4.3.4 Image taken on YAG3 at 40 MV/m for cathode A and cathode B. Cathode A showing no pattern beam and a large electron cloud due to space charge domination. Cathode B showed a pattern of emission and local maximum determined using FEpic blue crosses in center picture (not to scale); (c) Overlay of the initial DFEA pattern times a magnification factor of 12 (red dots) and the local maximums determined from FEpic (blue). Marker size is to scale at $E_h$ =30 MV/m.
Figure 4.3.5 Faraday cup capture ratio at Eh=40 MV/m as a function of emitting tip size 100
Figure 4.3.6 Raman spectrum comparison between cathode A and cathode B, locations of tips (a) measured for Raman spectrum seen in (c) for cathode A. Likewise locations of tips (b) measured for Raman spectrum seen in (d) for cathode B
Figure 4.3.7 Simplified loadline representation of the ballast resistance effect.

Figure 4.3.8 Concept map showing the different regions of field emission dynamics under high charge high gradient conditions
Figure A 1 Processed images indicating the number of local maxima found for each image from Eh 15 to 55 MV/m from FEpic
Figure A 2 Processed images indicating the number of local maxima found for each image from Eh 60 to 95 MV/m from FEpic
Figure B 1 <i>E<sub>h</sub></i> -15 MV/m Fowler Nordheim plots, knee point decision plots, and Millikan plots
Figure B 2 <i>E</i> <sub>h</sub> -20 MV/m Fowler Nordheim plots, knee point decision plots, and Millikan plots.
Figure B 3 Eh-25 MV/m Fowler Nordheim plots, knee point decision plots, and Millikan plots.
Figure B 4 <i>E</i> <sub>h</sub> -30 MV/m Fowler Nordheim plots, knee point decision plots, and Millikan plots.
Figure B 5 <i>E<sub>h</sub></i> -35 MV/m Fowler Nordheim plots, knee point decision plots, and Millikan plots.
Figure B 6 <i>E<sub>h</sub></i> -40 MV/m Fowler Nordheim plots, knee point decision plots, and Millikan plots.
Figure B 7 <i>E<sub>h</sub></i> -45 MV/m Fowler Nordheim plots, knee point decision plots, and Millikan plots.
Figure B 8 <i>E<sub>h</sub></i> -50 MV/m Fowler Nordheim plots, knee point decision plots, and Millikan plots.
Figure B 9 <i>E<sub>h</sub></i> -55 MV/m Fowler Nordheim plots, knee point decision plots, and Millikan plots.
Figure B 10 <i>E<sub>h</sub></i> -60 MV/m Fowler Nordheim plots, knee point decision plots, and Millikan plots
Figure B 11 <i>E<sub>h</sub></i> -65 MV/m Fowler Nordheim plots, knee point decision plots, and Millikan plots
Figure B 12 <i>E<sub>h</sub></i> -70 MV/m Fowler Nordheim plots, knee point decision plots, and Millikan plots.
Figure B 13 $E_h$ -70 MV/m Fowler Nordheim plots, knee point decision plots, and Millikan plots.

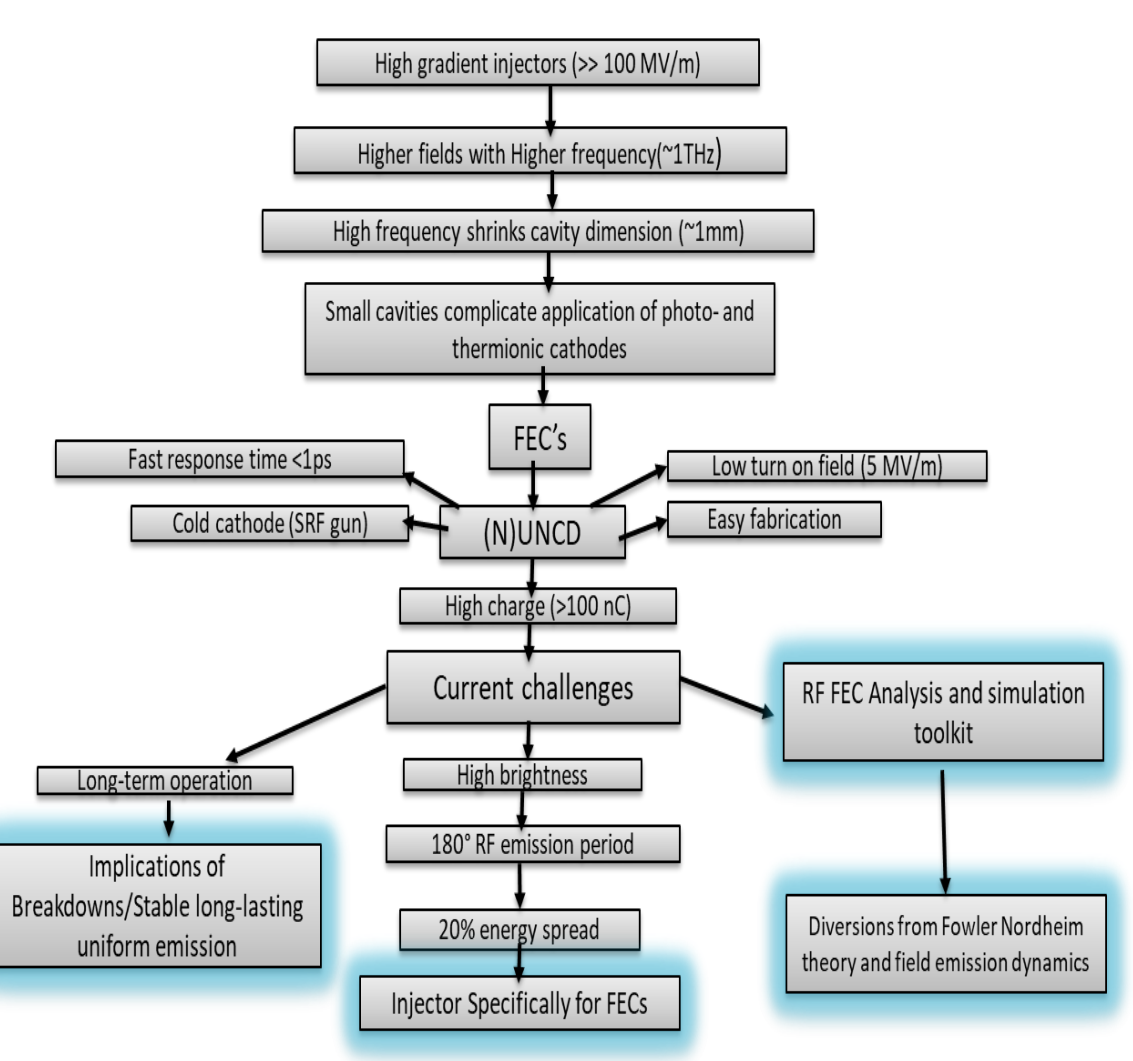
Figure B 14 <i>E</i> <sub>h</sub> -75 MV/m Fowler Nordheim plots, knee point decision plots, and Millikan plots.
Figure B 15 <i>E<sub>h</sub></i> -80 MV/m Fowler Nordheim plots, knee point decision plots, and Millikan plots.
Figure B 16 <i>E<sub>h</sub></i> -85 MV/m Fowler Nordheim plots, knee point decision plots, and Millikan plots.
Figure B 17 <i>E</i> <sub>h</sub> -90 MV/m Fowler Nordheim plots, knee point decision plots, and Millikan plots.
Figure B 18 <i>E<sub>h</sub></i> -95 MV/m Fowler Nordheim plots, knee point decision plots, and Millikan plots

#### **CHAPTER 1 INTRODUCTION**

The accelerator community, motivated by the roadmap laid out in the last Snowmass publication [1], hopes to push the operating gradient of injectors and accelerating structures to in excess of 300 MV/m. These higher gradient fields are achievable due to recent developments in millimeter and THz driven accelerating structures and development of the unique sources needed for the next generation of injectors is underway. The previous generation of injectors, dominated by photoemission and thermionic cathodes, are not practical under these operating conditions which makes a viable field emission cathode (FEC) that can operate in the RF environment necessary. The gap in knowledge (both theoretical and applied) of field emission characteristics in high gradient conditions is substantial and there is a significant opportunity for research in this subject to support widescale adoption in large facility applications.

The areas of investigation in this thesis are presented in Figure 1.1. Path of FEC injector development, with the thesis areas shown in blue. The path outlines the challenges that must be overcome to achieve high frequency, high gradient injectors. These challenges include determining the long-term stability of the source and the implication of the breakdowns on a field emission cathode, detailed in CH2. To analyze the sources, the FEmaster software was developed, representing the most comprehensive data acquisition, data processing, image processing, and modeling toolkit available for field emission sources, detailed in CH3. This led to categorizing field emission sources and determining the dynamics of the sources in extreme environments that pushes the envelope of currently accepted theories, demonstrated in CH4. This

ultimately will lead to determining the design parameters for building a custom field emission injector, detailed in **CH5**.



Path of FEC Injector Development with Thesis Areas in blue

Figure. 1.0.1 The goals of the community to build field emission injectors and the current challenges faced and resolved by this thesis (in blue).

### 1.1 Next Generation Injector Technology

There is currently an international effort to achieve extremely high gradients (>300 MV/m), not only in the accelerating structures but also in the injector design itself. The goal is to mitigate the effects of the space charge emittance to produce extremely bright beams ~10<sup>16</sup> A/(m×rad)<sup>2</sup> [1]. These beams are suitable for applications such as emittance exchange beam lines for flat beam production and light sources including x-ray free electron lasers. To achieve these higher gradients, the community has continuously increased the operational frequency of the injector [1].

The need for high gradient electron machines is crucial not only for pure physics applications such as high energy physics (HEP) but also for the development of compact accelerators. These compact accelerators have the potential to be the next generation of medical, industrial, or even military-based applications and would be needed in large volumes, thousands or greater. The current work on HEP based applications includes but is not limited to 1) CLIC, a compact high gradient accelerator currently being investigated at CERN [2]; 2) improvements in LCLS-II for bright beam applications [3]; 3) emittance exchange beam lines currently developed for advanced acceleration techniques [4]. Finally, the high current densities of field emission sources (on the order of 10<sup>6</sup>-10<sup>8</sup> A/cm<sup>2</sup>) are extremely useful for high current density sources such as DARHT at Los Alamos National laboratory and many other deployable electromagnetic weapon platforms [5].

Increasing knowledge of field emission characteristics of ultrahigh gradient machines also allows for the informed exploration of breakdown effects. In the breakdown community, the so-called dark current is exactly the field emission current, just termed differently. The research presented here is directly applicable to communities outside of electron accelerators and useful

for determining the breakdown characteristics for other machines such as proton or ion linear accelerators (linacs). For example, current work, presented in <u>CH5</u>, shows the development of ultrahigh gradient C-band (5.712 GHz) structures for a proton linac which will be used for major upgrades on the LANCE beamline at Los Alamos National Lab [6-8].

# 1.1.1 Introduction to field emission theory

As Figure 1.1.1 shows, field emission is a purely quantum mechanical process. For field emission in the presence of an external surface electric field (on the order of 1-10 GV/m), the step-like potential barrier slopes so that the electrons can now tunnel through the triangle-like potential barrier. Field emission sources do not need either a heating source or a laser scheme, making them an extremely simplistic electron source beneficial for compact accelerators.

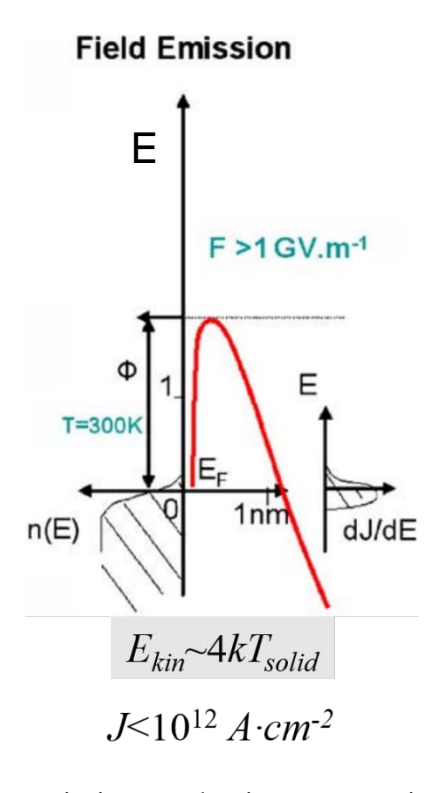


Figure. 1.1.1 diagram for the emission mechanisms comparing thermionic emission, photoemission, and field emission.

The Fowler-Nordheim equation written in the DC case is given by Eq. 1.1.1. By taking the logarithm base 10 of the current divided by  $E^2$ , one can find that there is a linear relationship between  $log_{10}(I/E^2)$  v. 1/E, called the Fowler Nordheim plot [9].

$$I = 1.54 * 10^{-6} \left(\frac{A_e}{\phi}\right) (\beta * E_h)^2 Exp\left(\frac{-6.83*10^9 \phi^{\frac{3}{2}}}{\beta * E_h}\right)$$
 Equation 1.1.1

where I is the FN current,  $A_e$  is effective emission area,  $\phi$  is the work function  $E_h$  is the gradient and  $\beta$  field enhancement factor.

Plotting the data in this coordinate system gives a linear regression where the slope is inversely proportional to the field enhancement factor. The field enhancement factor is a unitless factor that is multiplied by the applied field to determine the actual/local electric field on the cathode surface. The Fowler-Nordheim equation allows the formal determination of the effective emission area, which is the area of the cathode that is actually emitting electrons. However, many recent DC experiments [10-12] have experimental data that diverges from assumptions made in the Fowler Nordheim equations. Some of the crucial assumptions of the Fowler Nordheim theory are as follows: 1) the field emission source is at absolute zero, 2) the surface is a perfect conductor, 3) the work function of the material is perfectly uniform, and 4) the field emitter is perfectly planar. In addition to the assumptions made for the DC Fowler Nordheim equations, the RF Fowler-Nordheim equation (below) does not consider beam effects such as space charge and beam loading.

Furthermore, the original Fowler-Nordheim equation was for a DC case. Experimentally, field emission sources have been extensively studied in the DC environment. At the same time, much less attention was paid to FECs operating in the RF/microwave domain. The time-dependent nature of RF injectors makes the dynamics of a field emission source completely different and

brings up unique fundamental and applied challenges and opportunities when designing an optimal injector for field emission sources.

The time-dependent Fowler-Nordheim equation reads [12]:

$$\overline{I_F(t)} = -\frac{5.7 \times 10^{-12} \times 10^{4.52 * \varphi^{-0.5}} A_e [\beta E_c(t)]^{2.5}}{\varphi^{1.75}} \times Exp \left[ \frac{-6.53 \times 10^9 \ \varphi^{1.5}}{A_e [\beta E_c(t)]} \right] \text{ Eq } 1.1.2a$$

Then the expressions for the field enhancement factor is seen in Eq 1.1.2b.

$$\beta = \frac{-2.84*10^9 \varphi^{1.5}}{s} , A_e = \frac{10^{y_0} \varphi^{1.75}}{5.7*10^{-12}*10^{4.52} \varphi^{-0.5} \beta} \text{ Eq. 1.1.2b}$$

where s slope and  $y_0$  is the y-intercept obtained from the linear regression of the fitting of the Fowler Nordheim plot.

A representation of a Fowler Nordheim plot that shows no deviation from the Fowler Nordheim theory is seen in **Figure 1.1.2.** In the RF case, the Fowler-Nordheim coordinates are now modified to  $log_{10}(I/E^{2.5})$  v. 1/E.

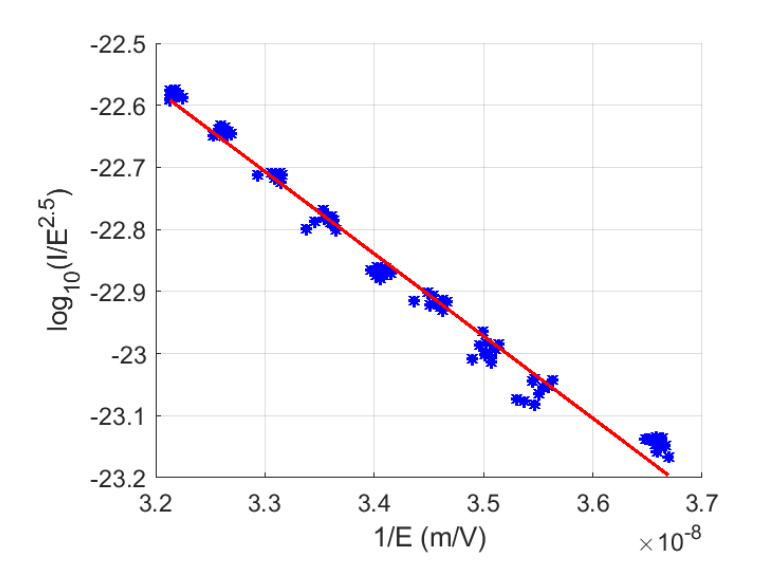


Figure. 1.1.2 example of a classical Fowler Nordheim plot with no deviation using the RF coordinates.

The intrinsic time dependency in RF implies that the electrons can be emitted whenever the RF field is positive as shown in **Figure 1.1.3**. Therefore, unlike with photoemission sources, field emission sources cannot naturally be phase locked to a certain portion of the RF signal field. The intrinsic energy spread of field emission source is exacerbated in the RF environment resulting in energy spreads normally on the order of 20%. This large energy spread results in the need to develop custom-built field emission injectors that can manage a large energy spread as explained in **CH5**. The actual emission mechanisms that the field emission sources are subjected to in an RF environment are not well documented. This led to the development of the FEmaster software series, in particular FEbeam which analyses the field emission source. This series is explained in **CH3**. FEmaster gives the ability to analyze and determine the performance characteristics of time dependent Fowler Nordheim under high gradient conditions which is examined in extensive detail in **CH4**.

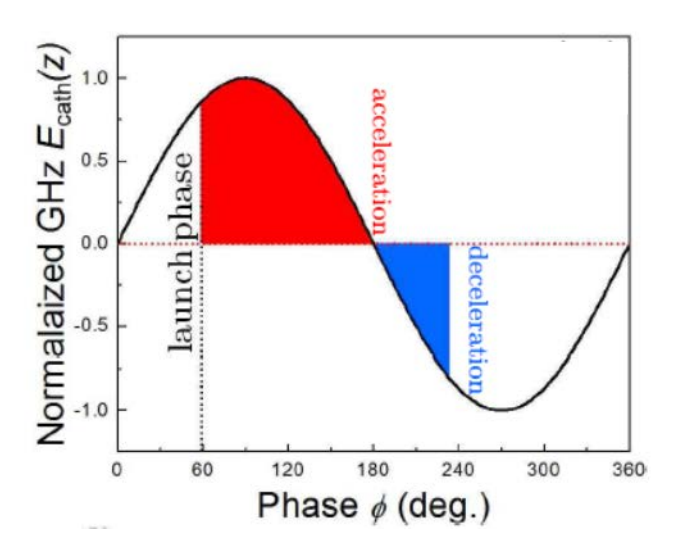


Figure. 1.1.3 FEC RF phase window from J. Qui and S. Baryshev, IEEE Transactions on Electron Devises 65, 1132 (2018) [15]. The IEEE does not require individuals working on a thesis to obtain a formal reuse license.

### 1.1.2 High-frequency injectors implications of source development

The reason that increasing the operational frequency increases the maximum applied gradient is due to the sinusoidal oscillating RF field. The higher frequency means that the structure only has to be subjected to that maximum power for a smaller amount of time. The average power being lower means that breakdowns are less probable. This decrease in breakdown probability/rate means that the structure can be conditioned up to a higher field. Conditioning is the process of incrementally increasing the power delivered to the cavity to control the breakdown rate of the cathode and achieve a desired applied gradient.

Increasing the operational frequency does come with one caveat: it shrinks the fabrication dimensions of the cavity as the residence frequency  $\omega$ =k\*c, where k is the wave number, c is the speed of light, and the wave number is inversely proportional to the dimensions of the cavity. For example, if one considers a simple pillbox (cylindrical) cavity. The residence frequency can be defined as **Eq 1.1.2** 

$$\omega_{\rm mnp} = c \sqrt{\left(\frac{X_{\rm nm}}{a}\right)^2 + \left(\frac{\pi p}{L}\right)^2}$$
 Equation 1.1.3

where m, n and p are integer modes,  $X_{nm}$  is the zeros of the Bessel function, and a is the radius, and L is the length of the structure.

Assuming that the structure operates at the most fundamental accelerating mode corresponding to the  $TM_{010}$  mode m=p=0, Eq. 1.1.3 is simplified to Eq. 1.1.4 which shows that the residence frequency is inversely proportional to the radius.

$$\omega_{\rm mnp} = c \frac{x_{\rm nm}}{a}$$
 Equation 1.1.4

For example, SLAC builds THz injectors (Figure 1.1.4) [16-20] that has a cavity radius on the order of ~0.1mm, meaning that the cathode to power the new injector has to be on the order of the radius of the cavity or smaller. These pinheads size cathodes impose new challenges

when trying to operate these cathodes under the previous conventional electron generating mechanisms such as thermionic emission or photoemission.

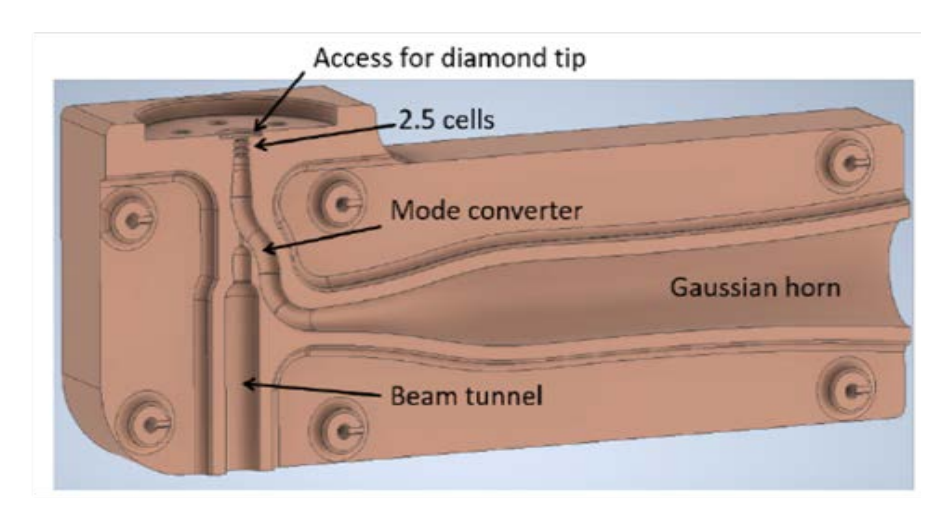


Figure. 1.1.4: SLAC's 110 GHz field emission injector with a 1mm beam aperture taken from S. Lewis proceedings IPAC 2019 [20]. All JACOW conference proceedings are published under the Creative Commons Attribution 3.0 license (CC-BY 3.0) to copy and redistribute the material in any medium or format.

It is unlikely high-frequency high injector cavities can be operated using thermionic cathodes. Under these dimensional constraints, the heating source of a thermionic cathode, which normally has to heat the cathode to around 1000°C, would dissipate its heat not only into the cathode, driving electron emission, but also into the surrounding cavity. This temperature is needed due to the thermal work function of the material which is on the order of a few eV temperatures greater than the 1000°C needed for emission. This temperature would likely make the cavity completely nonfunctional. For normal conducting cavities which are constructed out of copper, this increase of heat would cause the copper cavity to undergo thermal expansion. This would detune the cavity out of resonance, decreasing the beam quality. In an excessive case, the heat could be such that it could permanently warp the dimensions of the cavity to the point that the cavity and the injector would be nonoperational.

On the other hand, photo emission cathodes need high-power millijoule class 4 lasers to stimulate emission on the cathode surface. A complex mirror-aperture delivery system would be required. Also, typical beam size is 100 microns and therefore could cause undesirable parasitic electron background due to laser scraping the copper walls. Photoemission cathodes can be used for high gradient high-frequency structures, but it is much harder to operate than it would be for lower frequency structures such as L or S band [21].

The challenges with the temporal dynamics and large energy spread of field emission source means producing bright beams for facility applications is not feasible under the current state-of-the-art injector technology.

# 1.1.3 FEC bright beams and dark current effects

When comparing accelerators to accelerators, figures of merit commonly used are drawn in terms of output current I, current density j, or beam brightness B - which is the most challenging and ambitious metric to achieve. Brightness is defined as  $B = \frac{2I}{\varepsilon_{\perp}^2}$ , where the total normalized transverse emittance  $\varepsilon_{\perp}$  is found as:

$$\varepsilon_{\perp}^2 = \varepsilon_{int}^2 + \varepsilon_{sc}^2 + \varepsilon_{rf}^2$$
 Equation 1.1.5

with  $\varepsilon_{int}$  being the intrinsic cathode emittance, and  $\varepsilon_{sc}$  and  $\varepsilon_{rf}$  being the space charge induced and rf induced emittance, respectively.

The definitions of the brightness and emittance set the stage for rf injector developments. It thus involves material science, emission physics and high power rf design. Additional sources of emittance growth exist due to electron optics not being ideal, e.g., astigmatic solenoid, but those can be fairly easily corrected by using a standard quadrupole based stigmators [22,23].

For planar cathodes [24], the space charge term is reduced through the increase of the macroscopic cathode rf field E (also termed gradient) as

$$\varepsilon_{SC} = \frac{1}{8} \frac{I}{I_A} \frac{\lambda}{\alpha} \frac{1}{3 \frac{\sigma_{\perp}}{\sigma_{\alpha}} + 5},$$
 Equation 1.1.2

where  $I_A$  is the Alfven current of 17 kA,  $\lambda$  is the operating rf wavelength,  $\sigma_{\perp}$  and  $\sigma_z$  are transverse and longitudinal bunch sizes, respectively, and  $\alpha = \frac{eE}{4\pi m_e c^2} \lambda$  with  $m_e$  being the electron mass and c being the speed of light [25].

Development of high frequency (C- to W- band) injectors is pivotal to greatly enhance the cathode peak electric field well above 100 MV/m to 300-500 MV/m, with 500 MV/m demonstrated in X-band [26,27], as higher operating frequency greatly suppresses the breakdown rate and enhances the system compactness at the same time.

One trade-off is that rf emittance grows with the gradient as:

$$\varepsilon_{rf} = \frac{\sqrt{2}\pi^2}{\lambda^2} \frac{eE}{m_e c^2} \sigma_{\perp}^2 \sigma_z^2$$
 [28]. Equation 1.1.3

In the case of a photocathode, the rf emittance can be minimized by minimizing  $\sigma_z$  through a phase matched femtosecond laser. In X-band frequency and well above [17], the use of photocathodes is extremely challenging due to size constraints, another benefit of using a field emission cathode (FEC) in place of photo emission technology which must be evaluated in great detail. To enable FEC operation, special dc-ac or harmonic mixing gating techniques or multicell designs were applied to reduce  $\sigma_z$  [28,29,30]. Since an injector that features high E and reduced  $\sigma_z$  has become available, it is critical to find a cathode material that 1) features low intrinsic emittance, 2) is capable of emitting 1-100 pC per rf cycle (translating to a current of many Amperes) and yet 3) is capable of surviving when exposed to a gradient on the order of 100 MV/m and above.

To achieve brightnesses like that presented in <u>CH4</u>, the structure must be tested up to extremely high gradients and the required normal breakdown rate during conditioning is on the

order of 10<sup>-3</sup> breakdowns per hour. Breakdown rates higher than this are normally considered to be experiment ending where the breakdowns would permanently damage the structure and degrade the vacuum in the system to the point of non-operation. This is due to, when a breakdown occurs, the local field is normally in excess of the interatomic force of 10 GV/m which is described in more detail in CH4. This causes a thermal runaway and therefore the surface emits a strong burst of electrons and x-rays. At the same time, jets of vaporized or liquid copper may be deposited onto or interact with inner structure surface of the cavity. Thus, categorizing and determining a conditioning procedure that allows for cathodes to be conditioned to extremely high gradients, without damaging the injector itself or causing breakdown rate high enough to end the experiment, is crucial.

#### 1.2 Advancement in polycrystalline diamond fabrication technology

Ultra-Nano-Crystalline Diamond (UNCD), along with other carbon-based sources, have been of great interest in recent years as a field emission source for a variety of applications. The

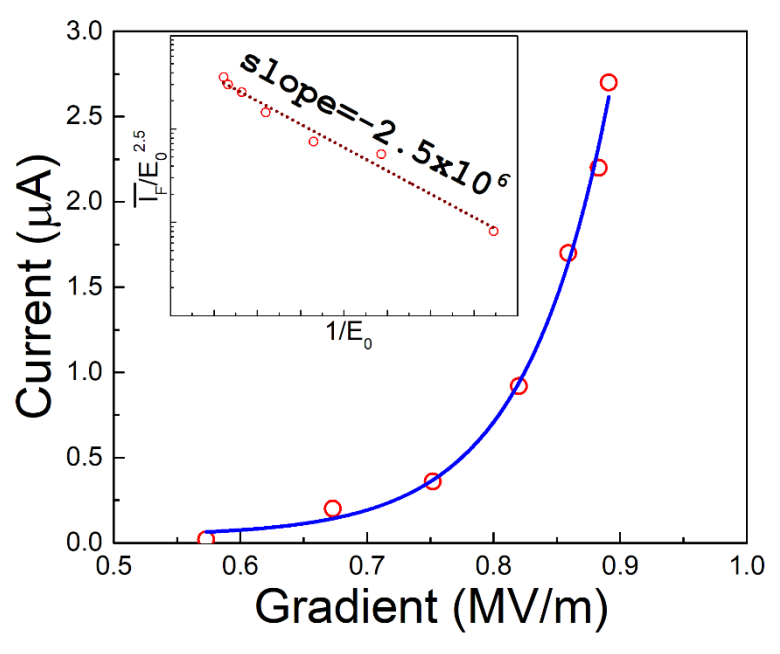


Figure. 1.2.1 UNCD cathode operated in a L-band SRF injector would turn on field at 0.6 MV/m [31]. AIP Publishing grants a license for all orders.

turn on field of this material, i.e., the lowest applied field to where emission can be observed, was found to be as low as 5 MV/m [15] in normal conducting and less than 1 MV/m [31] in superconducting radiofrequency injectors as seen **Figure 1.2.1**.

Another aspect of interest is that diamond has an intrinsically fast response time (~100 fs) which makes it applicable for rf/microwave applications even in W-band (100 GHz). Recent experiments have shown that a (N)UNCD can successfully operate in an X-band (10 GHz) injector (see **Figure 1.2.2**) [32,33].

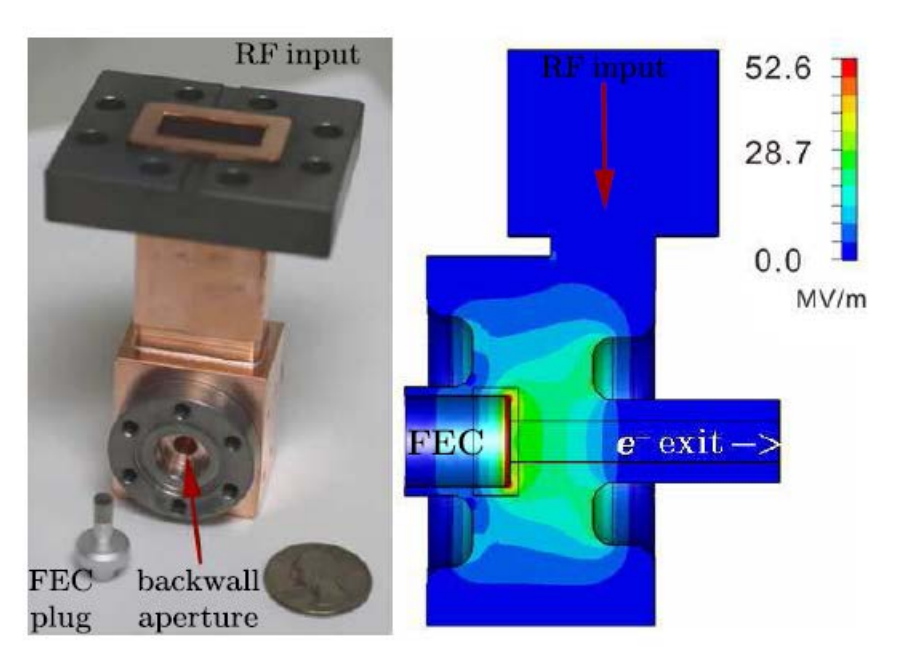


Figure. 1.2.2 copper normal conducting X-band injector with cathode plug and field map using a UNCD field emission cathode [33]. The IEEE does not require individuals working on a thesis to obtain a formal reuse license.

(N)UNCD in particular is a great emitter source for accelerators as it can be used as a simple planar thin film emitter. It has the most sp<sup>2</sup> diamond grain boundaries per unit area when compared to other forms of diamond as the grain sizes are on the order of approximately 10 nm (see **Figure 1.2.3**). Since emission in diamond materials is known to come from the grain boundaries [34,35,36], the diamond with the most grain boundaries per unit area will have the

ability to produce the highest charge. (The implication of this high charge beam capabilities is explained in detail in <u>CH4</u>.)

Microcrystalline: Nanocrystalline: UNCD:
dia. grain ≥500 nm dia. grain 10-200 nm dia. grain ≤10 nm

200 nm

Figure. 1.2.3 SEM images showing the relative grain size between different forms of polycrystalline diamond being that of micro, nano, and UNCD from [34]. Ability to reprint figure under the license number **5192220196519**.

UNCD and other forms of polycrystalline diamond are also useful for transversely shaped beams. Cathodes can be made in any imaginable geometrical form factor by using a silicon substrate to make a mold and then using microwave plasma deposition to fill the molds with diamonds which can then be brazed onto a variety of substrates (see **Figure 1.2.4**). This technique of making diamond field emitter arrays (DFEAs) was pioneered by Vanderbilt

University and is now continuing on in work at Los Alamos [37]. It will be explored in more detail in CH4.

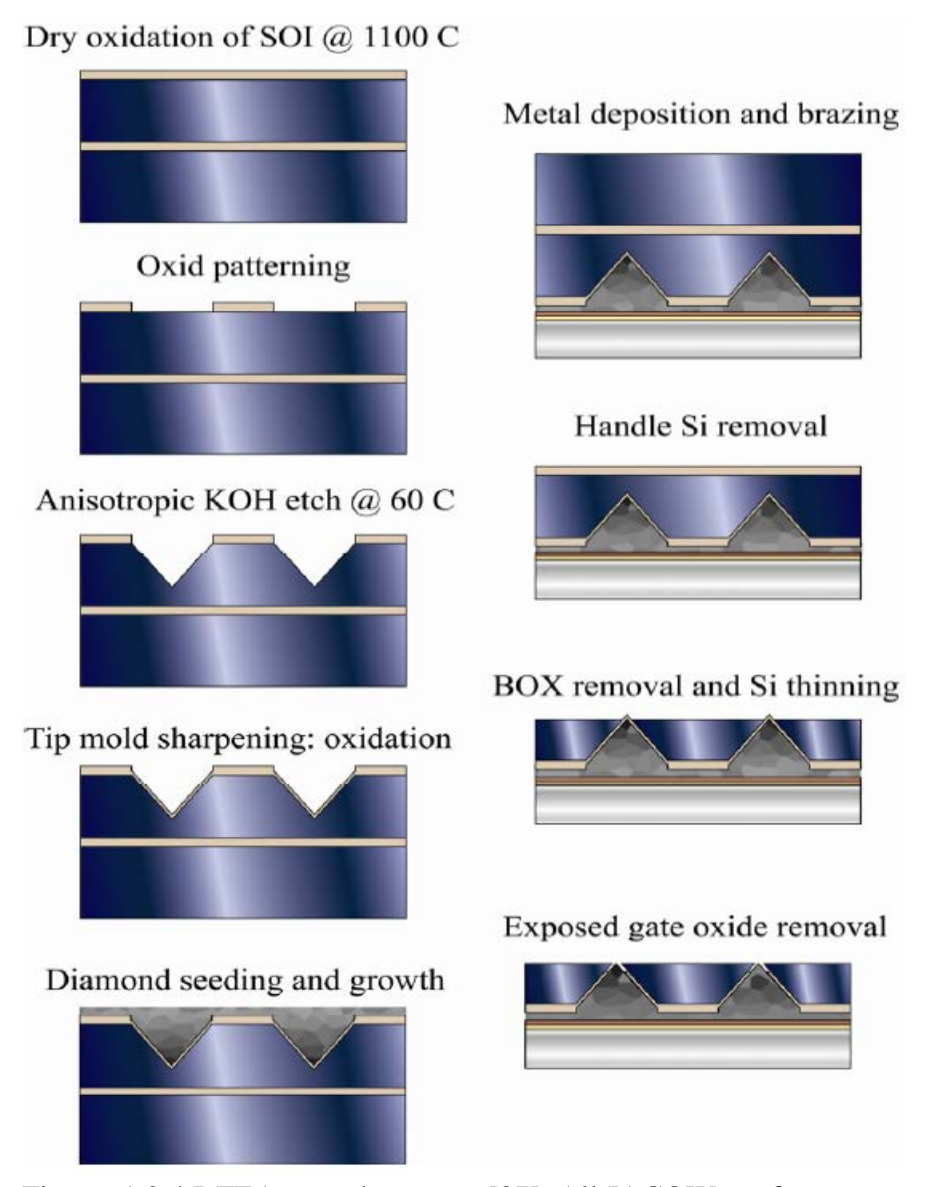


Figure. 1.2.4 DFEA growth process [37]. All JACOW conference proceedings are published under the Creative Commons Attribution 3.0 license (CC-BY 3.0) to copy and redistribute the material in any medium or format.

The actual growth process is common for any kind of diamond. A microwave plasma deposition system which operates in S-band at 2.45 GHz provides a plasma consisting of methane and hydrogen (and doping nitrogen as necessary) as growth precursors (see **Figure** 

**1.2.5**). The plasma dissociates the precursor gas mixture into reactive species. Sp3 to sp2 ratio is directly controlled through the methane to hydrogen ratio and microwave power in the reactor and can be thoroughly analyzed with Raman spectroscopy [38].

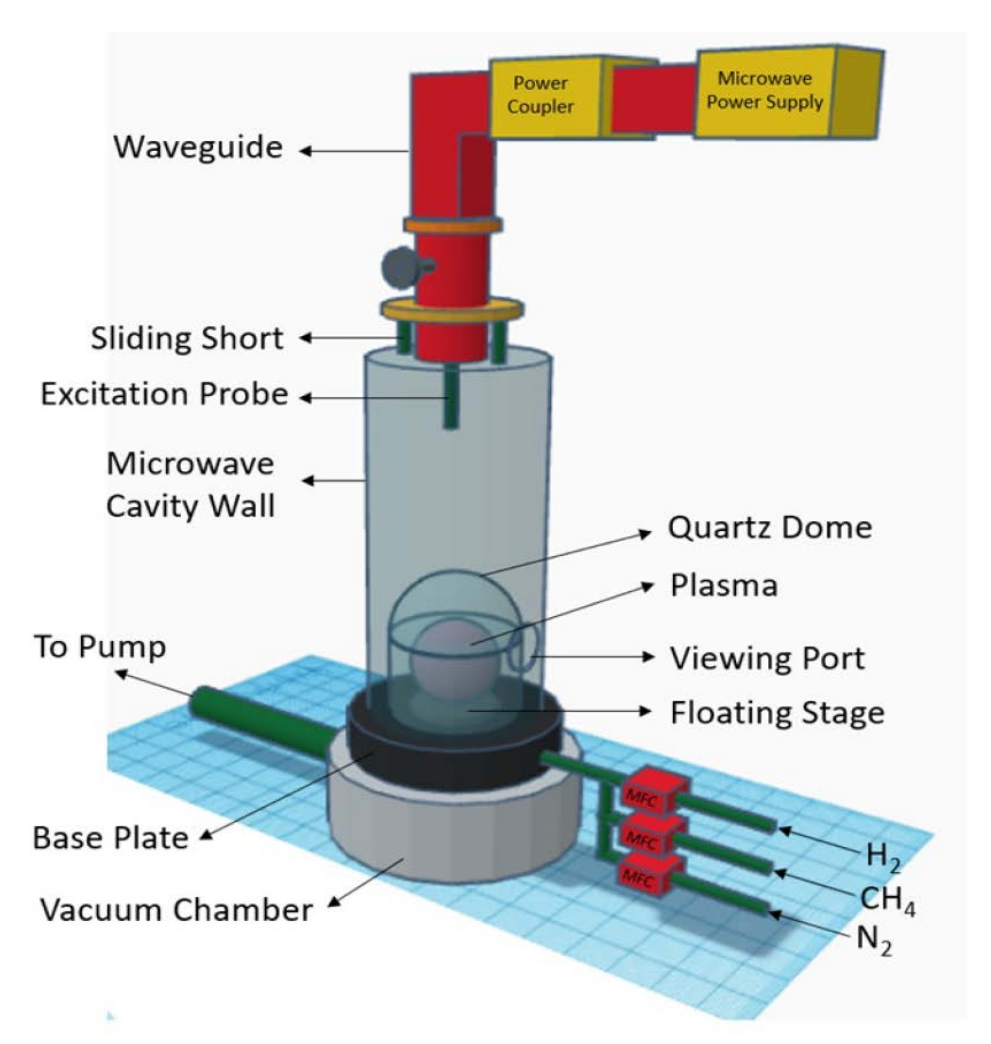


Figure. 1.2.5 Diagram of the UNCD growth chamber used at Michigan State University and the Fraunhofer Institute [38]. This figure has been approved to be reprinted in accordance with approval from the author Tanvi Nikhar MS.

**REFERENCES** 

#### REFERENCES

- [1] J. Shao, J. Power, C. Jing, G. Ha, et al. In 2021 Snowmass Workshop LOI. (2020)
- [2] The International Linear Collider technical design report (2013) Technical report, ILC
- [3] P. Emma, R. Akre, J. Arthur R Bionta *et al.* Nat. Photon. **4** 641 (2010)
- [4] G. Ha, J. Power, M. Conde, D. Doran, *et al.* In Proceedings of 38th International Free Electron Laser Conference (2018)
- [5] C. Ekdahl, J. Coleman, B. McCuistian. IEEE Transactions on Plasma Science, 44(7), 1094 (2016)
- [6] E. I. Simakov, J. E. Acosta, D. V. Gorelov, T. A. Jankowski *et al.* Proceedings from 12<sup>th</sup> International Particle Accelerator Conference (IPAC2021), Campinas, SP, Brazil (2021)
- [7] E. I. Simakov, R. L. Fleming, D. V. Gorelov, M. Kirshner, *et al* Proceedings from 12<sup>th</sup> International Particle Accelerator Conference (IPAC2021), Campinas, SP, Brazil (2021)
- [8] D. V. Gorelov, R. L. Fleming, S. K. Lawrence, J. W. Lewellen *et al* Proceedings from 12<sup>th</sup> International Particle Accelerator Conference (IPAC2021), Campinas, SP, Brazil (2021)
- [9] R. Fowler & L. Nordheim, Proceedings of the Royal Society of London. Series A, Containing Papers of a Mathematical and Physical Character, **119**(781), 173 (1928)
- [10] V. Satopaa, J. Albrecht, D. Irwin, and B. Raghavan, in 2011 31st International Conference on Distributed Computing Systems Workshops (2011)
- [11] R. Forbes, Appl. Phys. Lett. **110**, 133109 (2017)
- [12] T. Posos, S. Fairchild, J. Park, S. V. Baryshev, Journal of Vacuum Science & Technology B, Nanotechnology and Microelectronics: Materials, Processing, Measurement, and Phenomena, **38**(2), 024006 (2020)
- [13] J Shao, Investigations on rf Breakdown Phenomenon in High Gradient Accelerating Structures, Springer Theses (2018)
- [14] J. Shao, M. Schneider, G. Chen T. Nikhar *et al*, Phys. Rev. Accel. Beams **22**, 123402 (2019)
- [15] J. Qui and S. Baryshev IEEE Transactions on Electron Devises 65, 1132 (2018)
- [16] S. M. Lewis, A THz-Driven Electron Gun, thesis University of California at Berkeley (2020)

- [17] M. Othman, J. Picard, S. Schaub, V. A. Dolgashev, *et al.* Appl. Phys. Lett. **117**, 073502 (2020)
- [18] S. M. Lewis, J. Merrick, M. Othman, A. Haase, *et al.* In proceedings from 45th International Conference on Infrared, Millimeter, and Terahertz Waves (2020)
- [19] M. Othman, A. Gabriel, E. Snively, M. Kozina, **et al.** 45th In proceedings International Conference on Infrared, Millimeter, and Terahertz Waves (2020)
- [20] S. Lewis, A. Haase, D. Kim, E. A. Nanni et al. In proceedings International Particle Accelerator Conference (2019)
- [21] F. Sakamoto, M. Uesaka, K. Dobashi, A. Fukasawa, et al. J. Korean Phys. Soc. 49, 286 (2006)
- [22] L. Zheng, J. Shao, Y. Du, J. G. Power, Phys. Rev. Accel. Beams 22, 072805 (2019).
- [23] J. Qiu, G. Ha, C. Jing, S. V. Baryshev, et al Ultramicroscopy **161**, 130 (2016).
- [24] D. H. Dowell, Phys. Rev. Accel. Beams **22**, 084201 (2019).
- [25] K. J. Kim, Nuclear Instruments and Methods in Physics Research Section A: Accelerators, Spectrometers, Detectors and Associated Equipment 275, 201 (1989).
- [26] A. D. Cahill, J. B. Rosenzweig, V. A. Dolgashev, S. G. Tantawi, S. Weathersby, Phys. Rev. Accel. Beams **21**, 102002 (2018).
- [27] V. Dolgashev, S. Tantawi, Y. Higashi, and B. Spataro, Applied Physics Letters **97**, 171501 (2010).
- [28] L. Schachter, W. D. Kimura, and I. Ben-Zvi, AIP Conference Proceedings 1777, 080013 (2016).
- [29] J. W. Lewellen and J. Noonan, Phys. Rev. ST Accel. Beams **8**, 033502 (2005).
- [30] X. Li, M. Li, L. Dan, Y. Liu, C. Tang, Phys. Rev. ST Accel. Beams **16**, 123401 (2013)
- [31] S. V. Baryshev, E. Wang, C. Jing, V. Jabotinski, et al. App. Phys. Lett., 118 (5), 053505.
- [32] Z. Li, S. G. Tantawi, T. Y. Posos, M. S. Schneider, S. V. Baryshev. Proceedings from 12<sup>th</sup> International Particle Accelerator Conference (IPAC2021), Campinas, SP, Brazil (2021)
- [33] J. Qiu, S. S. Baturin, K. K. Kovi, O. Chubenko, et al. IEEE Transactions on Electron Devices, **65** (3), 1132-1138.
- [34] A. V. Sumant, O. Auciello, R. W. Carpick, S. Srinivasan, *et al.* MRS bulletin, **35(4)**, 281 (2010)

- [35] L. Y. Zhou, J. Shi, D. Wang, W. Gai, H. Chen, 8th Int. IPAC'17 (2017)
- [36] F. Sakamoto, M. Uesaka, K. Dobashi, A. Fukasawa, T. Yamamoto, et al., J. Korean Phys. Soc. 49, 286 (2006)
- [37] J. Jarvis, H. Andrews, C. Brau, B. Choi, et al. Proceedings of FEL2009, Liverpool, UK (2009)
- [38] T. Nikhar, Revisiting Effects of Nitrogen Incorporation and Graphitization on Conductivity of Ultra-nano-crystalline Diamond Films, thesis Michigan State University (2019)

#### **CHAPTER 2 TECHNICAL RELEVANCE**

This chapter builds upon a combination of the breakdown knowledge obtained previously using the Argonne Cathode Test-stand, as outlined in Jiahang Shao's PhD thesis [1], and a preliminary study that develops the conditioning procedure to obtain optimal cathode performance, as outlined in a Physical Review Accelerators and Beams paper published in 2019 [2]. Specifically, this work outlines a rigorous conditioning procedure to obtain maximum cathode performance with regard to achieving the maximum output current per pulse as well as the maximum achievable fields, while also mitigating effects such as beam loading, multipacting (both were not observed or were negligible this conditioning procedure) and minimizing the breakdown rate.

# CHAPTER 2 L-BAND CATHODE TESTING FACILITIES AND DEVELOPMENT OF CATHODE CONDITIONING PROCEDURES

In order to develop a compact injector that can provide high brightness and Ampere-class beams, it was necessary to conduct benchmarking experiments at a relevant beamline facility, i.e., at a facility that 1) is injector power and beam energy rated, 2) operates in the relevant frequency range and 3) has all relevant beam diagnostics. The Argonne Cathode Test-stand (ACT), part of the Argonne Wakefield Accelerator (AWA) facility at Argonne National laboratory (ANL) fit these requirements. The ACT was developed and optimized for field and photo emission cathodes R&D. It is an TM<sub>01</sub> L-band (1.3 GHz) system, allowing for the largest cathodes. This, in turn, allows for imaging and beam diagnostics with the least complexity. This allows important physics insights to be obtained with ease and applied toward W band (~100 GHz) expected operation/performance. In other words, L-band experiments can be used as a baseline for developing the next generation of injectors.

## 2.1 The Argonne Cathode Teststand (ACT)

The ACT allows for maximum cathode diameters of 0.777 inch and is a single RF wavelength cell with gap distance of 2 cm, which can yield 2 MeV electrons at the output at 100

MV/m field (klystron power limit for flat cathode). A cross-sectional and 3D CAD model photo of the ACT gun can be seen in **Figure 2.1.1** [1].

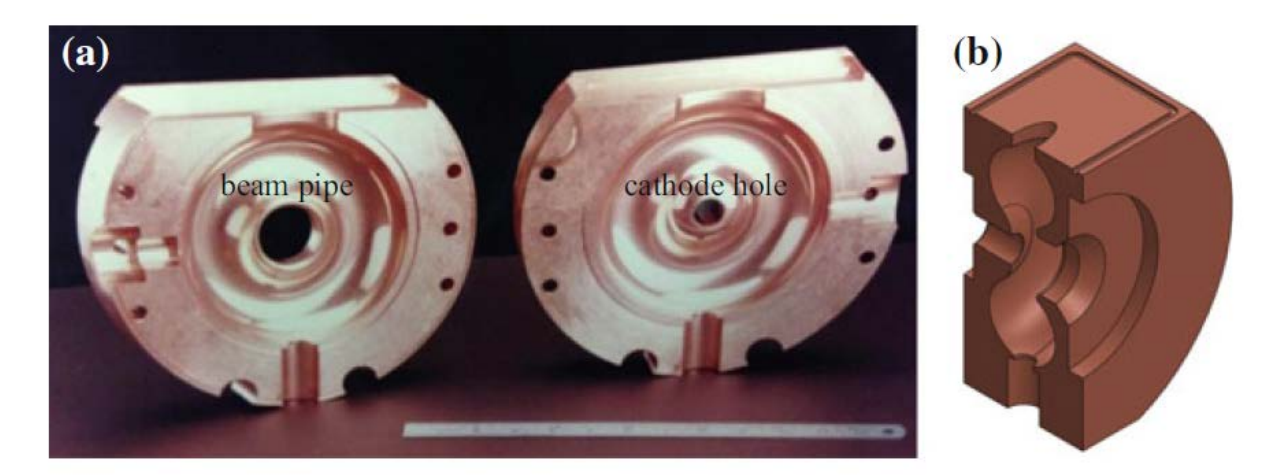


Figure. 2.1.1 (a) transverse cross-sectional photo of ACT gun showing the beam aperture and the cathode holder. Photo was taken before brazing the two sections of the cavity into one part. (b) shows a longitudinal cross-section of the 3D model of the ACT gun [1]. Ability to reprint figure under the license number **5192550991050**.

The ACT can operate using pulse lengths of 2 µs, 4 µs, or 6 µs with a 2 Hz repetition rate. A pulse length refers to how long the klystron power is turned on for and not the length of an RF cycle [1]. For example, the experiments presented here are normally operated at 6 µs which means that there are approximately 8000 RF cycles in a single pulse length. Therefore, a true unit of measure when comparing these results should refer to the charge per RF cycle and not the charge per pulse length. At higher frequency structures, there are more RF cycles in a single pulse length which means that two beams with the same charge per pulse may have orders of magnitude different charge per pulse length. This difference in charge per RF cycle may have drastic implications on the beam dynamics such as beam loading and space charge forces. Likewise, one can simply increase the charge per pulse by increasing the pulse length as the charge will scale linearly with the number of RF cycles.

To have peak efficiency in the extraction of the charge created from the FEC, the fields need to be optimized to allow only on-axis fields on the cathode surface. On-axis fields refers to the fields that are in the longitudinal direction, i.e., z direction. Electrons generated in a place where there are off-axis fields will cause the trajectory of the particles to start to form spiral motions which would increase the transit time in the gun. This off axis field within the gun causes an increase in the transverse emittance due to an increase in the RF emittance. This could get to the point where the field switches polarity which would contribute to a larger energy spread. Even electrons that are generated only slightly off-axis, where transverse component of the field is almost negligible, will still have larger energy spread due to having a longer transit time. This can be seen by observing the field lines in **Figure 2.1.2** of the ACT gun where an on-axis field would appear as a perfectly straight line in the beam propagation [1] although these off axis fields are negligible on the cathode surface and are mostly confined near the exit of the gun.

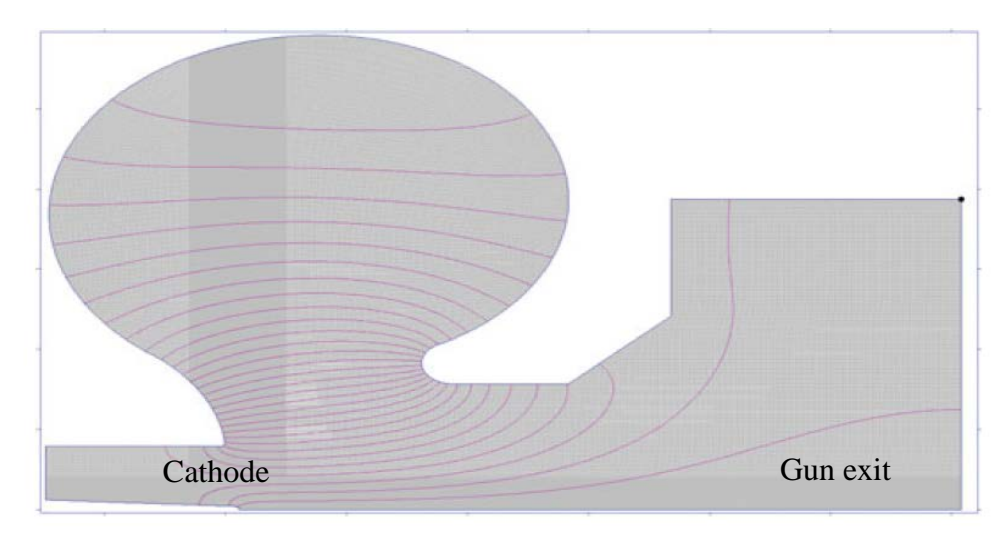


Figure. 2.1.2 E field map line concourse of ACT gun concavity of field lines shows where the field is most off-axis [1]. Ability to reprint figure under the license number **5192550991050**.

**Figure 2.1.3a and b** shows the electric and magnetic fields inside and just after the exit of the gun. There is a strong secondary peak in the electric field at the exit of the gun [1]. The

ACT is said to have an asymmetric gun exit due to the secondary kick at the exit of the gun caused by the standing wave nature of the ACT cavity. This secondary peak in the electric field causes asymmetric focusing which defocuses the electrons out of the gun, causing a second peak in the magnetic field (gun exit is denoted with black dash line). This asymmetric focusing is an artifact of the ACT's original purpose for breakdown studies where additional focusing elements would be counterproductive [1]. This, coupled with the large energy spread due to electrons being emitted over the entire 360° RF cycle, results in additional solenoid focusing needed along the beam line. Figure 2.1.3 shows this asymmetric focusing after the exit of the gun (denoted by red dashed circle).

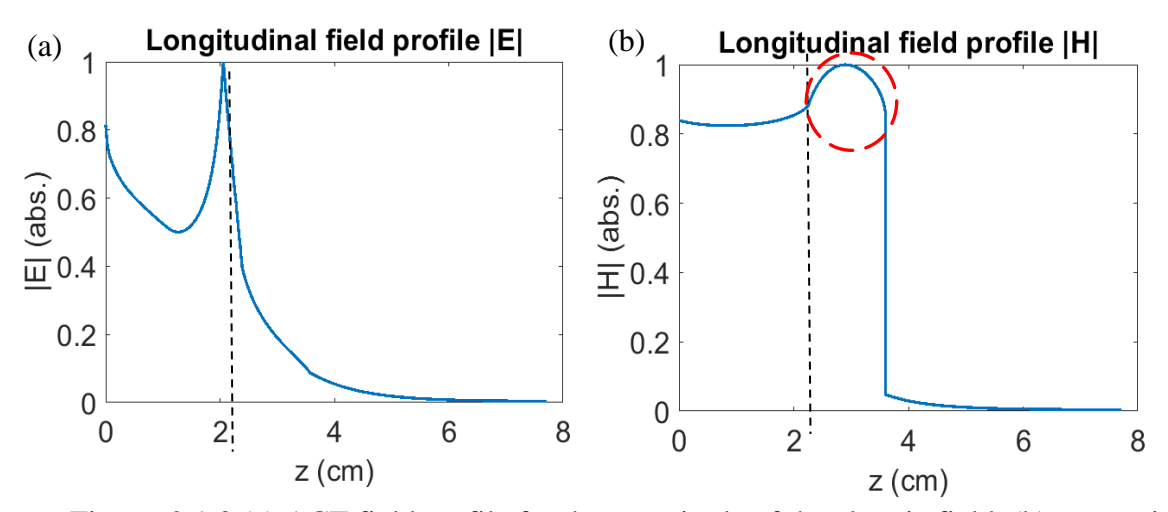


Figure. 2.1.3 (a) ACT field profile for the magnitude of the electric field, (b) magnetic field where dashed line represents the exit of the gun.

Therefore, the ACT has three solenoid magnets that are used for focusing of the beam (see **Figure 2.1.4**.) The first two are a coupled pair of solenoids called the bucking solenoid and focusing solenoid. The bucking solenoid is placed behind the RF gun and the current is run in opposite direction with respect to the focusing solenoid so that, when both are run together, they can cancel out the magnetic fields inside of the gun. This cancels out some of the off-axis fields, decreasing the transit time and resulting in a lower divergence angle. The focusing solenoid has

more windings of wire on it so that it not only cancels out the magnetic fields inside of the gun, but also provides the main focusing outside of the gun. The focusing solenoid normally runs at twice the magnetic field of the imaging solenoid. The imaging solenoid is placed 74 cm downstream with respect to the back wall of the gun which is set as the origin. The imaging solenoid is used to focus the beam down to a waist in the plane of the second Yttrium Aluminum Garnet (YAG) imaging screen.

The ACT has three imaging screens as seen in **Figure 2.1.4.** At the location of YAG 1, there is a Faraday cup that is used to collect the charge. YAG1 and Faraday cup are interchangeable. This diagnostics plane is located 25 cm from the cathode. The YAG2 screen plane is located 1.55 m away from the cathode and can be swapped with a variety of apertures used for beam collimation. The aperture that was used in all experiments for best imaging resolution was a 1 mm circular aperture for the center of the beam. Since the center of the beam is the electrons generated on axis, this 1 mm aperture filters most of the electrons that are off axis

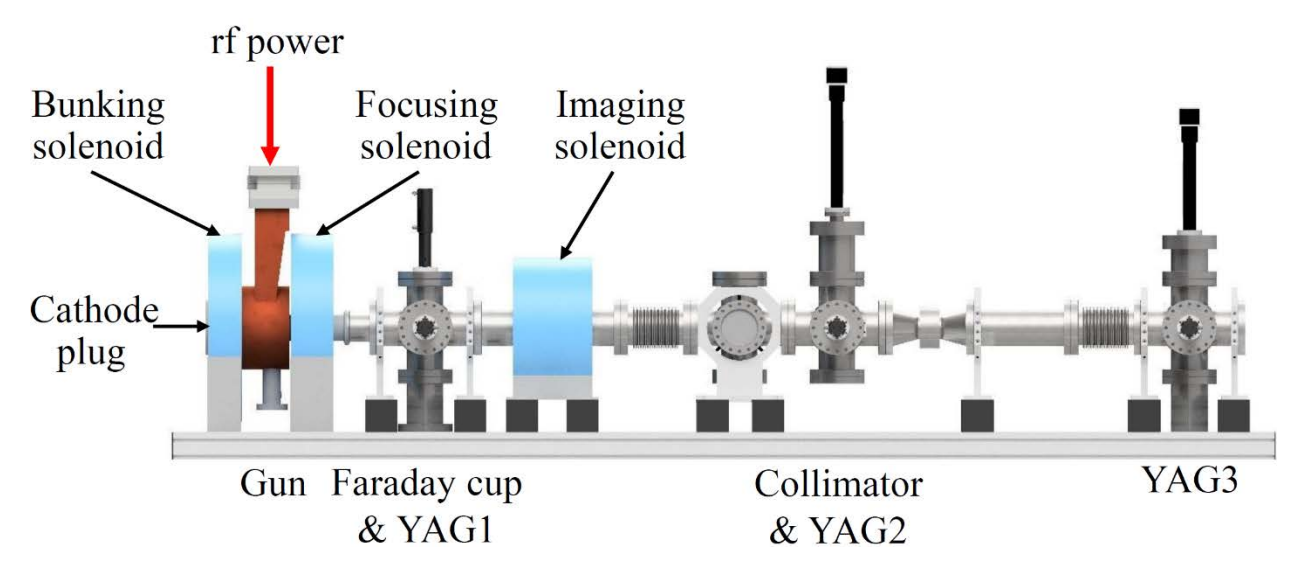


Figure. 2.1.4 Beamline diagram for the ACT showing all three of the solenoids and the location of the cathode with respect to the rest of the beam line and the three imaging stations. Not shown is the RF system before the gun [2]. It is not necessary to obtain permission to reuse this article or its components as it is available under the terms of the <u>Creative Commons Attribution 4.0 International license</u>.

after being focused by both solenoids. These collimated electrons are then imaged in the YAG3 plane which is 2.45 m away from the origin. YAG3 images are diagnostically the most important, giving the clearest image of the emitting cathode surface at largest magnification (~10) [1].

Not shown in Figure 2.1.4 is the RF system needed to power the ACT. The system consists of a L band (1.3 GHz) klystron with maximum output power of 2.5 MW. This is directed through the waveguide network into a circulator which is a three-port device that diverts the reflected power as to not damage the waveguides or klystron. There is also a directional coupler that is used to measure the RF waveforms needed to calculate the applied field during power conditioning to the operating point. This is explained more in CH3.2. The directional coupler measures the field using a RF pickup that is placed outside of the radiation bunker. The attenuation due to the waveguide network is 0.2 dB, RF pickup depending on the power level can either be 10 dB or 15 dB and the directional coupler itself has 60 dB attenuation. The ACT power limited field is 100 MV/m for a planar geometry when using maximum output power of 2.5 MW. The ACT's output power increases by 208.5 W per 1 MV/m of conditioning field [1,2,3].

## 2.1.1 Optimal Conditioning Procedure

To achieve the best performance out of a field emission cathode, the most important thing is the conditioning procedure. This process was developed in Ref. [2]. It is a general procedure and can be seen as a standard methodology of conditioning of a FEC to its operating point. The first step is to slowly increase the field until emission is observed on an imaging screen. This determines the turn-on field. Before increasing to the next gradient point, the breakdown rate must be lower than 10<sup>-4</sup> breakdowns per second (but initially can be as high as 10<sup>-1</sup> breakdowns

per second right after the new higher gradient point was set). The interval between maximum applied fields for each QE curve is typically 5 MV/m to maintain the continuous "slow" pace. For cathodes that may not be able to handle extremely high fields, such gradient interval step can be 1-2 MV/m. The choice is made based on the breakdown rate that is continuously monitored. Once the breakdown rate is lower than 10<sup>-4</sup>, the QE curves are taken on the reverse until the point where the charge on the Faraday cup is below the detection threshold. This low breakdown rate is necessary as, when a breakdown occurs during the process of taking the QE curves, that data must be discarded, and the QE data collection must be restarted. A good rule of thumb is that the interval between data points in the QE curves should be about 0.1 MV/m. Additionally, each data point should have 10 individual pulses taken before moving to the next data point so that there is a good average field and average charge as these data points can fluctuate slightly from pulse to pulse. After the QE data is obtained, imaging should be done.

Due to the large energy spread of the field emission cathode, the gun solenoid settings must be continuously optimized to keep the capture ratio at over 95%. Changing the magnetic field by only a few hundred gauss can drop the capture ratio on the Faraday cup from 95% to as low as 30% as seen in **Figure 2.1.5.** This figure shows the capture ratio at a single gradient as a

function of magnetic field when compared to simulation results. The same trend is shown when modeling the particles in ASTRA.

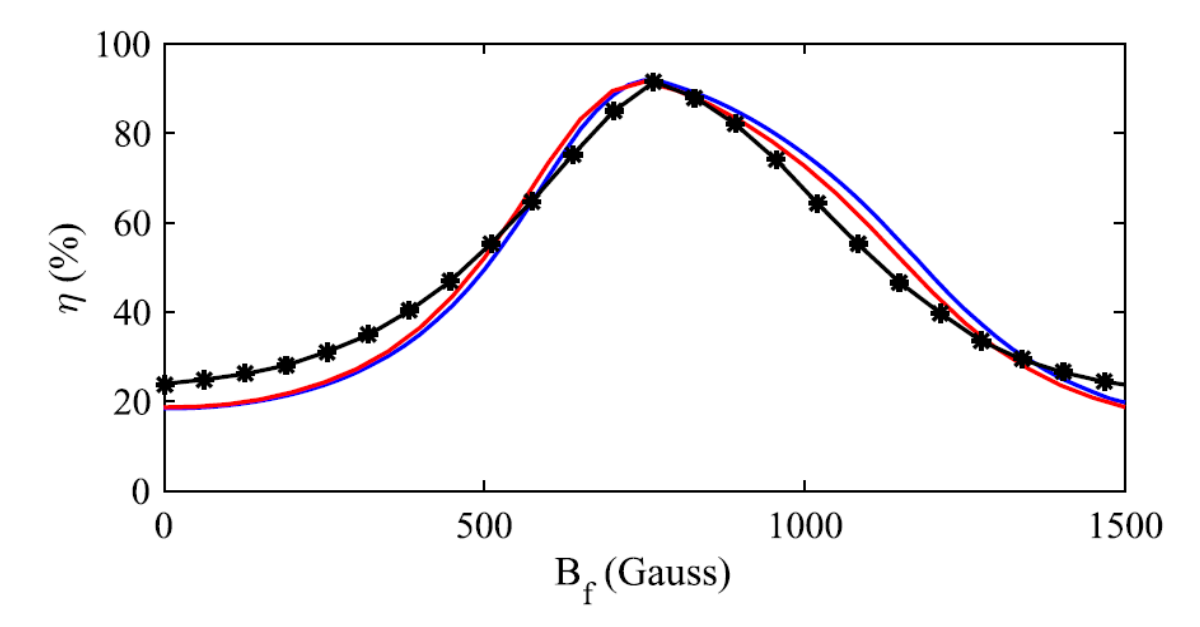


Figure. 2.1.5 Capture ratio for UNCD for  $E_h$ = 43 MV/m (black line) compared with simulation values for capture ratio of  $\mid E_h \mid$  (red line) and  $E_{h \text{ max}}$  [2]. It is not necessary to obtain permission to reuse this article or its components as it is available under the terms of the Creative Commons Attribution 4.0 International license.

The capture ratio does seem to change slightly when increasing the field by only a few percent of the magnetic field as shown in **Figure 2.1.6.** To maintain an approximately constant capture ratio, the magnetic field has to increase by almost 25%.

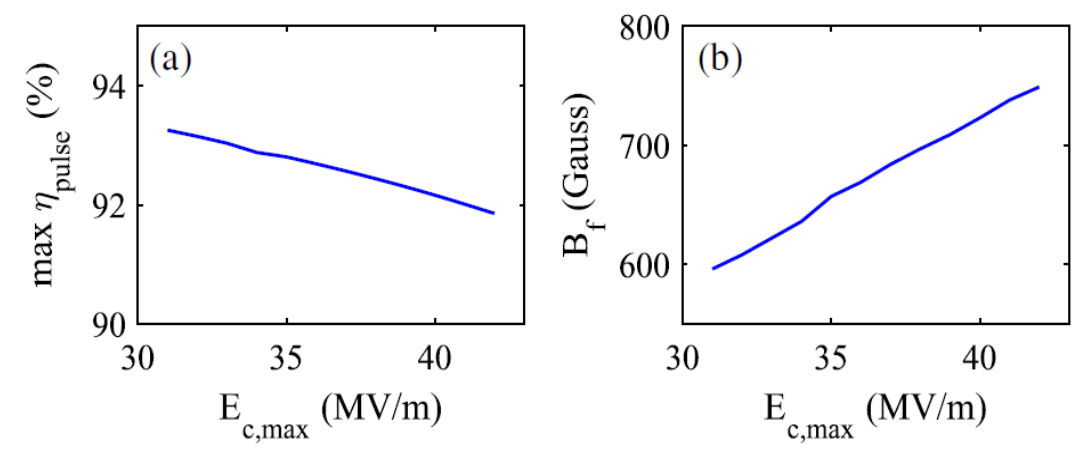


Figure. 2.1.6 (a) maximum capture ratio as a function of conditioning field  $E_c$  and the corresponding optical magnetic field of the focusing solenoid on the ACT beamline (b) [2]. It is not necessary to obtain permission to reuse this article or its components as it is available under the terms of the <u>Creative Commons Attribution 4.0 International</u> license.

However, when keeping this conditioning procedure in mind and optimizing it for every individual cathode, it is this precision and performance of the FEC itself that allows for the development of high resolution computing toolkits that gave life to discovering new field emission dynamics that are discussed in more details in <u>CH4.1</u>

**REFERENCES** 

# **REFERENCES**

- [1] J Shao, Investigations on rf Breakdown Phenomenon in High Gradient Accelerating Structures, Springer Theses (2018)
- [2] J. Shao, M. Schneider, G. Chen T. Nikhar *et al*, Phys. Rev. Accel. Beams **22**, 123402 (2019)
- [3] M. Schneider, E. Jevarjian, J. Shao and S. V. Barnyashev Review of Scientific Instruments **92**, 053305 (2021)

#### **CHAPTER 3 TECHNICAL RELEVANCE**

This chapter outlines the series of software tools named the FEmaster series. This consist of four parts: 1) FEgen for time dependent field emission beam dynamics, 2) FEbeam for converting high power hardware raw signal to charge and electric field representation, 3) FEpic for image post processing of experimental electron emission micrographs, and 4) FEbreak for data experimental control and data acquisition for high power RF systems conditioning, including structure breakdown rate analysis. These four software in tandem provide the most comprehensive set of software for developing the next generation of RF injectors. The goal of the authors was to provide the software to the community as open source so that they became the standard unit of measure when comparing FEC performance and dynamics across different cathode geometries, materials, and injectors. The need for this software became evident through attending variety of conferences, most importantly IVNC 19. Many groups use in-house or proprietary software to analyze and model their field emission sources and, due to different assumptions in those models, there is inconsistency when comparing results between different groups. Note that FEpic was developed by another student in the group, Taha Posos. Therefore, this thesis does not claim the development of FEpic and only briefly describes the mathematical concept behind it, and later showcases its application to RF microscopy analysis.

# CHAPTER 3 CREATION OF THE FEMASTER SERIES: A COMPREHENSIVE FIELD EMISSION BEAM ANALYSIS AND MODELING TOOLKIT.

During the development of the experimental procedure, it was determined that a comprehensive field emission analysis toolkit was required to conduct analysis in a timely manner. The current toolkits available for both simulation and data processing were either custom-built for specific applications or proprietary software that was very expensive, such as MICHELLE of TechX's VSim. This led to the development of the FEmaster series which is a comprehensive field emission beam analysis and modeling toolkit that is open-source freeware.

The FEmaster series currently consist of four subunits: FEbeam, FEgen, FEpic, and FEbreak [1,2,3,4]. All the softwares are modular designs and are incorporated into a single MATLAB/Python hybrid script that can be run as one singular unit. Each component of the FEmaster series can be a self-contained program. However, they also work as a cohesive unit as seen in the workflow diagram in **Figure 3.0.1.** 

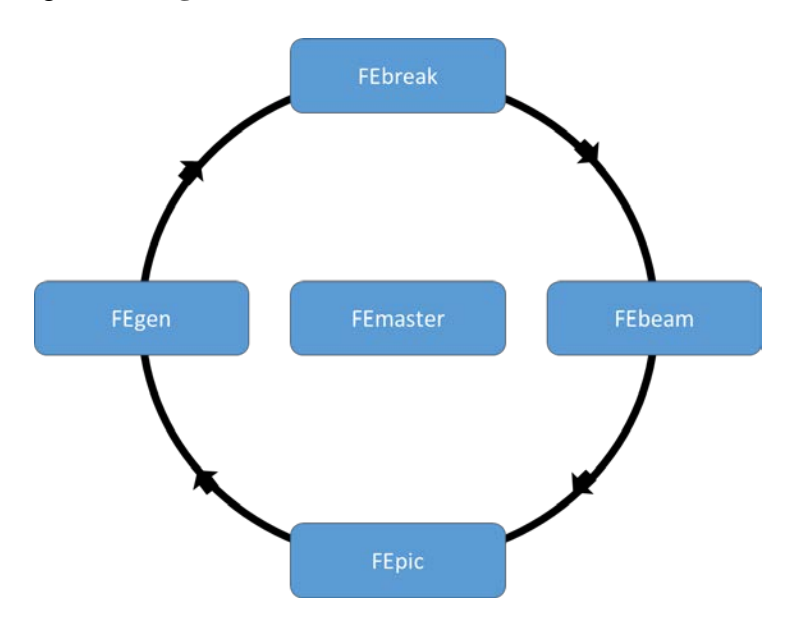


Figure. 3.0.1 Workflow diagram of FEmaster.

FEbeam is a data processing pipeline that allows for characterization of FEC's in an RF or pulsed DC environment [1].

FEgen is a field emission initial particle distribution generator based on the timedependent Fowler-Nordheim equation. FEgen work is ongoing as it will be expanded to account for higher order models beyond Fowler Nordheim, such as: semiconductor emitters, nonplanar geometries, work function mapping, and temperature effects [2].

FEpic is a fast electron emission image processing algorithm that can determine the number of emitters by analyzing electron emission patterns on YAG screen images.

Finally, FEbreak is a breakdown statistics algorithm designed to not only be able to calculate the breakdown rate, but also automate the conditioning cathodes procedure such as the one presented in [4] **CH2**.

## 3.1 FEgen:

The following work is taken from FEgen currently on archive as see in Ref [2]. As field emitters are poised to become the preferred electron source for next-generation electron accelerators and other vacuum electronics microwave devices are moving up in operating frequency for higher peak power rating and compactness [4–9], a computational toolbox needed be developed to realistically model their particle dynamics. Unlike in photoemission where an ultrashort high power density laser pulse is synchronized (in other words, phase matched) with an rf/microwave drive signal, electrons are generated by and interact with the rf/microwave drive cycle in a much wider phase window, regardless of whether a field emission cathode is operated in an ungated or gated fashion (by means of a physical gate electrode, harmonics mixing, or multicell gun design). An extended interaction phase window is of paramount importance to correctly reveal the longitudinal phase space of the resulting beam, which may promote delayed emission and secondary effects in the injector ultimately leading to beam loading, multipacting, and cathode field screening effects.

Compactness of a high frequency system (and the corresponding small emitting area of an electron source required to emit high charge) poses challenges in regard to correctly tracking and accounting for vacuum space charge effects and beam expansion/explosion. Currently, indemand beam tracking software that is capable of accounting for space charge effects, such as ASTRA,[10] IMPACT-T,[11] or GPT,[12] lack a native particle distribution generator suitable for field emission analyses. There are costly PIC codes, VSim [13] and MICHELLE [14] for example, that account for the space charge effect yet contain field emission models based on the conventional dc Fowler Nordheim equation. Such PIC codes do not incorporate the time dependence necessary for rf modeling. In addition, the exact mechanism of how MICHELLE and VSim determine their field emission distributions is proprietary.

This work aimed to engineer a distribution generator function using Python by implementing the time dependent Fowler-Nordheim equation, allowing for the observation of temporal/phase (and thus complex longitudinal) beam processes. Furthermore, our freeware generator is available as open source which is advantageous to proprietary codes or custom-made add-ons to existing beam tracking software. The generated distributions can be directly translated into both ASTRA and GPT. FEgen can be found on GitHub and its principle is detailed below. In particular, this work provides the ability to design and simulate transversely inherently shaped beams using array field emission cathodes providing new means for improving wakefield structure or plasma accelerators [15]

#### 3.1.1 Momentum Distribution

The momentum distribution here is based on an isotropic distribution, defined in the ASTRA's user manual as arising from the emittance on the cathode surface as the electrons tunnel through the barrier [10]. This results in a momentum spread that is uniformly distributed over a half sphere, where the base is the surface of the cathode. This is referred to as an isotropic distribution which is defined as any distribution function azimuthal symmetry; in this case, particles distributed over a uniform half sphere centered at the origin. To create the isotropic momentum distributions, first the maximum energy of each particle is calculated. Using NumPy random normal distribution function, a three-dimensional array of values with a normal distribution between -1 and 1 in each dimension is created to serve as unit vectors for each particle's momentum in the x, y, and z direction. In **Figure 3.1.1**, the absolute value of the z dimension of the unit vector array is multiplied by the maximum energy for a particle, given that momentum in the z direction must be positive.

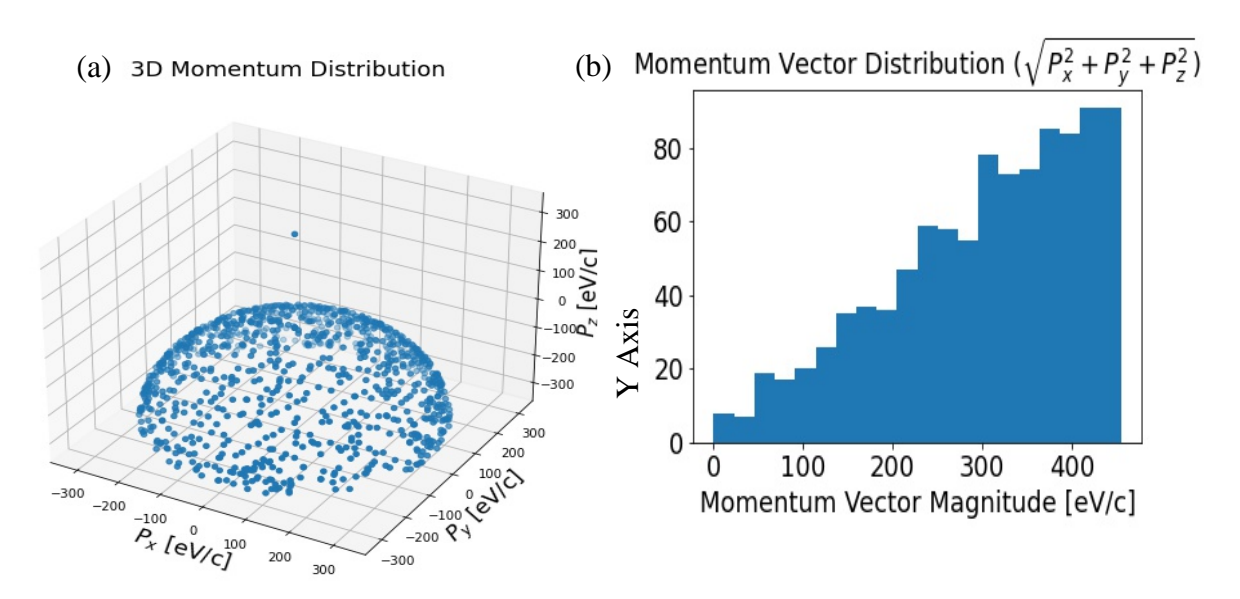


Figure. 3.1.1 (a) isotropic distribution in momentum space. The single point above the sphere is the test particle where all of the momentum is in the z direction; (b) the distribution for the magnitude of the momentum vector [2].

The magnitude of each particles momentum vector is then calculated and used to create an array of each particles energy which is then used in SciPy's Statistical Kolmogorov-Smirnov test (kstest) to generate a p-value indicating the uniformity of the energy distribution by testing against SciPy's Statistic Uniform distribution function. The given p-value is then compared to a significance level of 0.01. When the generated momentum arrays meet this significance condition, the momentum values are accepted and stored in the program to later be written into the output file along with the spatio-temporal components.

## 3.1.2 Spatio-temporal Distribution

**Figure 3.1.2a** illustrates how the spatial radial distribution is uniform over a given radius. For FEgen, NumPy's random distribution was used to produce the radial distribution, as illustrated in **Figure 3.1.2b**. This conceptual difference does not affect the resulting individual distributions of the x and y coordinates as clearly emphasized by **Figure 3.1.2c and 3.1.2d**.

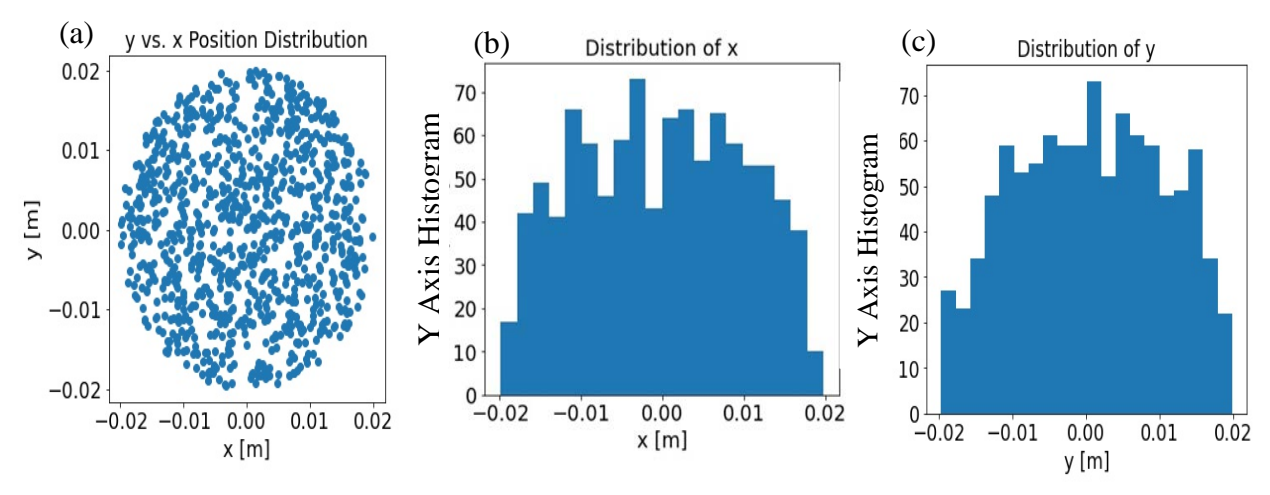


Figure. 3.1.2 (a) Radial distribution calculated using (b) and (c) compare between x and y distributions obtained FEgen [2].

The FEgen has additional features such that, beyond having a single emitter, one can design a variety of emission patterns to simulate custom emitter arrays. A user can pick not only the radius of the emitter but also design an emitter grid and a custom pattern of emission points.

An additional benefit is if the user knows the total charge of the beam or the total charge over the entire emission pattern region, FEgen can calculate then the charge for each emitter.

This is useful in the case of simulating an emission grid of only a few emitters to represent a uniform emission which may have thousands of emitters on the cathode surface to maintain the ratio of emission area to charge to accurately simulate the space charge forces on the beam downstream. The interface of the initial particle distribution FEgen, containing all of the aforementioned features, is shown in **Figure 3.1.3**.

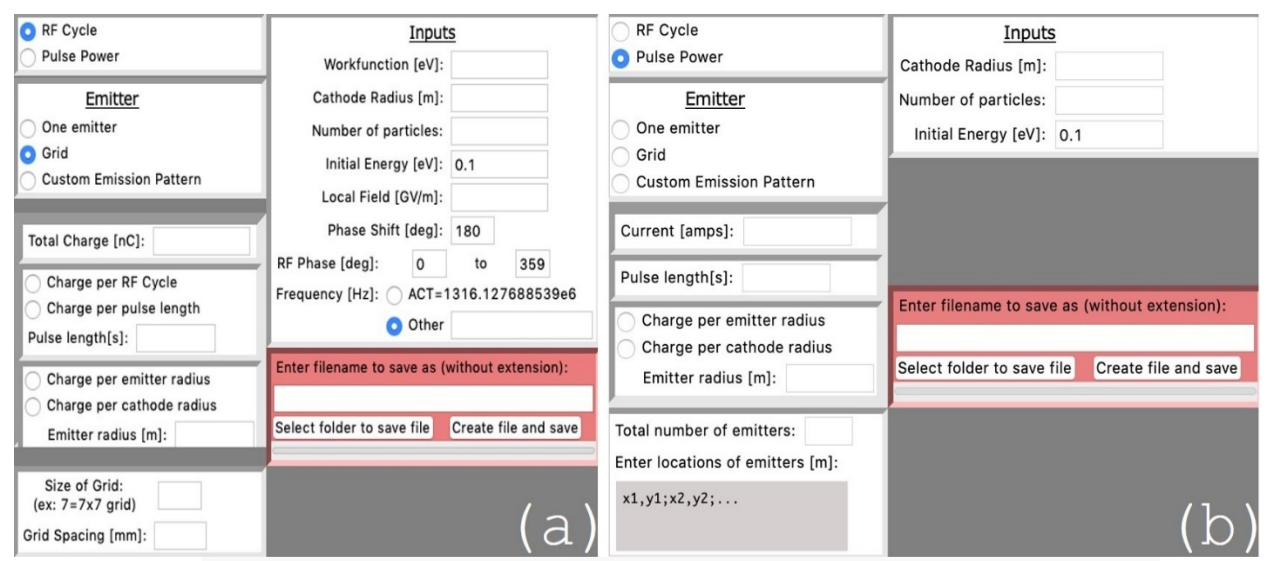


Figure. 3.1.3: FEgen interface for initial particle distribution generation. Functionalities include 1) rf and dc pulsed power environments, ability to design 2) uniformly spaced grid of emitters and 3) custom grid of emitters. Note Pulsed power function uses the pulse length of a dc system and the current to calculate the charge. As in any dc environment, the output current is constant with respect to time and does not follow the Gaussian-like distribution associated with the Fowler-Nordheim equation containing time varying electric field. FEgen interface functionality for (a) rf and (b) dc pulsed power environments [2].

The temporal distribution is determined upon whether the field emission source is operated in a dc pulsed power (dc) or rf (ac) environment. In the dc environment, the field emission current is constant with time. Therefore, the temporal distribution follows a uniform distribution where the output charge is found by inputs for the pulse length and current. In the rf

environment, the Fowler-Nordheim equation is time-dependent. When averaged over an rf cycle, the Fowler-Nordheim equation is transformed into a form that reads [16]

$$I_F(t) = \frac{1.54 \times 10^{-6} \times 10^{4.52*\phi^{-0.5}} A_e [\beta E_c(t)]^2}{\varphi} \times Exp\left[\frac{-6.53 \times 10^9 \varphi^{1.5}}{A_e [\beta E_c(t)]}\right]$$
Equation 3.1.1

The external electric field is modeled as a time variant sinusoidal oscillation which is a result of only considering the longitudinal component. Eq. 3.1.1 is then fitted to a Gaussian distribution to determine the mean and standard deviation over the emission phase as specified by the input parameters (exemplified in **Figure 3.1.4**).

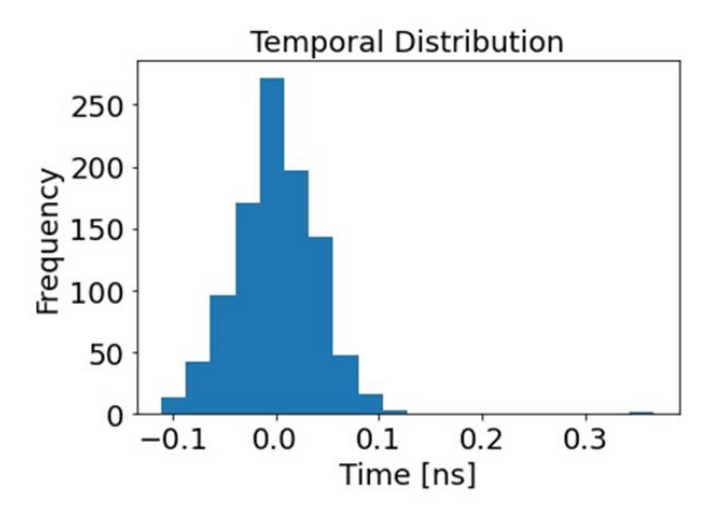


Figure. 3.1.4 Temporal distribution [2].

Generally speaking, there is no intrinsic gating in field emission, and the current is allowed to emit over 360° of the rf cycle, and only electric field strength in Eq. 1 dictates when the emitting charge quenches. On the other hand, Eq. 3.1.1 is highly non-linear, and it is therefore hypothesized that the emission phase window is much shorter than 360°, often assumed [9] to be equal to 60° (±30° around the rf cycle electric field crest). This is of course not a fundamentally defined threshold, and FEgen interface offers to input a specific rf phase where the emission to occur thus allowing, e.g., for finding best agreement between simulations and experimental data.

The other important input parameters are the work function of the cathode material, initial energy spread at the cathode surface, the phase shift and frequency of the gun, and the local field on the cathode surface (the product of the applied field and the field enhancement factor β). The FEgen code was originally intended for the Argonne Cathode Teststand (ACT) where the default frequency is the L-band operational frequency of 1.316 GHz. The initial energy distribution at the cathode surface is defaulted to 0.1 eV, as for most materials the initial energy distribution is a fraction of an eV.01 [17] As this current model uses the Fowler-Nordheim equation, all particles are assumed to emit at z=0, which is the location of the cathode surface in the simulation given that the cathode surface is of a planar geometry. Even so, the current extent of FEgen allows for very accurate simulations which match with our experimental results which can be seen more in CH4. Though the next session will discuss of this project, it has been spun off into another thesis for new graduate student in the advisor's group who was formerly an undergraduate assistant of the author.

# 3.1.3 Outlook modeling of non-Fowler Nordheim conditions

A FEgen in its current form is limited to only being able to model planar geometries based on Fowler Nordheim which assumes a metallic cathode. As seen in CH5, there is the need to explore different geometry emitters for their ability to not only produce pattern beams but also probe the transition region between classical Fowler Nordheim and new field emission regimes, explored in more detail in CH4. The first step for these nonplanar geometries is to consider that there will be surface potential across the surface of the material as a function of z which will cause a redesign of both the momentum and spatial temporal distributions. The next generation of field emission sources, as shown in the application example, are most likely to be semiconductor materials, such as those made of carbon nanotubes and diamond materials [18–

25]. Recent results have shown a divergence from the classical Fowler Nordheim conditions [20,24–26], which is attributed to the current model failing to account for an emitter being a semiconductor. Future work will implement the semiconductor effects using the Stratton-Baskin-Lvov-Fursey formalism, [25] expanding into the rf environment, temperature, and patchy/varying work function effects.

### 3.2 FEbeam:

FEbeam was originally designed by the author's collaborator, Jiahang Shao at Argonne National Laboratories, as part of the Argonne Wakefield accelerator for the Argonne Cathode Test-stand. Originally, FE beam consisted of 17 different sub algorithms to perform data processing [1]. During the development of the conditioning process in **CH2**, it was determined that a similar pipeline must be created with a modular design. There was also a need to automate this process as each of the 17 different steps had to be repeated for each data set, potentially taking multiple days of operator time to fully process a complete set of data.

The modular design allowed for the development of higher order analysis such as the knee point algorithm to analyze non-Fowler Nordheim conditions that will be explored in more detail in <u>CH4</u>. FEbeam was originally designed for the ACT though there is only one section of the code which is specific to the RF system used in the ACT. This could quickly be changed to any new RF system as was done later for the C-band RF system in <u>CH5</u>.

A single graphical user interface (GUI) conveniently combines and cross-links all components together. **Figure 3.2.1** shows the workflow map of all of the components necessary to take the raw data and convert it to analyze and compare the field emission cathode performance. The green boxes in **Figure 3.2.1** are the input data and parameter files, the blue

boxes represent a simplified version of the internal pipeline for data processing, the red boxes are the output files, and the yellow boxes are the output figures.

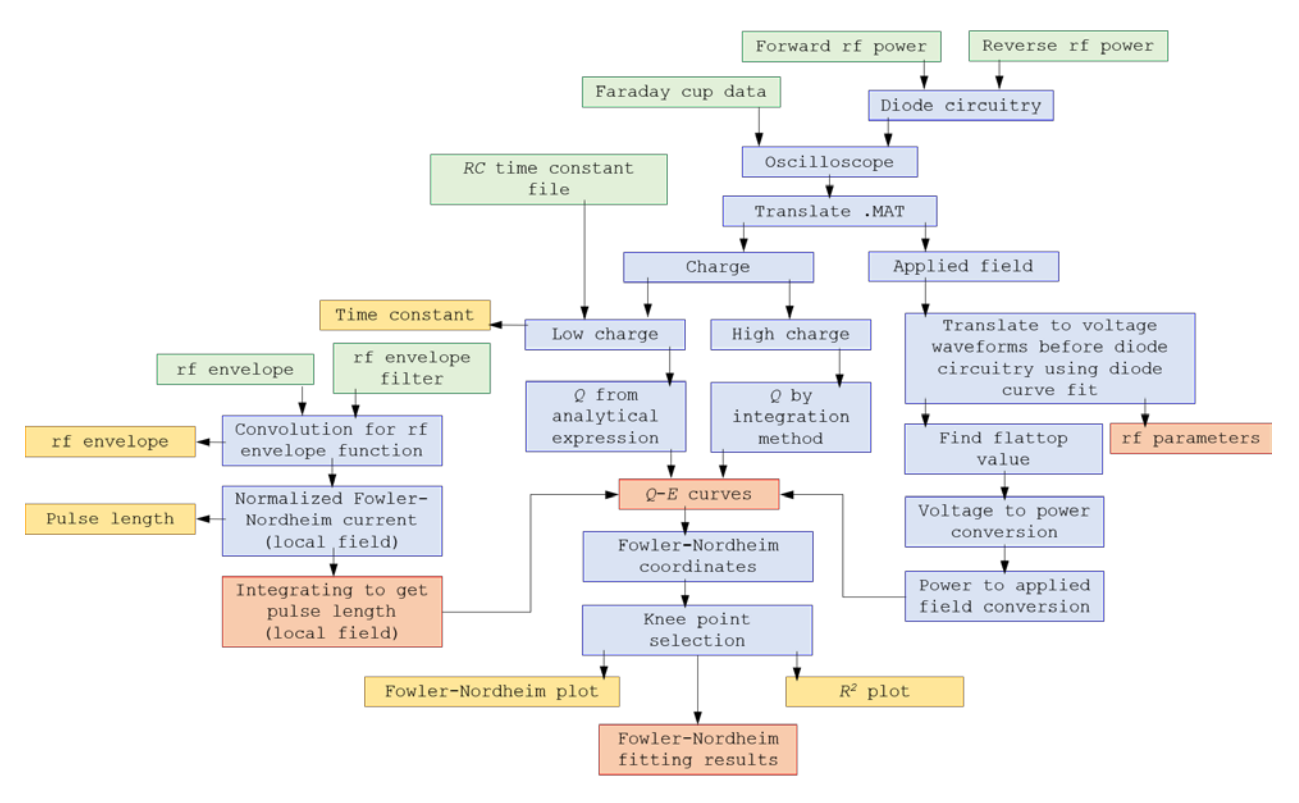


Figure. 3.2.1 FEbeam's workflow map showing how the data processing algorithm (in blue) takes the raw data from input files (in green) to the output data (in red) and the output figures (in yellow) [1]. AIP Publishing grants a license for all orders.

## 3.2.1 Obtaining Q-E Curves

The raw data used to calculate the field emission characteristics is obtained from the oscilloscope in a CSV format consisting of the voltage waveforms for the Faraday cup, forward power, and reverse power. Each CSV file is a single point in the Q-E curve where each point consists of 10 individual pulse shots. The opening GUI screen, Select Raw Data Files, is shown in **Figure 3.2.2a**. This allows the user to select the folders in which the raw CSV files are located. The user then selects the files that they want to process in the GUI window. This screen has the options for image processing and postprocessing that are discussed in further detail in **Section 3.2.2**.

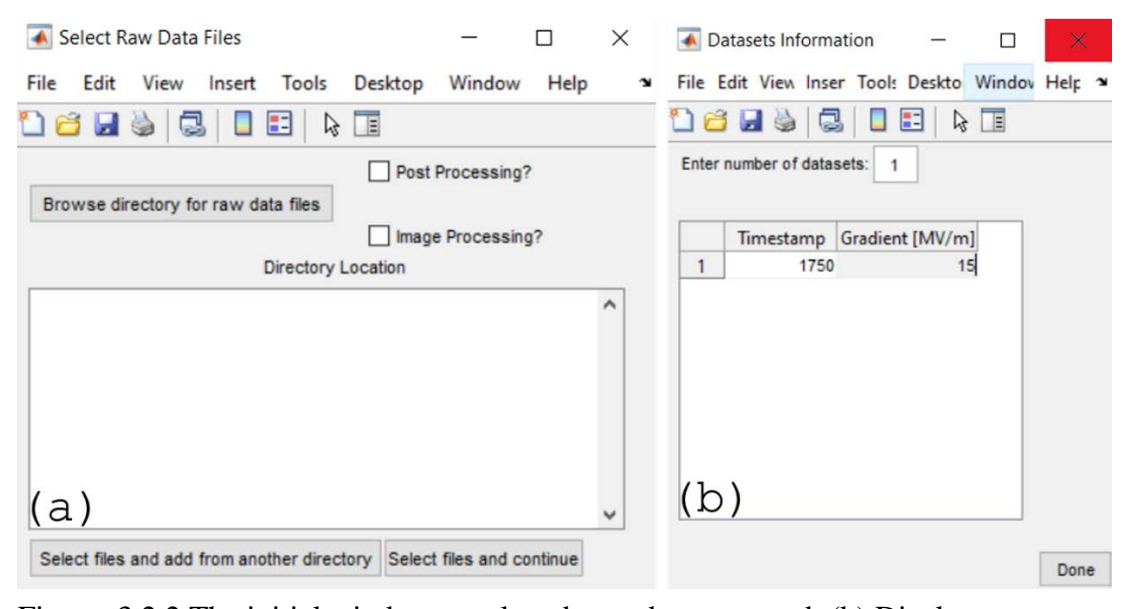


Figure. 3.2.2 The initial window to select data to be processed; (b) Display screen that allows for the timestamp of the dataset to be associated with the conditioning gradient that will be later used to rename and group the files. AIP Publishing grants a license for all orders.

The default name setting for the CSV files groups is derived from the experimentally achieved conditioning gradient. For ease-of-use, FEbeam renames the files based upon the conditioning gradient for that dataset as shown in Figure 3b, Datasets Information. The conditioning field is the desired field that the cathode was conditioned to for a given dataset.

Note that the conditioning field is used solely for naming convenience and that the applied field is the actual measured value. After the datasets have been selected, renamed, translated into MATLAB data files (.MAT format), the rf parameters need to be set in the FEbeam screen, as shown in **Figure 3.2.3**. These parameters are used to translate the raw data into Q-E curves after each individual file is grouped based on the conditioning gradient entered in Dataset Information (see **Figure 3.2.2b**). Parameters include options for a low charge or a high charge case scenario, and for selection of the rf filter and rf envelope needed to calculate the pulse length.

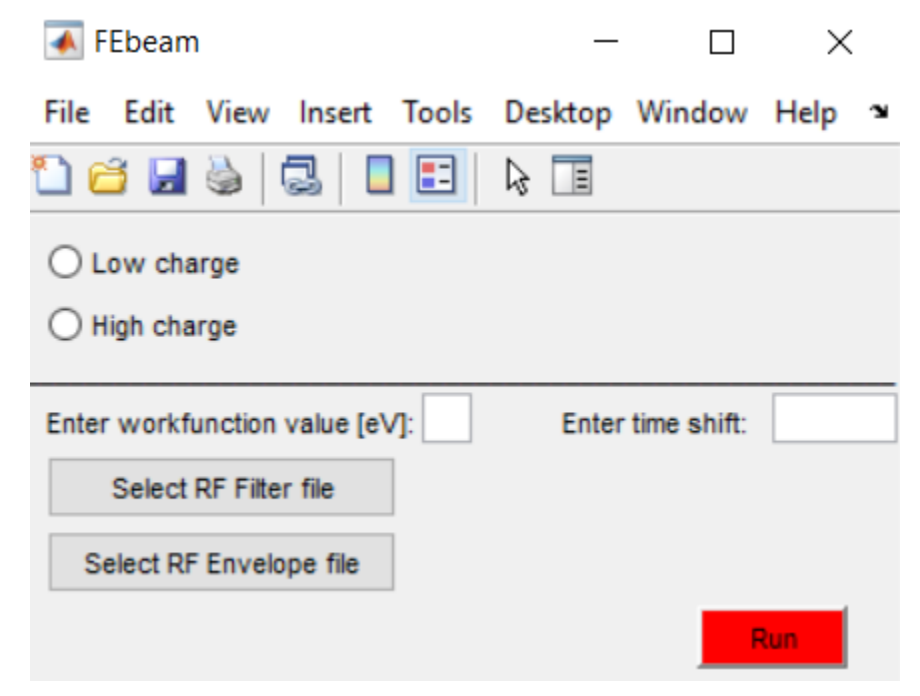


Figure. 3.2.3 The main interface of FEbeam. The top portion sets the rf parameters to translate the raw data into Q-E curves. AIP Publishing grants a license for all orders.

The difference between the high and low charge scenarios refers to the terminating impedance on the oscilloscope in the Faraday cup circuitry. The low charge case uses the impedance of 1 M $\Omega$  as the larger impedance allows for larger voltage drop read by the scope and hence higher sensitivity to lower charge beams. However, the Faraday cup signal length will increase by a few orders of magnitude. As a result, rf pulse and Faraday cup signals cannot be

captured simultaneously. Therefore, Faraday cup signal is recorded to only calculate RC time constant  $\tau$ RC as illustrated by the interface screen shown in **Figure 3.2.4.** The charge in the Faraday cup for the low charge scenario can be then found using the top expression in **Eq. 3.2.1**. When calculating the time constant, the user selects a range to use as back subtraction.

The lower portion calculates the pulse length of the function of the local field and calculates the emission envelope using the Fowler-Nordheim equations, based on the work function entered noise floor and a range to calculate the RC time constant. Recommended values of 90% and 10% are the minimum recommended to mitigate calculation errors and are illustrated in **Figure 3.2.4**.

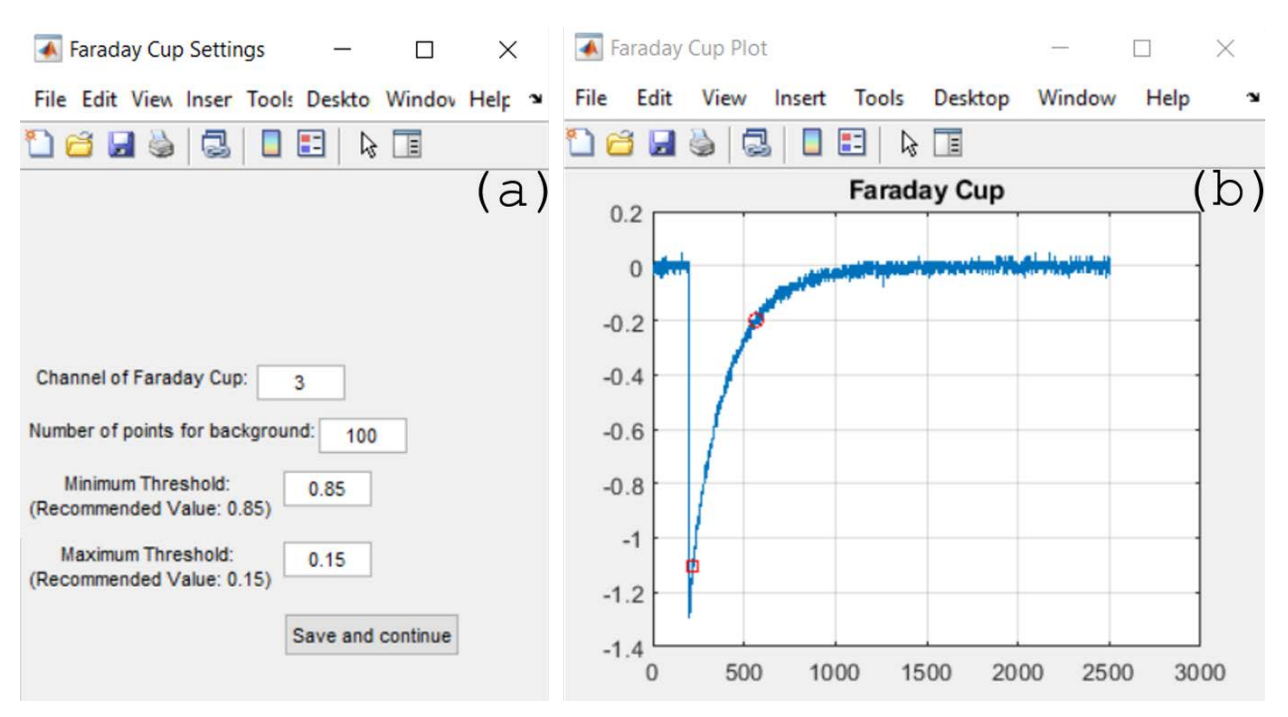


Figure. 3.2.4 (a) Faraday Cup Settings display interface for selecting the time constant for the low charge case. (b) Plot where red square and circle denote the location of the minimum and maximum threshold values corresponding to 90% and 10% of the maximum value [1]. AIP Publishing grants a license for all orders.

In the high charge case, which uses the terminating impedance of 50  $\Omega$ , the charge is directly calculated by integrating the signal from the Faraday cup over the range specified in the

settings window (see **Eq. 3.2.1**). In the Parameter File Settings (see **Figure 3.2.5a**), the operator selects which of the three channels represents the forward power, reverse power, and the Faraday cup signal. One then gets to enter which time integration range will be used to calculate the noise floor for the data. This integration range is used to calculate the charge collected. The final set of parameters associated with the specific rf system includes the attenuation factors due to the waveguides, the attenuators for the forward and reverse power, and the power to electric field conversion factor for the output power of a klystron.

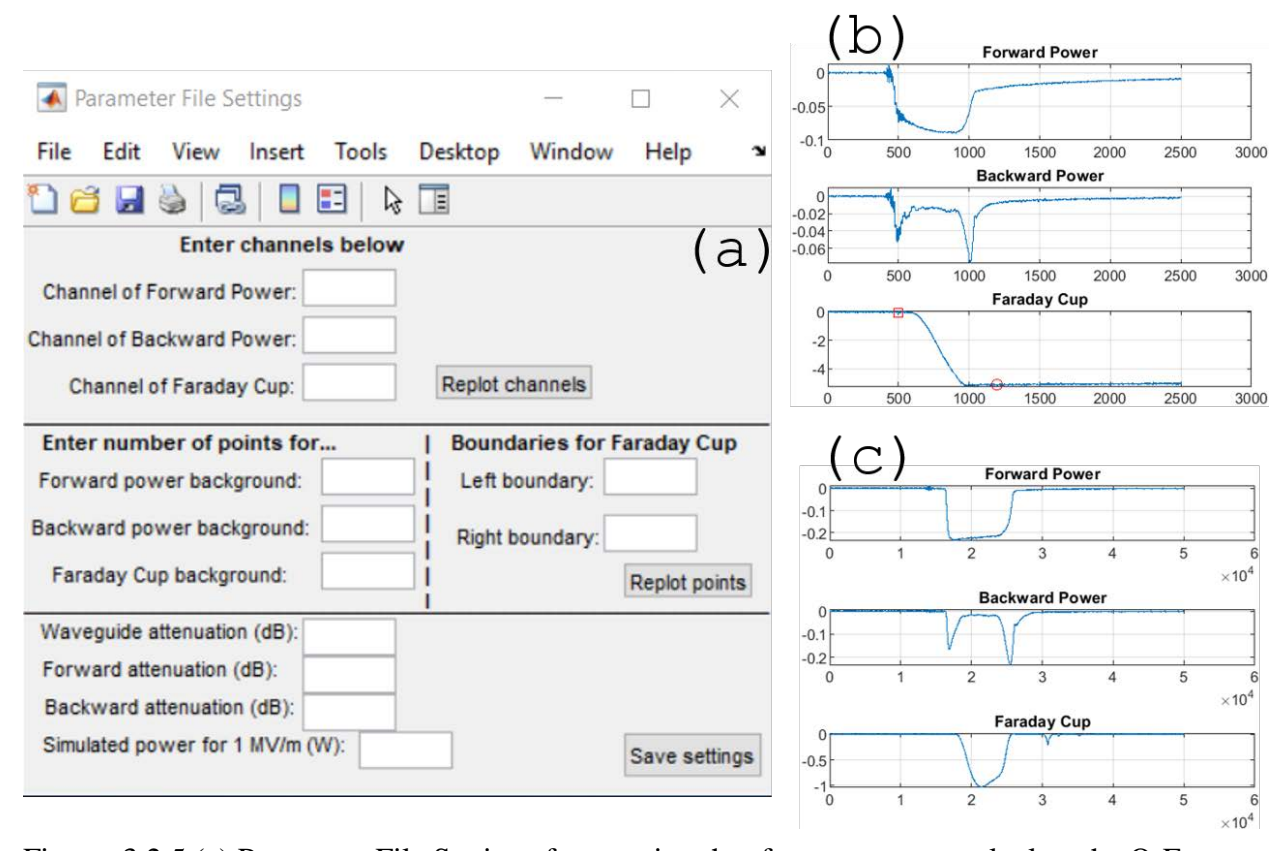


Figure. 3.2.5 (a) Parameter File Settings for entering the rf parameters to calculate the Q-E curves; (b) waveforms for a low charge scenario; (c) waveforms for a high charge scenario. Red marks denote the region that was considered in the Faraday cup to calculate the charge. AIP Publishing grants a license for all orders.

Remember for the ACT case, the waveguide attenuation is 0.2 dB, and the power conversion factor is 208.5 W of the input power corresponds to 1 MV/m of applied macroscopic field. The 208.5 W power conversion factor was obtained from SUPERFISH cavity simulation

and is valid for planar cathode geometry only. The forward and reverse power attenuators, depending on the experiment set up, are either 10 or 15 dB with an addition of 0.5 dB added to account for the filter on the attenuator. The settings window is the same for the high and low charge cases: **Figure 3.2.5b and Figure 3.2.5c** show the Faraday cup waveforms for the low and high charge case relaying the basic difference. Summarizing, the charge is calculated as follows:

$$\begin{cases} Q = -\frac{V_{FC}^{mean}}{Z_L} \tau_{RF} \text{ Low Charge} \\ Q = \frac{-1}{Z_L} \int_{t_1}^{t_2} V_{FC} dt \text{ High Charge} \end{cases}$$
 Equation 3.2.1

where VFc is the voltage waveform from the Faraday cup within the specified boundaries in the settings,  $\tau_{RC}$  is the RC time constant calculated for the low charge case, ZL is the load impedance, and t1 and t2 are the 10% and 90% boundaries.

If an oscilloscope with limited bandwidth is only available, it is still possible to measure envelope for the forward and reflected power in order to establish the applied field on the cathode. Figure 3.2.5b and Figure 3.2.5c demonstrate the result of this approach. For a narrow bandwidth scope, the raw forward and reverse rf signal picked up on the directional coupler installed on the waveguide near the L-band driving klystron was passed through a diode (Keysight 423B) circuit to modulate the frequency low enough that it can be read in by the oscilloscope. This step is not necessary for systems and facilities with access to a GHz scope and can be bypassed if necessary. During data processing, the raw forward and reverse power waveforms from the oscilloscope are translated back into their original form by fitting the diode waveform to a 7- order polynomial. These conversion equations [Eq. 3.2.2 and Eq. 3.2.3] for the ACT are as follows:

=-0.034+0.0477\*
$$V_{FP}$$
+6.617×  $10^{-4}$ \* $V_{FP}$ <sup>2</sup>  
+4.948×  $10^{-6}$ \* $V_{FP}$ <sup>3</sup>-5.411×  $10^{-8}$ \* $V_{FP}$ <sup>4</sup>+3.129×  $10^{-10}$ \* $V_{FP}$ <sup>5</sup> Equation 3.2.2

$$-8.789 \times 10^{-13} * V_{FP}^{6} + 9.65710^{-16} * V_{FP}^{7}$$

$$V_{RP}^{original} = [-0.159 + 0.07052*V_{RP} - 2.4 \times 10^{-5}*V_{RP}^{2}$$

$$+1.86 \times 10^{-5}*V_{RP}^{3} - 1.925 \times 10^{-7}*V_{RP}^{4} + 1.079 \times 10^{-9}*V_{RP}^{5}$$
 Equation 3.2.3
$$-3.028 \times 10^{-12}*V_{RP}^{6} + 3.37 \times 10^{-15}*V_{RP}^{7}]$$

where power waveforms for both the forward (FP) and reverse (RP) power have units of milliwatts in this equation.

To convert original voltage waveforms for the forward and reverse power into actual power, the following equations are used:

$$\begin{aligned} & P_{\text{F}} = V_{FP}^{\ original} * 10^{(\frac{ATT_{FP} - ATT_{WG} + ATT_{DC}}{10} - 3)} \text{ Equation } 3.2.4 \\ & P_{\text{R}} = V_{RP}^{\ original} * 10^{(\frac{ATT_{RP} - ATT_{WG} + ATT_{DC}}{10} - 3)} \text{ Equation } 3.2.5 \end{aligned}$$

where  $ATT_{FP}$  is the forward power attenuator,  $ATT_{RP}$  is the reverse power attenuator,  $ATT_{WG}$  is the waveguide attenuation, and  $ATT_{DC}$  is the attenuation for the directional coupler which, in this case, is 60 dB. The -3 term denotes the conversion from milliwatts to watts.

It is assumed that the rf pulse is a flat top; therefore, if we integrate over the forward power and then divide by half, this midpoint should be where the level of the flat top is, as shown by **Eq. 3.2.6**. This corresponds to the median applied field over that rf pulse. Time k corresponding to that midpoint is found from relation:

$$\int_{t_i}^{t_k} P_F dt = \frac{1}{2} \int_{t_i}^{t_f} P_F dt$$
 Equation 3.2.6

where t<sub>i</sub> and t<sub>f</sub> are initial/start and final/end time integration boundaries.

Finally, the applied macroscopic electric field can be found as:

$$E_h = \sqrt{\frac{P_F^k}{P_{factor}^{ACT}}}$$
 Equation 3.2.7

Where  $P_F^k$  is the power at time  $t_k$  measured in W as found from Eq. 3.2.7 and  $P^{ACT}_{factor}$  is the ACT power conversion factor equal to 208.5 W·m²/MV. The applied field and power conversion factor are imported from the Parameter File Settings, and labeled in accordance with the highest  $E_c$  achieved, called Eh.

Subsequently, each of the data points in the Q-E curve are combined into a single file. The next step is converting the Q-E curve into the Fowler-Nordheim coordinate representation to further extract the field emission characteristic parameters, the field enhancement factor  $\beta$ , cathode local or microscopic electric field  $EL = \beta \times E_c$ , and the effective emission area Ae.

# 3.2.2 Determining Fowler-Nordheim parameters:

According to the Fowler-Nordheim (FN) equation, the transient field emission current when the cathode field is positive  $(\cos(\omega t) > 0 \text{ as in } \mathbf{Eq. 3.1.1})$ . The emission profile can be approximated by a Gaussian distribution whose standard deviation  $\sigma$  depends on the maximum microscopic cathode field  $\beta |Ec|$ , as illustrated in **Figure 3.2.6.** 

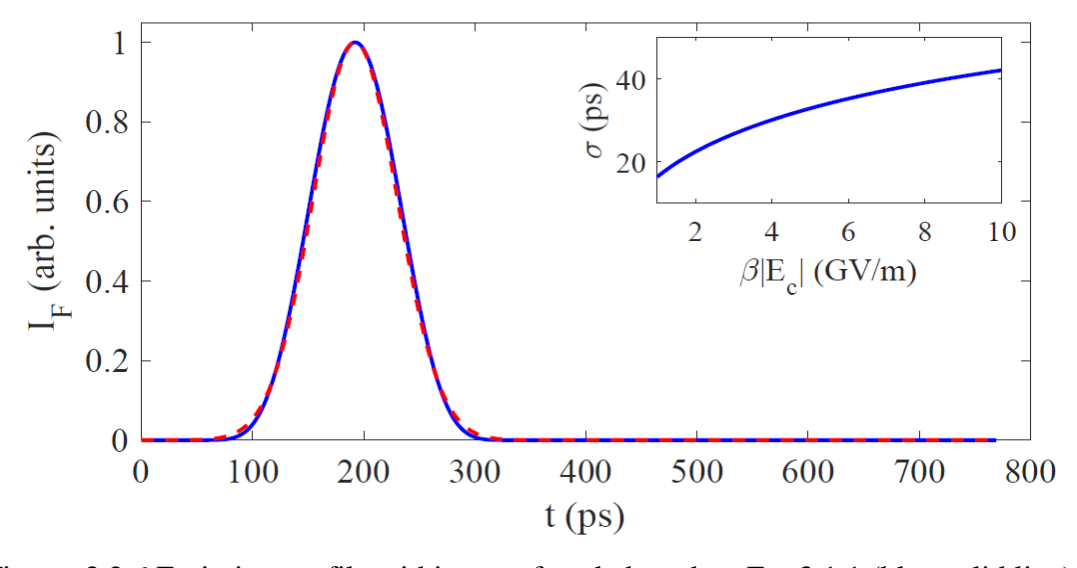


Figure. 3.2.6 Emission profile within one rf cycle based on Eq. 3.1.1 (blue solid line) and its Gaussian distribution approximation (red dashed line). Inset: The standard deviation of the Gaussian distribution as a function the maximum microscopic cathode field [1]. AIP Publishing grants a license for all orders.

To translate the Q-E curves into the Fowler-Nordheim coordinate, first, we determine the pulse length as a function of the local field. In the rf environment, the Fowler Nordheim coordinates are different than those in the dc environment: one plots  $log_{10}(Q/E^{2.5})$  as function of  $E^{-1}$  instead of  $log_{10}(Q/E^2)$  as function of  $E^{-1}$  (like it is in the dc environment). The extra factor of 0.5 is a result of averaging the Fowler-Nordheim current distribution over an rf cycle. The current distribution for the RF emissions phase window for Fowler-Nordheim in an rf environment is **Eq. 3.1.1**. The current distribution over the full RF cycle for Fowler Nordheim in an rf environment reads:

$$\overline{I_F(t)} = -\frac{5.7 \times 10^{-12} \times 10^{4.52 \times \varphi^{-0.5}} A_e [\beta E_c(t)]^{2.5}}{\varphi^{1.75}} \times Exp \left[ \frac{-6.53 \times 10^9 \varphi^{1.5}}{A_e [\beta E_c(t)]} \right]$$
Equation 3.2.8

where the external electric field is modeled as a time variant sinusoidal oscillation which is a result of only considering the longitudinal component as rf guns are TM mode cavity resonators.

To calculate the emission pulse length, envelope of the drive rf is necessary to be known. Predicted emission profile, as illustrated in **Figure 3.2.7**, is calculated for each  $|E_c|$ , where  $\beta$  is assumed to be constant and  $\sigma$  of the longitudinal emission profile is adjusted based on  $\beta |E_c|$ . It is seen that  $I_F$  (t) is highly sensitive to  $|E_c|$ , and emission pulse can be approximated by using a square emission profile of a length  $\tau$  with an average emission current of  $\overline{I_{F,max}}$  calculated by using  $|E_c| = E_{c,max}$  in **Eq.3.2.8**, as illustrated in **Figure 3.2.7**.

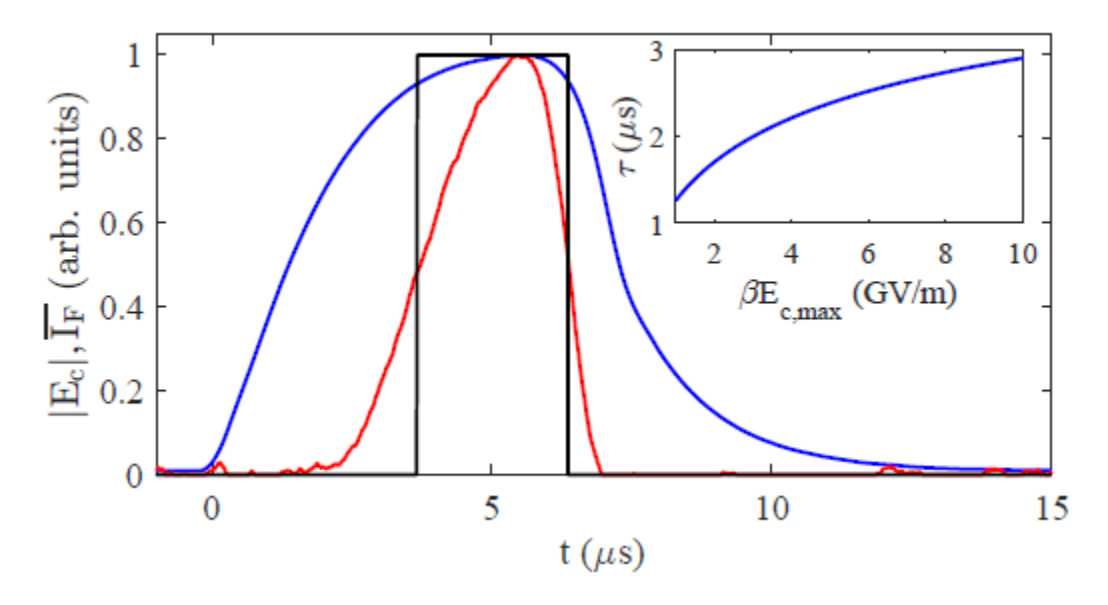


Figure. 3.2.7 Blue: the normalized cathode field amplitude |Ec(t)| measured by the rf pickup. Red: the predicted average emission current IF (t) by Eq. 9. Black: the square pulse approximation of the emission profile. Inset: The width of the square emission profile as a function of  $\beta Ec$ ,max. Reproduced from Ref.3. AIP Publishing grants a license for all orders.

The width of the square pulse is set as  $\tau = -\int \overline{I_F} dt/\overline{I_{F,max}}$  so as to keep the same charge. It depends on  $\beta Ec, max$ , as calculated by **Eq. 3.2.8** and illustrated in the inset of **Figure 3.2.7**. Note

that this calculation routine is done in the wider range of 0-50 GV/m for the local field to allow for convergence, but only the range of 0-10 GV/m is physically meaningful5, see **Figure 3.2.8a.** 

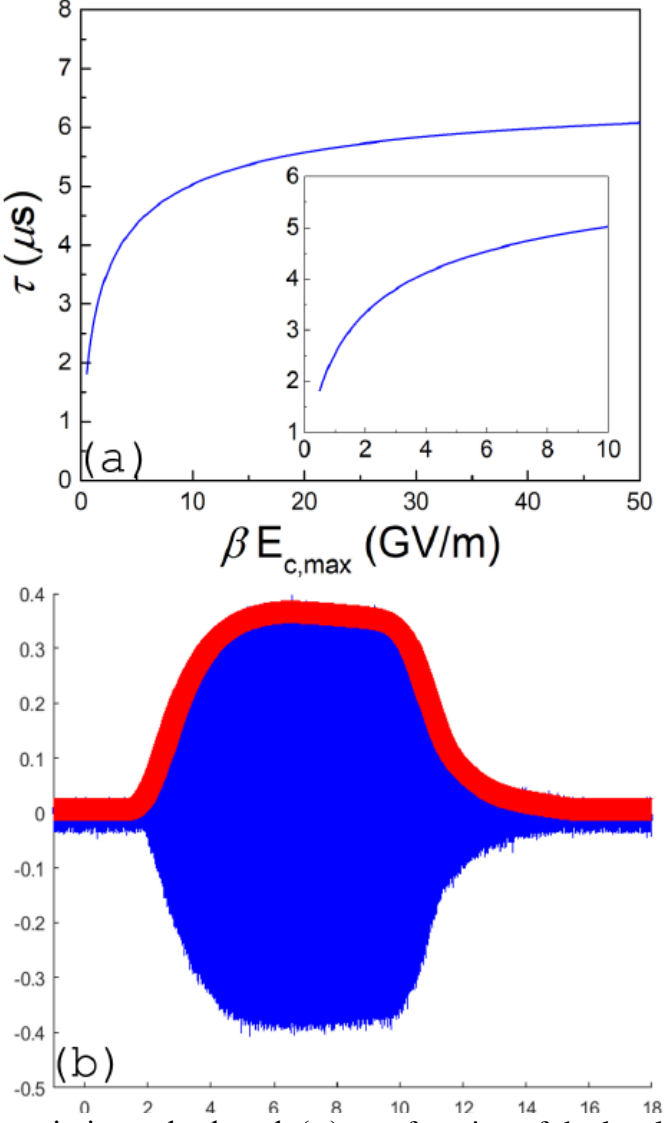


Figure. 3.2.8 The emission pulse length ( $\tau$ ) as a function of the local field plotted in the entire fitting range from 0 to 50 GV/m, inset is a zoom-in view of the pulse length within the physically meaningful local field range, from 0 to 10 GV/m. (b) In red is the rf envelope after frequency filter was applied, in blue is the actual pulse measured using pickup in the gun. AIP Publishing grants a license for all orders.

The red line in **Figure 3.2.8b** illustrates rf pulse envelope measurement. Additional smoothing is possible using an appropriate frequency filter function that can be obtained from the same scope. In MATLAB, the smoothing is applied using the convolution command called

conv. FEbeam exports the rf envelope and the pulse length as functions of the local field to the figures folder. Note that this calculation routine is done in the wider range of 0–50 GV/m for the local field to allow for convergence, but only the range of 0–10 GV/m is physically meaningful [27]

When the pulse length as a function of the local field is found, Q-E or I-E dependences can be plotted. It is often the case that the field emission characteristic plotted in Fowler-Nordheim coordinates deviates from straight line and multiple slopes can be seen; like the example seen in **Figure 3.2.9**.

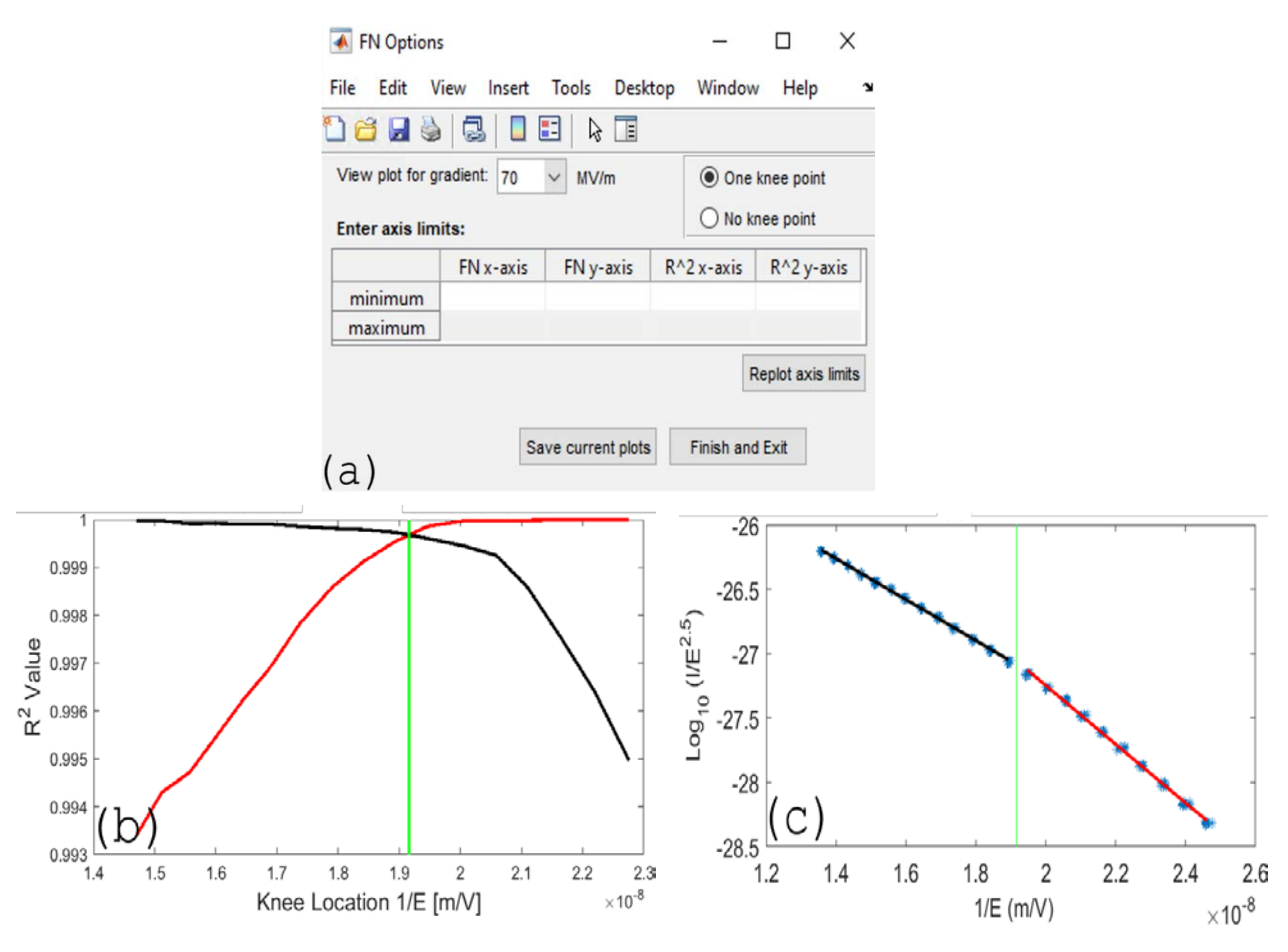


Figure. 3.2.9 (a) Display interface for the Fowler-Nordheim fitting; (b) example of an R2 plot; (c) example of a Fowler-Nordheim plot showing the fitting of the two different regions emphasizing the knee point. AIP Publishing grants a license for all orders.

Research and development the charge per rf pulse or rf cycle (and not the current used in regular dc or pulsed dc environments) is a significant figure of merit. The Faraday cup measures the charge per rf pulse. Once the rf pulse, as previously outlined, was calculated, the charge per rf cycle can be found at a given frequency and plotted as a function of the gradient. Same can be done to obtain the gradient dependencies of the average or peak current. For consistency with the convention in the rf linac Research and development, we plot here the relations between the rf pulse charge Q and the rf gradient E in Fowler–Nordheim coordinates. It is often the case that the field emission characteristic plotted in Fowler–Nordheim coordinates deviates from the straight line and multiple slopes can be seen; an example can be seen in **Figure 3.2.9b**. There is a number of physical mechanisms at play (e.g., vacuum space charge effect, [28] emitter bulk charge depletion, [20] or image charge effects [29]), and this is currently a subject of intense research in our laboratory.

Thus, a routine search for a knee point was developed based It is included as an optional data processing tool. The knee point is calculated using the Fowler-Nordheim as function of E<sup>-1</sup>. Since the pulse length is known to be relatively constant throughout conditioning, it does not change the selection of the knee point location when using the Q-E version vs. the I-E version of the Fowler-Nordheim coordinates. This only constitutes an additional y-offset. For the ACT, every data point of the Q-E measurement consists of 10 pulses (or, shots). Averaged values and an iterative fitting algorithm are used where the Fowler-Nordheim plot is split into two independent line segments shown in **Figure 3.2.9c**.

The first line (red line) initially only considers the first three data points and iterates until it fits all but the last three data points. The second line (black line) consists of the remaining points not fit by the first line. The R<sup>2</sup> values of each line are recorded for each step in the

iteration. The knee point is chosen for the field at which the R<sup>2</sup> values of each line intersect, as this is the point where the linear fit is optimized for each line.

If a knee point is found, the Fowler-Nordheim plot is split into two regions. Each region is fit independently of each other to find the  $\beta$ -factor and emission area Ae for each line segment, i.e., for the high and low field regions. Additionally, the knee point is applied to extract  $\beta$ -factor and Ae for both the I-E and Q-E dependences. A comparison between these two fitting methods can be seen using the postprocessing options along with image processing results. Both of these options are independent from the main data processing pipeline and can be done in tandem with the data processing.

If no knee point is found, the entire Fowler-Nordheim plot is fit by a single line. FEbeam displays figures in Fowler-Nordheim coordinates with the knee point indicated. Additional plot showing the R<sup>2</sup> value is generated if the knee point was determined. It should be noted that if the algorithm cannot find the knee point due to no diversions from the Fowler-Nordheim law, the user is able to select an option on the FN Options interface (seen in Figure 10a) to fit the Q-E data without a knee point. This interface also allows for the user to save the data and figures of the Fowler-Nordheim plot and the R<sup>2</sup> plot with the additional ability to change the axis range for better display (**Figure 3.2.9b** and **Figure 3.2.9c**). This can be changed for each conditioning field Eh chosen, and each data set needs to be saved independently by selecting the save button for each E<sub>h</sub>.

The data extracted from the QE curves is only one half of the equation when analyzing field emission dynamics. The other half of that equation determines the number of emitters based on the *in-situ* imaging system. This work collaborates the evidence that the Fowler Nordheim equations does not accurately predict the effective emission area. The emission area can be

calculated independently using the imaging system while providing a non-subjective counting scheme to determine the number of emitters. This is done using a machine learning algorithm in the form of FEpic.

# 3.3 FEpic

The development of FEpic [3] was a collaboration across our whole laboratory team and was headed by a fellow graduate student, Taha Posos, who the author would like to thank for allowing us to use some of the work here. FEpic was originally designed for image processing of field emission images on YAG screens for DC field emission test-stands. The work presented here is the is an expansion of the implementation of FEpic to operate in the RF environment and is heavily based on Ref. [x]. This was done to find the number of local maximums which can be used to find the cathode's emission area independently from the effective emission area calculated from Fowler Nordheim equations. The images are originally an intensity matrix created from a .dat file that is imported into FEmaster under the image processing section where the operator can select a maximum and minimum value for the intensities for the image for better

visualization. This does not change the actual pixel value, just the color bar on the axis, see **Figure 3.3.1**.

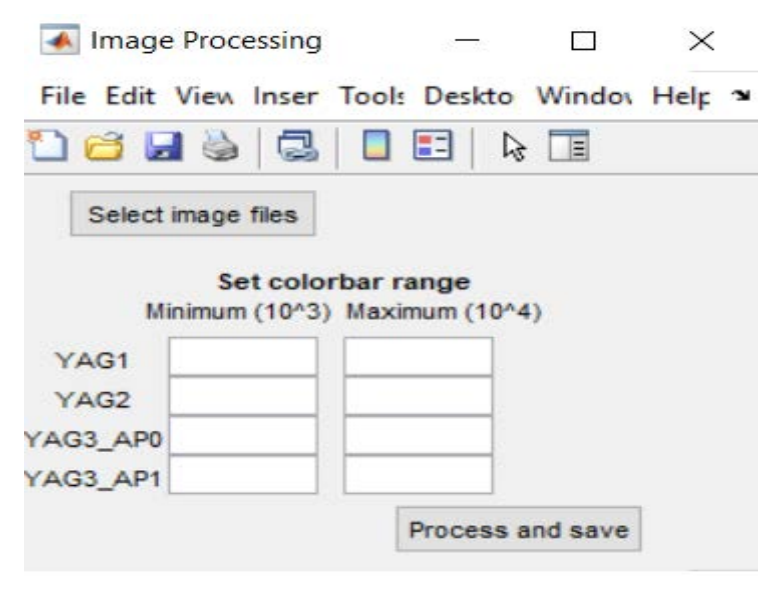


Figure. 3.3.1 FEpic inside of FEmaster options for selecting minimum and maximum threshold for image visualization. Options include all three YAG on the ACT and YAG3 having two options one with and without the aperture.

Next, loading in of a 450 x 450 pixel black and white image was done to determine the number of search regions of 10 pixels. All spot sizes were found to be within two standard deviations of the Gaussian peak which was determined to be 10 pixels with no local maximums less than 20 pixels apart. This search region is called a kennel.

To determine if a local maximum is present, we use the Euclidean distance formula **Eq. 3.3.1**.

$$d_a = \sqrt{(x_i - x_{MISR})^2 + (y_i - y_{MISR})^2}$$
 Equation 3.3.1

Around a given pixel a 10 x 10-pixel evaluation area was used to determine if there were any other pixels with a brighter intensity value. If the original pixel chosen is the brightest pixel in the search radius (MISR), it is determined to be one of the global maximums in the image. If

the chosen pixel is not the brightest pixel another 10-pixel kennel is used. The pixel in the previous kennel is called the maximum in search radius. Then another kennel is established around the maximum in search radius until it finds a global maximum. The pixels' location and value are recorded on the decision plot. The decision plot is so-called due to it determines which pixels are emitters. The intensity value for the images ranges from 0-2<sup>16</sup> due to using a 16-bit Blackfly camera at the ACT. To determine if the global maximum is an emitter, an assisted machine learning algorithm was used using a Gaussian decision boundary. This is due to two reasons: the first is that there may be a minute change in the intensity in the dark region which could be falsely categorized as the emitter. These are easily filtered out by being able to set a minimum threshold (C in Eq. 3.3.2) on the distribution function.

$$V_p(p_a) = A * Exp\left[\frac{-(p_a - \mu)^2}{2\sigma^2}\right] + C$$
 Equation 3.3.2

where  $p_a$  is the pixel position, Vp is the pixel value, A is the amplitude,  $\mu$  is the mean,  $\sigma$  is the standard deviation, and C is an offset.

The second is due to having dead pixels or close clustering in the image and these are much harder to sort out. Dead pixels can be caused by either defects in the camera or in the case of the RF image x-ray damage. X-ray damage was particularly difficult to deal with due to that when a pixel in the camera is damaged by a high-power x-ray generated by the accelerator that that pixel shows up in the image as a maximum pixel value (2<sup>16</sup>). To cancel out this x-ray damage a custom smoothing algorithm was used. For each pixel selected the next 3 x 3 area to find the median value and that mediam value was replaced the previous value. This is done as the x-ray damage normally only damages one pixel and therefore it is an outlier with regards to its neighbors. Replacing it with the median value, conserves the background value and eliminates skews to the total count due to x-ray damage.

Close clustering of emitters is much harder to deal with as the field emitter in the RF environment often causes a localized emitter which may have tens to hundreds of emitters and very close density which may show up as a single blob on the image as in **Figure 3.3.2**.

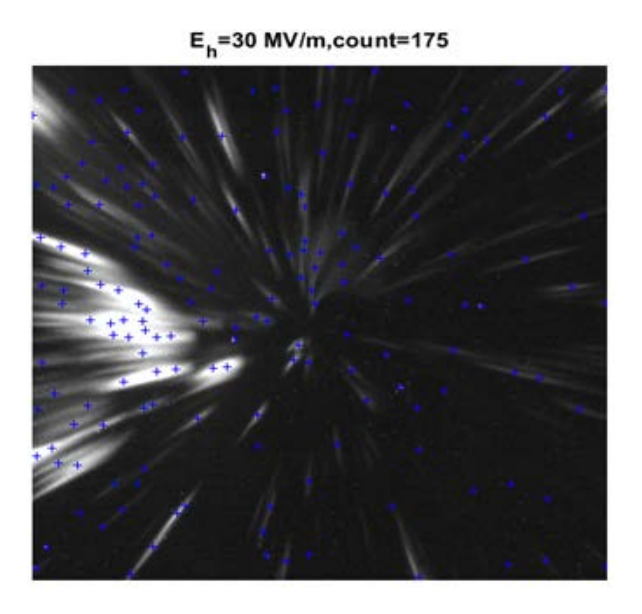


Figure. 3.3.2 Illustration of closely packed emitters extracted from data for A-class UNCD FECs form the experiment outlined in CH4.

On the other hand, some emitters may not be as strong and would be very faint line which is also hard to determine. This causes great clustering of emitters with very close intensity values to form in the decision plot (see the red circled region in **Figure 3.3.3a**). This clustering of emitters in the decision plot is very hard for the machine learning algorithm and even operators to determine due to the lack of a clear delineation between actual emitters and background noise. The goal would be to account for all of the strong emitters in an image however small changes in the shape of the Gaussian distribution can cause a grave over estimation in the number of emitters or not being able to resolve clearly visible strong emitters. To modify this algorithm to work in RF, the circular kennel used in the DC images was changed to elliptical in RF. This is because in the DC environment the emitters are made at a single point which then can be linearly

transposed onto the imaging screen. In the presence of RF, the 360° emission phase turns the single emitter point into a line due to the large energy spread of the field emitter which can be as great as 20%. This is different from the DC test stand where the YAG is immediately followed by the anode and, therefore, the electrons are collected on the YAG. In the RF environment, the electrons are not embedded into the YAG but instead transverse through it and therefore the images are actually a projection image. This projection image causes all of the emitters to be rotated at some form of an angle as they transverse through the YAG. The electrons of the large energy spread will also have a larger divergence angle as the diversion single  $\theta = \tan^{-1} \Delta \delta$  where  $\Delta \delta$  is the energy spread. This results in the electrons that are on axis, and would have the lowest energy spread, being recorded on the images as almost perfectly circular while the electrons towards the edge which are created off axis have the largest energy spread and appear as the largest lines (see Figure 3.3.3b).

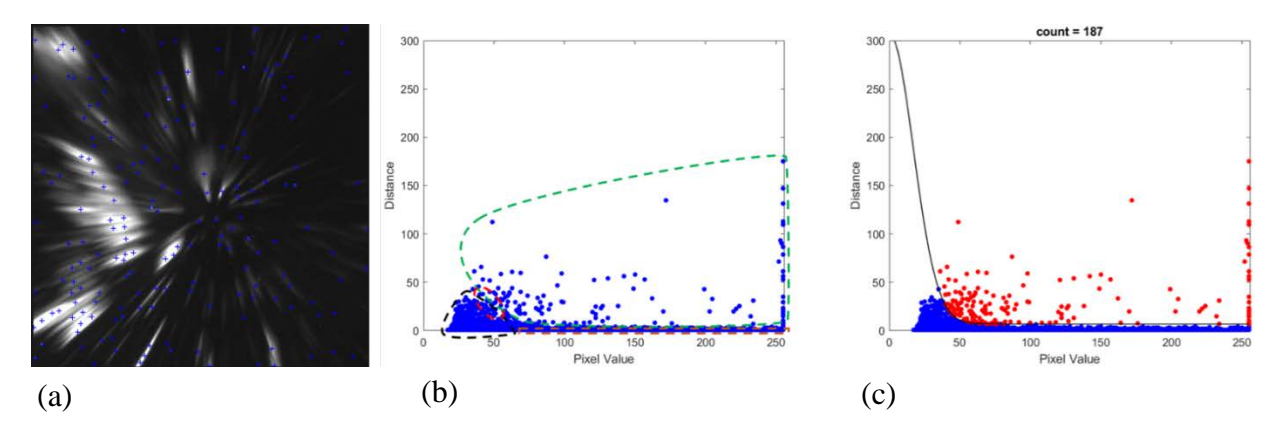


Figure. 3.3.3 (a) example of image processing results. (b) decision plot green line shows actual emitters, black line shows the noise, and red line shows the undefined region that is a mixture of noise emitters and actual emitters. (c) machine learning algorithms final decision for decision boundary Gaussian fitting function.

Each of these dashed lines represent a single emitter in the image. This is an ongoing issue as it is nearly impossible for the algorithm to determine the dimensions of the ellipse.

Without direct intervention from the operator, one cannot determine the ratio between the vertex

and the covert texts of the ellipse. This would have to be done for every emitter and therefore would negate the effect of using this algorithm as one would have to assume the number of emitters before calculating it. To account for this, it was determined that an uncertainty of +/-10 emitter should be used.

To determine the emission area, the authors assumed that each emitter comes from the grain boundaries which is a unit area of 10 nm². Therefore, the total emission area recorded on the images is the number of emitters time the unit area. Then, as discussed in CH2, as all of these images shown were from YAG3 with a 1 mm aperture added at the location of YAG2, the number of emitters shown are <10 % of the total emission. Therefore, the total emission area is approximately an order of magnitude greater than the number of emitters calculated through the image processing algorithm. Beam dynamics simulations using a combination of FEgen and GPT prove that each line emitter present on these images corresponds to a single emitter which is explored in detail in CH 4.1.

It should be noted that even though there are significant concerns for the image processing algorithm in an RF environment, it has been shown in papers by our colleagues to be extremely accurate in the DC environment. Due to the dynamic shape of the lines and the severe damage to the camera due to x-ray damage, significant work was done to modify this algorithm to become the current version of FEpic. It should also be noted that the machine learning algorithm only has a select number of images from the RF environment to use as a baseline. Future experiments would be helpful to give this algorithm more of a knowledge base.

#### 3.4 FEbreak

Rounding out the FEmaster series is FEbreak, which is the main data acquisition workhorse of the series. FEbreak was designed to automate the conditioning such that after the

user identifies and determines the initial breakdown threshold, the conditioning process and controlling of the klystron, signal generator tuning, and data acquisition requires no user interaction. When commissioning high gradient structures, the conditioning process can be extremely long and tedious and may take several hours. It must be run in a 24-hour operation which is not feasible to do in a small team configuration.

This software is also extremely versatile being built in LabVIEW using a real-time analysis method not available at other facilities using an FPGA scope. This real-time analysis can determine the breakdown rate with extreme accuracy. Using parallel computing, the data acquired can be directly postprocessed through FEbeam and FEpic for a real-time analysis structure performance.

This is part of ongoing research to develop a high gradient test stand called the C-band engineering research facility New Mexico (CERF-NM) at Los Alamos National laboratory (LANL). Our team developed the software called FEbreak (a part of the FEmaster series) which allows analyse of breakdown in real time. This software will be able to provide high accuracy breakdown analysis while coupling it to the field emission dark current effects and breakdown *in situ* imaging software diagnostics. FEbreak has shown a 97% efficiency for pulse acquisition and analysis when processing1 µs long pulses at 100 Hz repetition rate, which is a standard setting for testing many normal conducting cavities for high gradient.

#### 3.4.1 Introduction

The ability to measure the breakdown rate is the cornerstone of high gradient research.

Breakdown rate characterizes the ability of the structures to handle high electromagnetic power under long-term operation [30]. Therefore, the ability to measure the breakdown rate accurately and consistently is paramount. If a breakdown analysis software is not a real-time measurement,

it will not be able to recognize and analyze every pulse and therefore will not accurately compute the breakdown rate [31, 32]. This will result in an artificially low breakdown rate. Furthermore, if these measurements are not done in real-time, timely control of the klystron is impossible.

The work presented here is a new attempt to fill the existing gap in diagnostics. To this end, a real time breakdown analysis software called FEbreak was developed. It enables active klystron tuning, while also providing a parallel computing option for data processing to analyze the field emission characteristics and then directly tie them to a future *in situ* imaging system to be able to determine the locations of breakdowns within the structure during the commissioning process.

#### 3.4.2 CERF-NM facility

The CERF-NM facility is a C-band (5.712 GHz) high gradient test facility. It is based around a 50 MW Canon klystron that can produce peak powers up to 50 MW and couple the power into the structures under test (see **Figure 3.4.1a**).

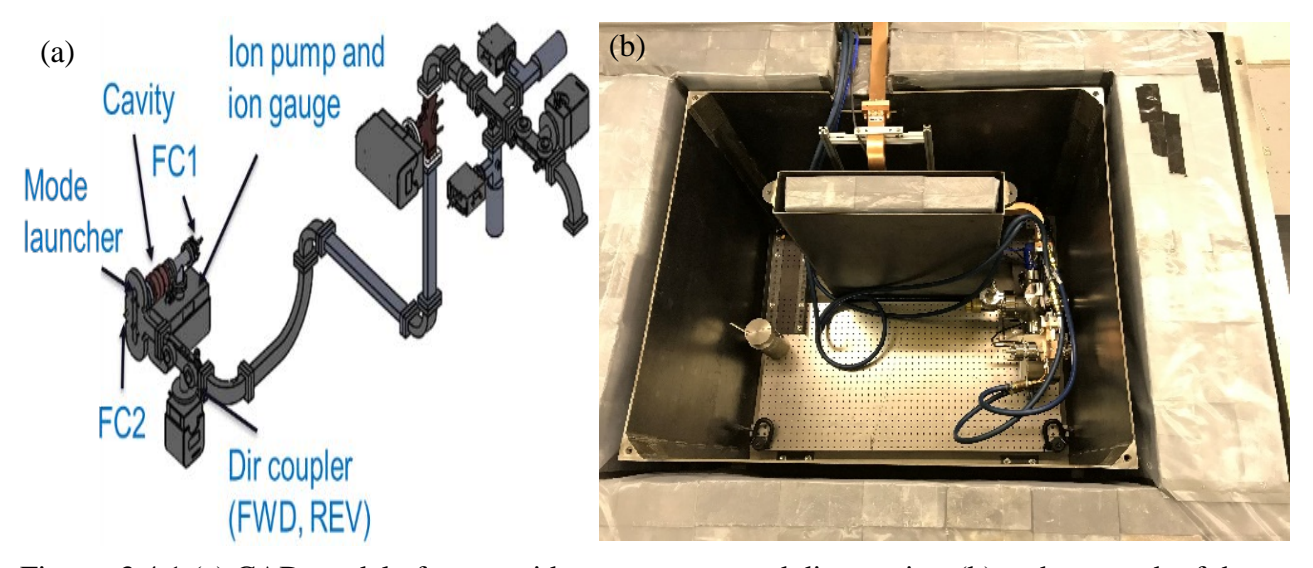


Figure. 3.4.1 (a) CAD model of waveguide components and diagnostics, (b) a photograph of the current state of the part of the CERF-NM facility in lead box enclosure. All JACOW conference proceedings are published under the Creative Commons Attribution 3.0 license (CC-BY 3.0) to copy and redistribute the material in any medium or format.

The accelerating structures under test produce dark current that can be accelerated up to beam energies of 5 MeV in a three-cell design. (See other papers in this proceedings collection for more details on CERF-NM.)

The waveguide line of the CERF-NM has seven vacuum pumps which can maintain vacuum at  $10^{-10}$  Torr. A series of temperature controls are implemented using thermocouples on key components including both bidirectional couplers inside and outside of the lead box enclosure (see **Figure 3.41b**) and the RF window which is temperature control by using a chiller. The two Faraday cup allow for the dark current measurements. When combined with the forward or reflected power measurements that come from the bidirectional coupler, it allows us to determine the Fowler-Nordheim parameters for the field enhancement in the cavity. All of these diagnostics are used to analyze breakdown in real-time. The commissioning procedure of a cavity can be completely automated.

#### 3.4.3 FPGA scope for real-time breakdown analysis

Our controls system is based on the National Instruments PXI Express system. This system consists of a crate which allows multiple modules to be inserted into the system in order to customize the configuration and capabilities of the entire system. Currently our configuration consists of the main PXIe chassis, a PXIE-8840 controller with Windows installed onto it, a PXIE-6341 DAQ card, a PXIE-5654 RF signal generator, and a PXIE-5172 Oscilloscope with built in FPGA (see Figure 3.4.2). This system can be broken down into two main sections, the controller, and the FPGA. Currently the majority of the decision-making processes are done

within the controller section, however it is planned to off-load significant portions of the decision making onto the FPGA in the near future.

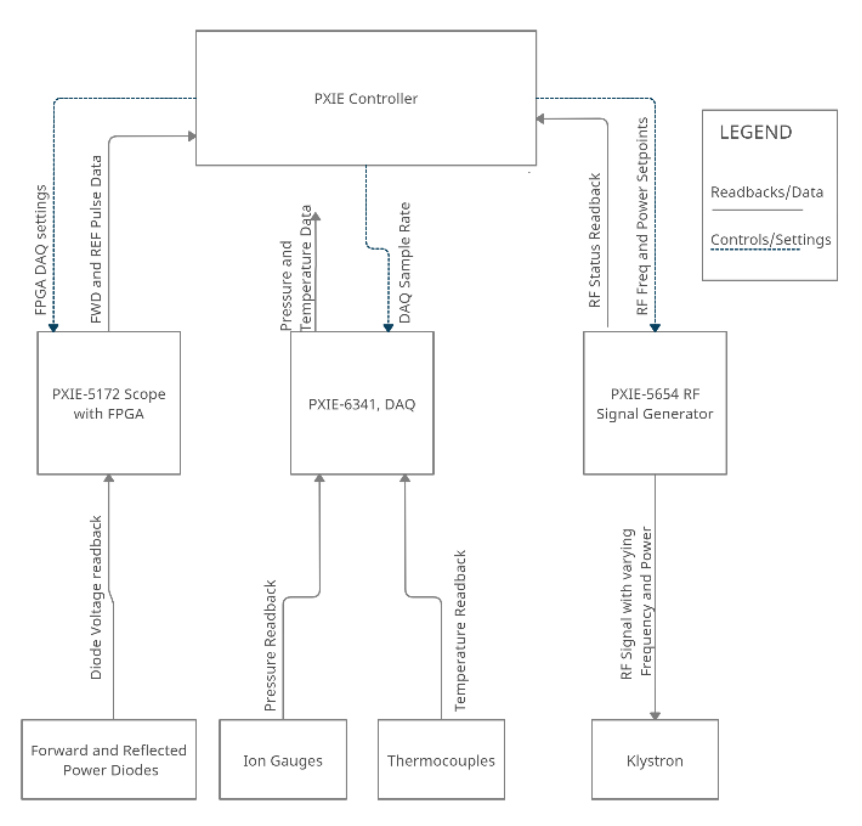


Figure. 3.4.2 Block diagram of FEbreak. All JACOW conference proceedings are published under the Creative Commons Attribution 3.0 license (CC-BY 3.0) to copy and redistribute the material in any medium or format.

Within the controller section of our DAQ system, we perform several operations. First, we initialize the crate modules. The controller first initializes our RF signal generator with a set power and frequency and waits for the module to confirm that it is sending out the appropriate signal. During this time, the controller also initializes the DAQ module to begin recording vacuum and temperature data. Once the RF signal is being generated and the pressure and temperature readings start being recorded, the rest of intricate parts of FEbreak is initialized.

The FPGA module runs mostly independently from the crate controller. It begins by waiting for a initialize command from the controller, and once it receives this initialization

command it grabs configuration information from the current experimental settings. This information includes the number of channels to read, the trigger settings in order to synchronize it with RF generation, how many datapoints to record, and at what sample rate it should record them. The FPGA itself then proceeds to run in its own loop, constantly triggering, recording data, and then sending that data to a pool of shared memory between itself and the controller. Currently the FPGA does not make any decisions on its own with this data, but future plans will offload some of the computational logic with the recorded data from the controller to the FPGA.

Once the controller has received the data from the FPGA, it performs a series of operations. First, it displays the data in real time, which allows an operator to select what parts of the reflected power they are interested in analyzing (see Figure 3.4.3).

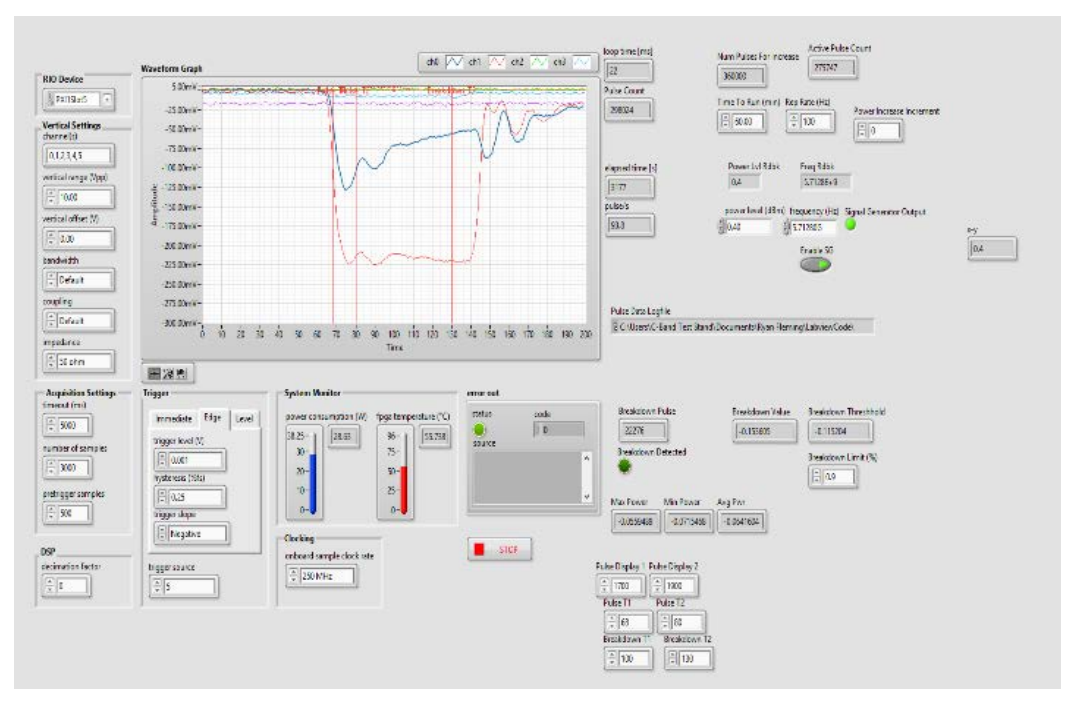


Figure. 3.4.3 User interface for FEbreak. All JACOW conference proceedings are published under the Creative Commons Attribution 3.0 license (CC-BY 3.0) to copy and redistribute the material in any medium or format.

Once this selection is completed, the controller will automatically determine the breakdown threshold and analyze each pulse to determine if a breakdown has occurred. If the

breakdown rate is acceptable the controller will increase the RF power by a set amount after the required number of pulses have been sent down the waveguide. However, if the breakdown rate is too high, then the controller will decrease the RF power to reduce the breakdown rate, before resetting its pulse count and continuing with the conditioning process. This data is saved in real-time after each pulse in order to prevent any data loss. This process repeats itself until stopped by an operator, or it reaches the end power goal of conditioning with an acceptable breakdown rate.

The increase in the reflected power that would normally be observed happens later in the pulse and therefore is inconsistent and leads to false positives or missing break down pulses that may be able to detect due to their variation. Future generations will hope to analyze both the Faraday cup and the reflected power for higher accuracy in the breakdown determination.

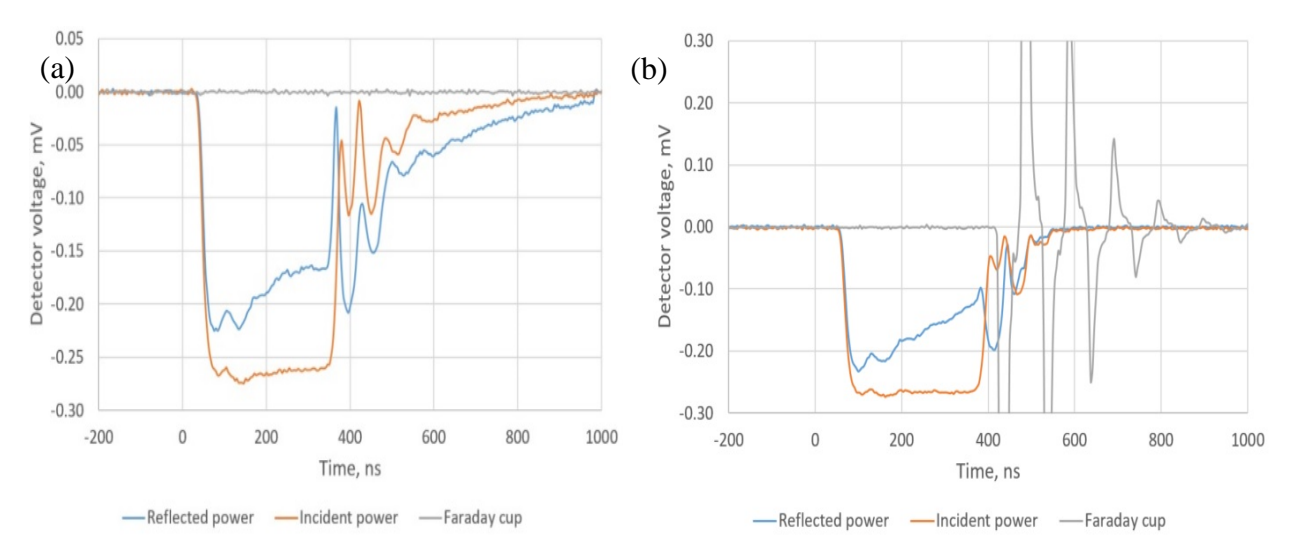


Figure. 3.4.4 Nominal (a) and breakdown condition (b) pulses showing the forward, reflected, and Faraday cup signals. All JACOW conference proceedings are published under the Creative Commons Attribution 3.0 license (CC-BY 3.0) to copy and redistribute the material in any medium or format.

The first single-cell cavity at CEFR-NM was tested up to 500 kW of input power into the cavity with no breakdowns detected. Hence, the dummy/test signals were used to evaluate algorithm functioning. Conditioning of the same cavity is underway up to 4 MW which will correspond to 161 MV/m accelerating gradient. It should be noted that there is a 0.465 time delay

between the RF power measurements in the Faraday cup due to the particle generation and the particles reaching the Faraday cup which was determined using our simulation results.

Future work includes integration of FEbreak into the FEmaster series along with analyzing the breakdown rate. It is paramount to not forget that breakdowns are dark current/field emission effects. Therefore, for a comprehensive analysis, the field emission characteristics must be considered when analyzing the performance of these high gradient structures. The data extracted from FEbreak will record the forward and reflected power as well as the Faraday cup measurements throughout the conditioning process. This data then would be directly imported into the FEbeam [4] software to parametrize data in the framework of time-dependent Fowler-Nordheim equation.

Additional hardware upgrades are underway to build an *in-situ* imaging system. Such upgrades will allow for imaging breakdown events/locations. Further coupling of field emission parameters to the modelling software FEgen [5] and image processing software FEpic [6] would allow to backtrack the geometry and location of a breakdown inside of the cavity, which can further be confirmed with autopsy/post-mortem analysis. It is this combination that will allow for high resolution cavity design (see **Figure 3.4.5**). Work is currently underway to allow for

parallel computing on a separate CPU system independent of the PXIE crate to do data processing and data acquisition in parallel.

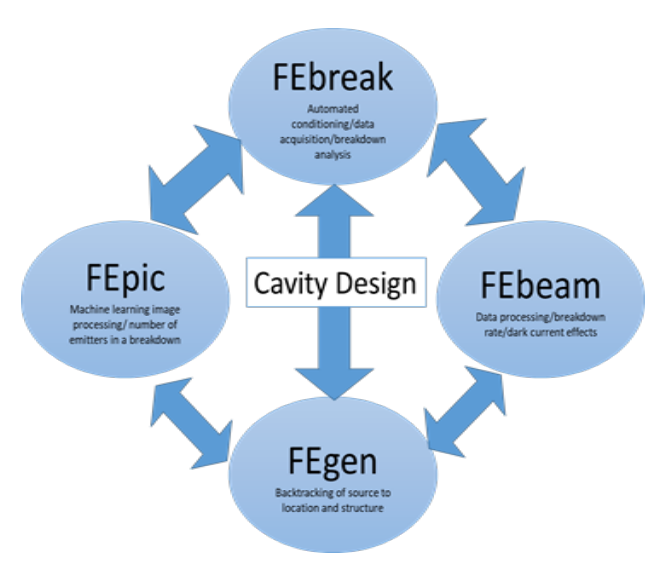


Figure. 3.4.5 Block diagram of the fully integrated FEmaster. All JACOW conference proceedings are published under the Creative Commons Attribution 3.0 license (CC-BY 3.0) to copy and redistribute the material in any medium or format.

This upgrade will be done in coordination with current upgrades to the PXIE configuration. The first of which is to include the internal triggering instead of external triggering by an external circuit which is currently being built. Second, work has shown in the past that having a phase in amplitude modulated forward pulse is better for conditioning as it will rapidly fill the cavity but then reduce the gradient for the rest the pulse. A second function generator can be used to produce this pulse and it will be done in real time using the FPGA code in future. Third, the current breakdown software is being programed in the LabVIEW platform and therefore is subject to slowdowns from running other codes in parallel such as the pressure and temperature monitoring code. Therefore, ongoing work is to completely include the breakdown logic into the FPGA functionality. It is the author's opinion that including this functionality completely inside of the PXIE crate will improve efficiency to above 99%.

It is the combination of the high-resolution results and conditioning procedure that we derived at the ACT and FEmaster series which can give the capabilities to determine the underlying mechanisms of field emission cathodes. Using the new fabrication methods for UNCD derived in CH 1, CH4 presents a study that shows a deviation from classical Fowler Nordheim with a space charge dominated Fowler Nordheim regime which is not limited by the Child Langmuir limit. Surpassing of the Child Langmuir limit will open the door for bright beam field emission capabilities for high gradient high-frequency injectors. A diamond field emission array (DFEA) made out of micro diamond was used to determine the contribution of the geometry and the material for pattern beam production. This shows conclusively that, unlike in the DC case, the geometry is negligible to the cathode performance in the RF case.

**REFERENCES** 

#### REFERENCES

- [1] M. Schneider, E. Jevarjian, J. Shao and S. V. Barnyashev Review of Scientific Instruments **92**, 053305 (2021)
- [2] E. Jevarjian, M. Schneider, and S. V. Baryshev, "FEgen (v.1): Field emission distribution generator freeware based on Fowler-Nordheim equation," arXiv:2009.13046 [physics.acc-ph] (2020)
- [3] T. Y. Posos, O. Chubenko, and S. V. Baryshev, "Fast pattern recognition for electron emission micrograph analysis," arXiv:2012.03578 [physics.app-ph] (2020)
- [4] M. Schneider, R. Fleming, E. I. Simakov, D. Gorelov, *et. al*, Proceedings from 12th International Particle Accelerator Conference (IPAC2021), Campinas, SP, Brazil (2021)
- [5] D. R. Whaley, R. Duggal, C. M. Armstrong, et. al, IEEE Transactions on Electron Devices **56**, 896 (2009).
- [6] J. Qiu, S. S. Baturin, K. K. Kovi, O. Chubenko, *et. al*, IEEE Transactions on Electron Devices **65**, 1132 (2018).
- [7] J. Shao, M. Schneider, G. Chen, T. Nikhar, *et. al*, Phys. Rev. Accel. Beams **22**, 123402 (2019).
- [8] S. M. Lewis, V. A. Dolgashev, A. A. Haase, E. A. Nanni, *et. al*, Proc. Int. Particle Accel. Conf., TUPTS077 (2019).
- [9] J. Lewellen and J. Noonan, Physical Review Special Topics-Accelerators and Beams **8**, 033502 (2005).
- [10] K. Flottmann, ASTRA-A space charge tracking algorithm, DESY.
- [11] https://amac.lbl.gov/jiqiang/IMPACT-T/.
- [12] http://www.pulsar.nl/gpt/.
- [13] https://www.txcorp.com/vsim.
- [14] J. Petillo, K. Eppley, D. Panagos, P. Blanchard, *et. al*, IEEE Transactions on Plasma Science **30**, 1238 (2002).
- [15] K. E. Nichols, H. L. Andrews, D. Kim, E. I. Simakov, *et. al*, Applied Physics Letters **116**, 023502 (2020).
- [16] J. Wang and G. Loew, Tech. Rep. (Stanford Linear Accelerator Center, 1997).
- [17] J. W. Gadzuk and E. W. Plummer, Rev. Mod. Phys. **45**, 487(1973).

- [18] D. Shiffler, S. Fairchild, W. Tang, B. Maruyama, *et. al*, IEEE Transactions on Plasma Science **40**, 18712012).
- [19] S. V. Baryshev, S. Antipov, J. Shao, C. Jing, *et. al*, Applied Physics Letters **105**, 203505 (2014).
- [20] T. Y. Posos, S. B. Fairchild, J. Park, and S. V. Baryshev, Journal of Vacuum Science & Technology B **38**, 024006 (2020).
- [21] X. Li, M. Li, L. Dan, Y. Liu, and C. Tang, Phys. Rev. ST Accel. Beams **16**, 123401 (2013).
- [22] P. Piot, C. A. Brau, B. K. Choi, B. Blomberg, *et. al*, Applied Physics Letters **104**, 263504 (2014).
- [23] D. Mihalcea, L. Faillace, J. Hartzell, H. Panuganti *et. al*, Applied Physics Letters **107**, 033502 (2015).
- [24] Q. Wang, X. Li, Y. Di, C. Yu, et. al, Journal of Applied Physics **119**, 084504 (2016).
- [25] O. Chubenko, S. S. Baturin, and S. V. Baryshev, Journal of Applied Physics **125**, 205303 (2019).
- [26] O. Chubenko, S. S. Baturin, K. K. Kovi, A. V. Sumant, and S. V. Baryshev, ACS Applied materials & Interfaces 9, 33229(2017).
- [27] A. Grudiev, S. Calatroni, and W. Wuensch, Phys. Rev. Spec. Top.-Accel. Beams 12, 102001 (2009).
- [28] J. P. Barbour, W. W. Dolan, J. K. Trolan, E. E. Martin, and W.P. Dyke, Phys. Rev. **92**, 45(1953).
- [29] R. G. Forbes and J. H. B. Deane, Proc. R. Soc. A **463**, 2907 (2007).
- [30] E. I., Simakov, V. A Dolgashev, S. G. Tantawi. Nuclear Instruments and Methods in Physics Research Section A: Accelerators, Spectrometers, Detectors and Associated Equipment, **907**, 221 (2018).
- [31] Dolgashev, V. A. Progress on high-gradient structures. In AIP Conference Proceedings American Institute of Physics **1507**, 76 (2012)
- [32] A. Palaia, V. Dolgashev, J. Lewandowski, S. Weathersby, Proceedings from In DIPAC2011, 10th European Workshop on Beam Diagnostics and Instrumentation for Particle Accelerators. Hamburg, Germany. (2011)

#### CHAPTER 4 TECHNICAL RELEVANCE

The following chapter addresses and debunks the major assumption that field emission cathodes behave under classical Fowler Nordheim conditions over the entire field and charge regime. As Chapter 1 explained, recent developments in DC have shown that there is a limitation due to the ballast resistance of the material. In addition, there are other conditions that are not considered, such as the effects of high spatial temporal space charge. Furthermore, studies do not back out the effects of the materials and geometric effects on FEC performance using nonplanar geometries. This chapter addresses these issues and derives a new regime of field emission unambiguously showcasing the 2D space charge emission regime observed in experiment directly. This work demonstrated record-breaking results, producing the world's highest charge of 300 nC/pulse, the world's highest field achieved by a nonmetallic cathode at 96 MV/m, and surpassing the Child Langmuir limit for the first time. In addition, this (N)UNCD FEC has beam brightness of 10<sup>14</sup> A/(m\*rad)<sup>2</sup>. Moreover, a second set of cathodes in a patterned array design showed the ability to produce pattern beams, while pinpointing the material ballast resistance limited emission of the FEC. Ultimately, this work was able to derive a concept landscape map of what cathode physics are dominant in which regimes.

## CHAPTER 4 PRODUCTION OF AMPERE-CLASS UNCD AND EVIDENCE FOR NEW EMISSION PHYSICS

#### 4.1 Ampere-Class beam and non-Fowler Nordheim conditions

This experiment used the ACT experimental facility and was optimized using the procedure derived in CH2.

#### 4.1.1 Section 4.1.1: Cathode Fabrication

The growth for this particular cathode was based on the growth procedure and knowledge of our laboratory colleague Tanvi Nikhar whose work is summarized in section 1.2 of this dissertation. For this experiment, the UNCD cathode was grown on an ultrasonically seeded molybdenum puck using microwave plasma assisted chemical vapor deposition in a S-band reactor operated at 2.45 GHz [1,2]. A synthesis substrate temperature of 1248 K was achieved using an H2/(20%)N2/(5%)CH4 feed gas mixture maintained at a flow rate of 200 standard cubic centimeters per min (sccm) at a total gas pressure of 67.5 torr and 3 kW microwave power. The substrate temperature was measured using an infrared pyrometer during the 1-hour growth process. The UNCD coated puck was then mechanically attached to the three-part assembly, as outlined in Ref.[3]. Additionally, the edge of the cathode was carefully rounded and UNCD coated on the inner 18 mm of the 20 mm diameter puck to avoid edge effects.

The grown sample was then characterized using a Horiba Raman spectrometer with a 532 nm probing laser. The Raman spectrum was typical to UNCD films illustrating D and G peaks centered around 1333 cm-1 and 1560 cm-1, respectively, were observed (**Figure 4.1.1**). This confirmed that the D peak corresponded to high fraction of sp3 diamond phase and G peak corresponded to semi-amorphous sp2 graphitic phases [1]. The deposition temperature was balanced such that the film exhibited high conductivity while still maintaining the sp3 phase (shown by the presence of 1333 cm-1 peak). From experiments on insulating Si and quartz

witness substrates such a Raman corresponds to a resistivity of  $0.5~\Omega\times\text{cm}$ : high conductivity is likely due to improved crystallinity and physical connectivity between sp2 grain boundaries as manifested by the G peak which is positioned at 1560 cm-1 [1]. Scanning electron microscopy further confirms nanostructure typical for UNCD.

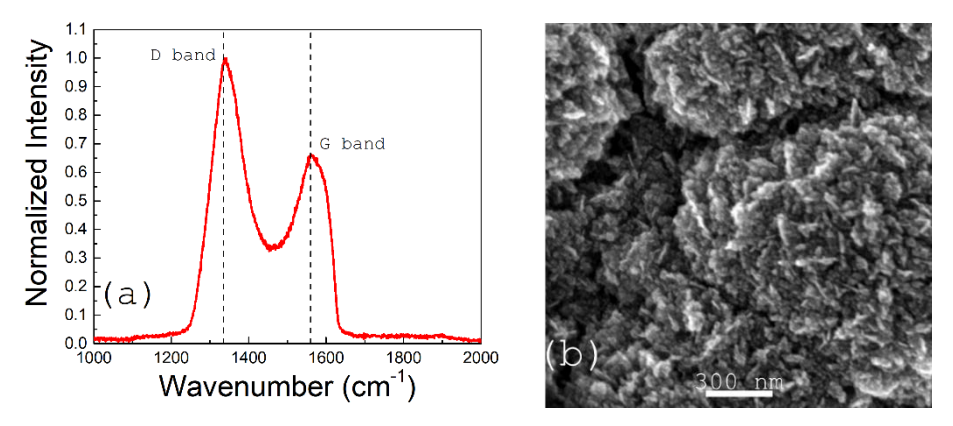


Figure. 4.1.1 Raman spectrum and SEM micrograph of as-grown sample [33]. It is not necessary to obtain permission to reuse this article or its components as it is available under the terms of the <u>Creative Commons Attribution 4.0 International</u> license.

#### 4.1.2 Image Processing and Beam Dynamics

Imaging was supported by beam dynamics simulations in GPT that were used to track an initial particle distribution generated with an open-source software called FEgen [4]. The initial energy spread on the cathode surface was set to the intrinsic value of 0.1 eV, and the UNCD work function was assumed to be 4 eV from previous Kelvin probe measurements [5]. and launched and captured at a time stamp corresponding to the YAG3 position. **Figure 4.1.2(a, b)** is a side-by-side comparison between the simulated and experimental emission imaging results at YAG3 which demonstrate a high degree of resemblance. From comparing simulations and imaging, emitters appear as bright stretched ellipses, but not circular spots like in a dc case [6,7]. The emission spots are stretched along rays, which start at the center of a cathode and go in all directions. They vary in length and brightness and are non-uniformly distributed in polar

coordinates. Unlike in dc, electrons are generated by and interact with the rf/microwave drive cycle in a wide phase window. The extended interaction phase window causes the ellipses (or streaks) to form, are essentially represented as rotated projections of longitudinally stretched electron beamlets arriving from the cathode surface. At this distance from the gun, the spatio-temporal behavior of the beam is dominated rf emittance  $\varepsilon_{rf}$ . It can be concluded that each line represents a singular emitter, and that counting streaks should be representative of the number of emitters and their variation as a function of the external power in the rf injector.

Charge collection was done hand in hand with image collection at different gradients.

The collected images were processed using FEpic to obtain the emitter population statistics throughout the FEC conditioning process. In brief, FEpic partitions the image into equal sections and finds brightest pixels in each of those sections. Then, it utilizes a so-called decision plot that relates the intensity of a brightest pixel and the distance between this brightest pixel and its closest neighbor. It then applies a special filter to sort emission centers from glowing background

or dead pixels. **Figure 4.1.2b** shows an exemplary calculation of the number of emitters using Figure **4.1.2a** as an input. The full set of image processing results can be found in Appendix A.

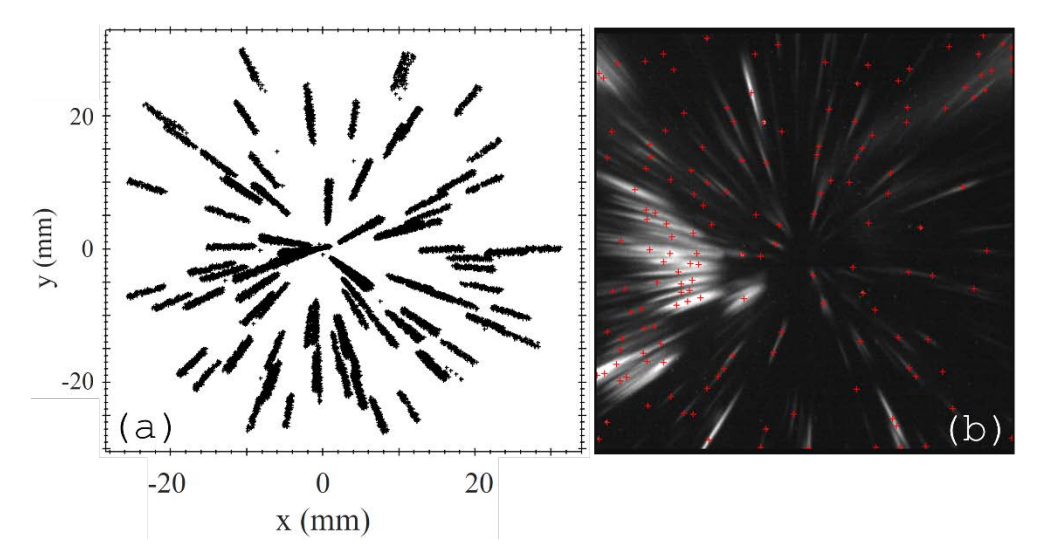


Figure. 4.1.2 Comparison of transverse electron patterns (a) as simulated in GPT and (b) as obtained experimentally, both at YAG3 position. The input emitter distribution was generated and imported using a pattern captured in dc, see Figure. 1 in Ref. [6]. Image (b) was processed with FEpic, and counted emitters are labeled by red marks. All other images with local maxima identified and labeled as emitters can be found in <u>Appendix A</u> [33]. It is not necessary to obtain permission to reuse this article or its components as it is available under the terms of the <u>Creative Commons Attribution 4.0 International</u> license.

Based on the high power conditioning methodology developed previously [3], the UNCD FEC was continuously conditioned from a turn-on field, determined to be 9 MV/m all the way up to 100 MV/m in increments of 5 MV/m. 9 MV/m was pinpointed to be the turn-on field as the electron emission signal was first detected on YAG1 at this field, though the charge on the Faraday cup was below the detection limit.

Q-E curves were taken as follows. The gradient was pushed up to the maximal intermediate target value termed Eh. Each conditioning field was taken in 5 MV/m increments, and the gradient was increased until each conditioning field, Eh, was achieved. The system was then kept at a given Eh until the breakdown rate reduced to ~10-4 per pulse. Every Q-E curve was then taken downwards with increments of 0.5 MV/m down to the point where no charge is detected

by the Faraday cup. For every consecutive Q-E curve Eh was 5 MV/m higher than Eh for preceding Q-E curve.

The first experimental session could not go above 70 MV/m as a breakdown event with a breakdown rate spiked instantaneously exceeding 10-1 per pulse. It occurred when the cathode was attempted to be run at 75 MV/m for data taking. Therefore, the first session was concluded, and a second session had to be carried out after the breakdown issue was identified. Upon stopping the experiment, the as-installed cathode was optically viewed inside the gun which allowed to identify the source of the intense breakdown sequence as a single location on the uncoated rounded molybdenum puck edge. The inset in **Figure 4.1.3** shows the outer edge as a light blue circle, and the breakdown location can be seen as a light blue thick dot located at 1 o'clock.

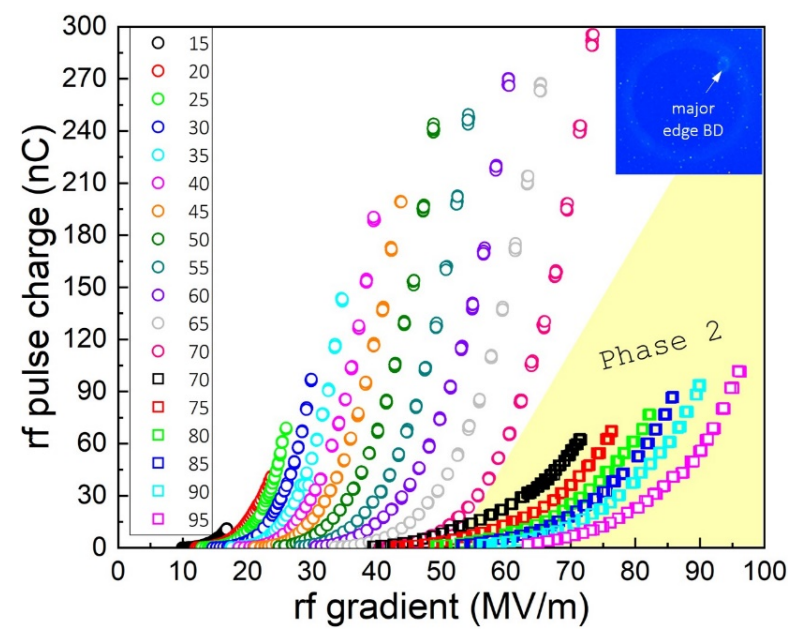


Figure. 4.1.3 The Q-E curves for phase one and phase two separated into two regions corresponding to the experiment runs. In the legend, the numerical values label the maximal conditioning gradient achieved per Q-E curve (referred to as  $E_h$ ). The inset shows *in situ* taken image of the major breakdown event, located on the outer edge of the cathode puck at 1 o'clock (labeled with an arrow) that stopped the phase one session [33]. It is not necessary to obtain permission to reuse this article or its components as it is available under the terms of the Creative Commons Attribution 4.0 International license.

The entire UNCD surface was determined to be unharmed by this major breakdown event. The FEC edge was refinished, and the FEC was reinserted into the gun for the second experimental session, demonstrating an additional depth of the UNCD FEC endurance capabilities.

During the second phase, the cathode was conditioned back up to 70 MV/m in a matter of two hours with only three breakdowns occurring during the entire process. Q-E curves were taken then from 70 MV/m to 95 MV/m in the same manner as was done in the first phase. 96±4 MV/m was the maximum field achievable due to power limited output of the klystron. While 95 MV/m was a targeted Eh, the actual mean gradient calculated from the measured input power was 96 MV/m with an error bar of 4 MV/m because the actual rf pulse envelope from the klystron was not an ideal rectangle. **Figure 4.1.3** highlights that, despite the reinstallation process that involved micromachining and air exposure, the output charge remained at the same order of magnitude of 100 nC. Additionally, phase two experiments showed the steady increase of the output charge with increasing gradient. This is a record-breaking result for an rf injector where a field emission cathode produced 0.1 A of current at 100 MV/m. Figure 4.1.4 compares emission patterns captured at 70 MV/m before and after the Phase 1 experiments stopped and restarted in Phase 2. One can see that the reduced output charge is a consequence of the reduced emission area. The exact reason behind the drop in charge (and apparent emission area) remains unknown and requires designed experiments where the conditioning process must be interrupted and the cathode re-installed and re-conditioned again such that Q-E curves and images are continuously. Furthermore, it is clear from **Figure 4.1.4** that the family of the emitters that dominated the emission in Phase 1 are the same emitters producing charge in Phase 2. It should be noted that, in the ACT gun, there is no locking mechanism when installing a cathode. During

re-installation, the cathode was unintentionally rotated by 50 degrees, as was determined from matching the major emission cluster on the right side of the images taken at 70 MV/m.

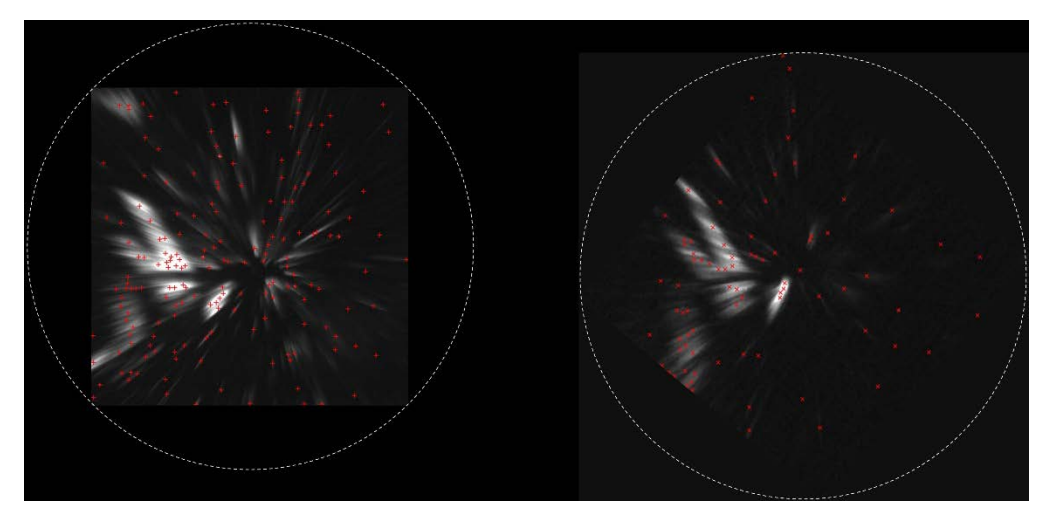


Figure. 4.1.4 Comparison between emission patterns on YAG3 at 70 MV/m taken in Phase 1 (left) and Phase 2 (right, rotated CCW by 50 degrees). The images are placed with respect to the origin: since there is slight *y*-offset in the left image the right rotated image rests below against the right image [33]. It is not necessary to obtain permission to reuse this article or its components as it is available under the terms of the <u>Creative Commons Attribution 4.0</u> International license.

Raw data analysis and conversion to Q-E curves, as well as plotting and analysis in various coordinates, was accomplished using a data processing pipeline called FEbeam which is described in a great detail in Ref.[8]. FEbeam begins by taking the raw voltage signal waveforms for the diodes measuring forward power and reverse power and Faraday cup to calculate the Q-E curves which are then translated into Fowler-Nordheim coordinates by analyzing the rf drive signal envelope and finding its temporal structure. The rf pulse length was 6  $\mu$ s throughout the presented experiments. This resulted in a constant scaling factor when plotting either Q-E or I-E curves where I is the rf pulse current. As before, Fowler-Nordheim coordinates for rf case are  $log_{10}\left(\frac{\bar{I}}{E^{2.5}}\right)$  versus  $\left(\frac{1}{E}\right)$  [5] per modified time averaged FN relation that reads

$$I = 1.54 * 10^{-6} \left(\frac{A_e}{\phi}\right) (\beta * E_h)^2 Exp\left(\frac{-6.83*10^9 \phi^{\frac{3}{2}}}{\beta * E_h}\right) \text{ Equation 4.1.1}$$

Unlike in previous rf cases [3,9], a significant divergence from classical Fowler-Nordheim (FN) law was revealed, which is obviously the result of the exceptionally high charge despite the duty cycle being extremely low, namely  $6\times10^{-6}$  at 1 Hz. The divergence is manifested by the presence of the knee point (previously discussed for dc case elsewhere [7]): two linear fits of a different slope exist intersecting at the knee point. Due to the large gradient incremental step (and thus, a smaller number of data points) a new automated algorithm to retrieve the knee point was implemented in <u>FEbeam</u>. The algorithm determines the knee point location along with the relative ranges of the  $R^2$  values of the iterative fitting for the line segments as depicted in **Figure 4.1.5**. Here,  $R^2$  represents the goodness of the linear fit.

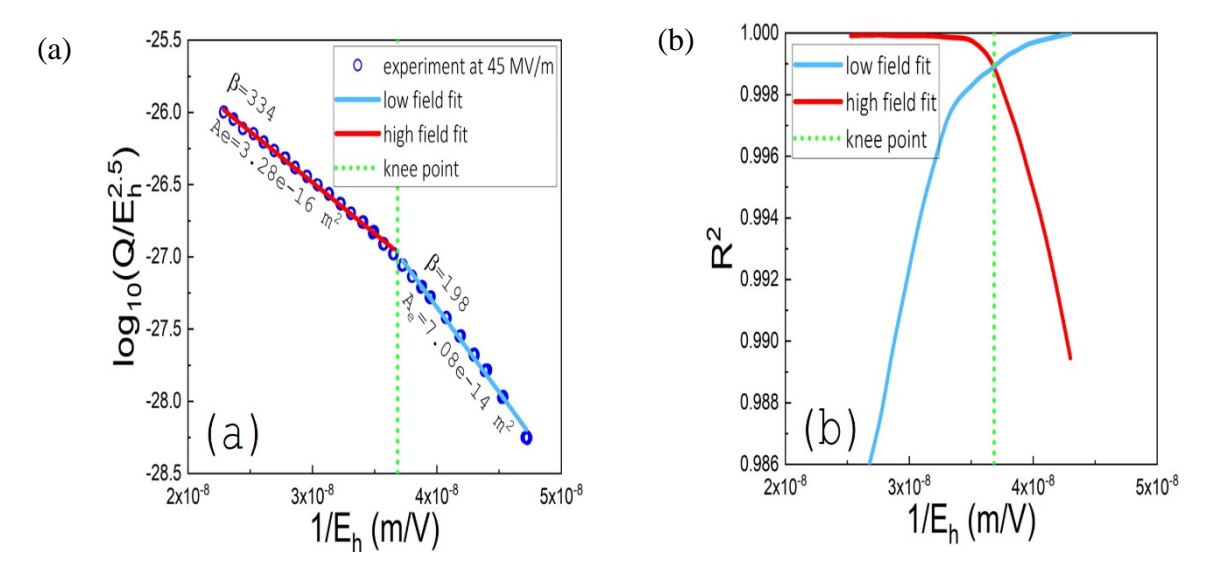


Figure. 4.1.5 (a) FN plot and (b) R<sup>2</sup> plot exampled for 45 MV/m. For all FN plot <u>Appendix B.</u> [33] It is not necessary to obtain permission to reuse this article or its components as it is available under the terms of the Creative Commons Attribution 4.0 International license.

After the knee point is selected, <u>FEbeam</u> performs FN fitting to two linear portions, separated by the knee point, in FN coordinates. Therefore, there are low gradient and high gradient portions of Q-E dependencies. For both portions, FEbeam then extracts the field

enhancement factor ( $\beta$ ), the local field on the cathode surface ( $\beta \times E_h$ ), and the effective emission area ( $A_e$ ) all as a function of the maximum achieved conditioning field ( $E_h$ ) per formalism below,

$$\beta = \frac{-2.84*10^9 \varphi^{1.5}}{s}$$
,  $A_e = \frac{10^{y_0} \varphi^{1.75}}{5.7*10^{-12}*10^{4.52} \varphi^{-0.5} \beta}$  Equation 4.1.2

where s and  $y_0$  are the slope and the y-axis intercept of the linear dependence, and  $\phi$  is the work function.

The result summary is presented in **Figure 4.1.6**.

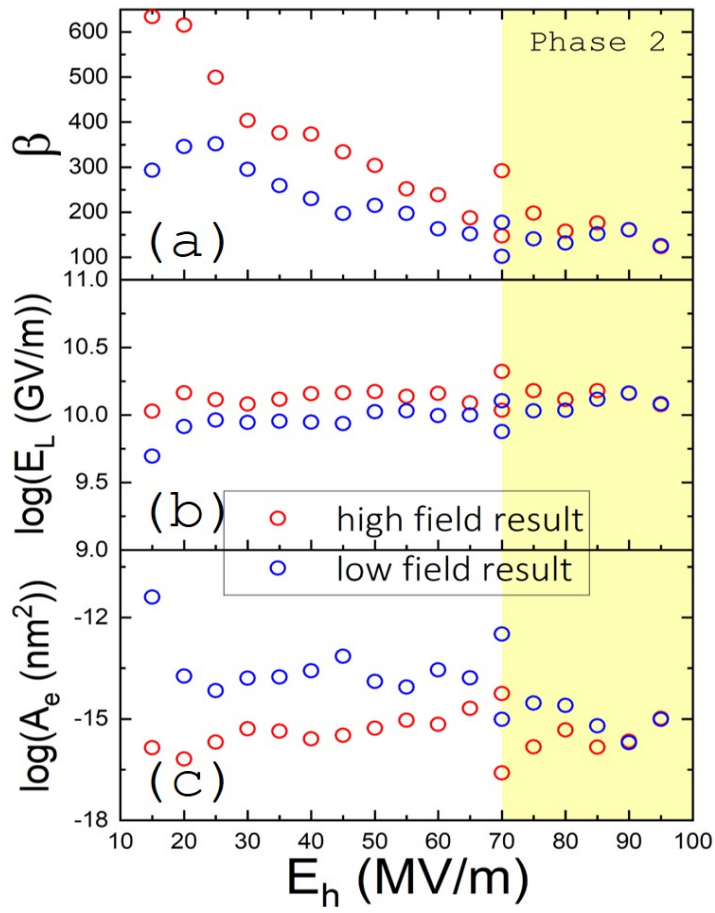


Figure. 4.1.6 Field emission conditioning parameters: (a) field enhancement factor, (b) local field on the cathode surface, and (c) effective emission area for both the FN-like (low field) and non-FN (high field) regions [33]. It is not necessary to obtain permission to reuse this article or its components as it is available under the terms of the <u>Creative Commons Attribution 4.0 International</u> license.

High field data results in overestimating the local field, as it is known that a local field above 10 GV/m may be unphysical due to exceeding the limit set by the lattice interatomic force.

This value includes diamond that breaks down at ~10 GV/m [10]. Experimentally, this would likely result in an immediate failure of the cathode due to breakdown induced runaway of the cathode material [11,12]. Since the cathode was not observed to behave this way, it is concluded that high field data overestimates the field enhancement factor. This over estimation causes the high field data to predict local fields in excess of 10 GV/m which is the breakdown threshold limit for diamond. Operating beyond breakdown limit would cause catastrophic failure of the cathode which was not observed with in this experiment for at any field. In contrast, low field data predicts the local field be below or at 10 GV/m. None of the datasets predicted the emission area correctly either in its magnitude or with respect to the gradient trend. Even though incorrect, the effective emission area for the low field portion decreases with  $E_h$  which is indicative of classical FN law [7]. High field portion predicts the effective emission area to be a nearly constant value. Therefore, the low gradient portion is attributed to the classical metal-like FN behavior, while the high gradient portion is driven by a different physical mechanism which is discussed further.

# 4.2 Surpassing the Child Langmuir limit and Development of the space charge dominated Fowler Nordheim regime

Generally, there are two competing hypotheses to explain deviation from FN behavior of planar FECs: (when charge grows slower than predicted by FN law). One is space charge limited emission [13, 14]. In this case, if an extensive charge is emitted and not removed away from the cathode's surface promptly, it may start screening the external electric field – hence, the emission curve diverges from the FN trend. The second of the competing hypotheses is based on resistance limited emission: in the 1960s, it was discovered that semiconductor and semimetal field emitters do not obey FN law. In experiments, the output current stops growing with the

electric field, and current-voltage characteristics switch from diode-like to resistor-like behavior. The ballast, or series resistance forcing the diode-to-resistor transition to take place, can be caused by the contact resistance [15] or by the transit time limited resupply of limited amount of charge being emitted through the limited amount of emission spots on the surface of the cathode [7, 16, 17]. Our leading hypothesis is that it is space charge that affects the emission and causes the observed divergence in this particular study. This is supported by a series of the following observations.

All measurements were done in fields stronger than 10<sup>4</sup> V/cm. This means that, at all gradients, charge drift can be expected to be saturated [15]. The number of emitters quickly increased and remained near a constant value as obtained by in situ imaging at  $E_h$  for every conditioning Q-E curve. For the purpose of this analysis, we were interested in the downstream imaging using YAG3 images as it enables the largest magnification and resolution (when coupled with the collimator at YAG2 position). To achieve high-resolution dark current imaging, a method to select electrons from certain emitting phases and narrow the energy spread was developed using external axial magnetic fields (i.e., solenoids) and a collimator at the focal plane, as is discussed in more detail in Ref. [18]. The resolution improves when smaller apertures are imposed. There is a trade-off between the resolution and the signal-to-noise. The standard technique is to apply a 1 mm aperture it enables strong signal and resolution of 100 μm. All imaging was conducted using a metal collimator with an on-axis centered circular aperture of 1 mm in diameter. The number of emitters (or local maxima in terms of image processing terminology) on the cathode surface was determined by processing a set of 18 raw 16 bit images using FEpic [16] shown in Appendix A in its entirety.

Each emitter that was determined to be present through image processing was assumed to have had the same area such that the total emission area was the number of emitters times the unit emitter area. The charge growth at every Eh point slowed down but did not plateau out on the semilog plot as it would be expected to be based on the series resistor model. This confirms the leading role of the electric field effects outside (and not inside) the cathode. Figure 4.2.1 sums up this representation by illustrating that the charge dynamics are driven by the electric field and not the emitter statistics (given the charge drift transport in UNCD bulk must be considered saturated at all gradients [17]). To further elaborate on these conclusions, we utilize 2D space charge formalism developed by Filippetto et al. elsewhere [19]. Having a field emission period of 38 ps in L-band, the generated beam can be termed as the cigar aspect ratio beam. Therefore, the 2D space charge formalism fully applies. Specifically, the following equation is used to fit  $Q_{max}$  vs. $E_h$  dependencies.

$$Q_{max}^{2D} = C_c I_A \frac{\sqrt{2}}{9} (\frac{eE_h R}{mc^2})^{3/2} \Delta t$$
 Equation 4.2.1

where Cc is an order-of-unity constant, R is the emission radius and  $\Delta t$  is the emission period equal to 38 ps.

The Phase 2 dependence was fit very well by Eq. 4.2.1 (purple dotted line and red square symbols), and an emission area radius of 13 µm was obtained (all other parameters were fixed). These results present direct evidence of the two-dimensional space charge limited emission. In Phase 1, the last three gradient points (60, 65 and 70 MV/m) were fit well by Eq. 4.2.1 (orange dashed line and red circle symbols), yielding an emission area radius of 37 µm. The gradients between 15 and 40 MV/m were fit well by a cubic law which **Eq. 4.2.1** becomes if the gradient and emission radius are both changing at the same time. This assumption is supported by the imaging results plotted on the same graph illustrating and confirming the validity of cubic law

application in this gradient range. While the gradient is changing from 15 to 40 MV/m, the emission radius is changing from 18 to 44 µm. The transition between 3 and 3/2 laws occurred between 40 and 60 MV/m and is not well captured in our experiments. The difference between extracted emission radii, 37 down to 13 µm, is consistent with the result seen in imaging: even though the main emission pattern remained after cathode reinstallation, the number of streaks (i.e., number of localized emitters) dropped. **Eq. 4.2.1** estimates this drop to be by a factor of 3. This is, again, is consistent with the image processing algorithm results that predicted a relative drop of the number of emitters by a factor of 2. Two observations are worth noting here: First, the emission area extracted from Eq. 3 is 10 orders of magnitude larger than that predicted from FN fitting as is depicted in **Figure 4.1.6**. Second, the space charge limited emission appears a better regime to extract the field emission area. The same phenomenon was observed in the transit time factor limited emission [7] which predicts a saturation in the effective emission area that resembles a more realistic observable field emission area as is supported by our image processing results.

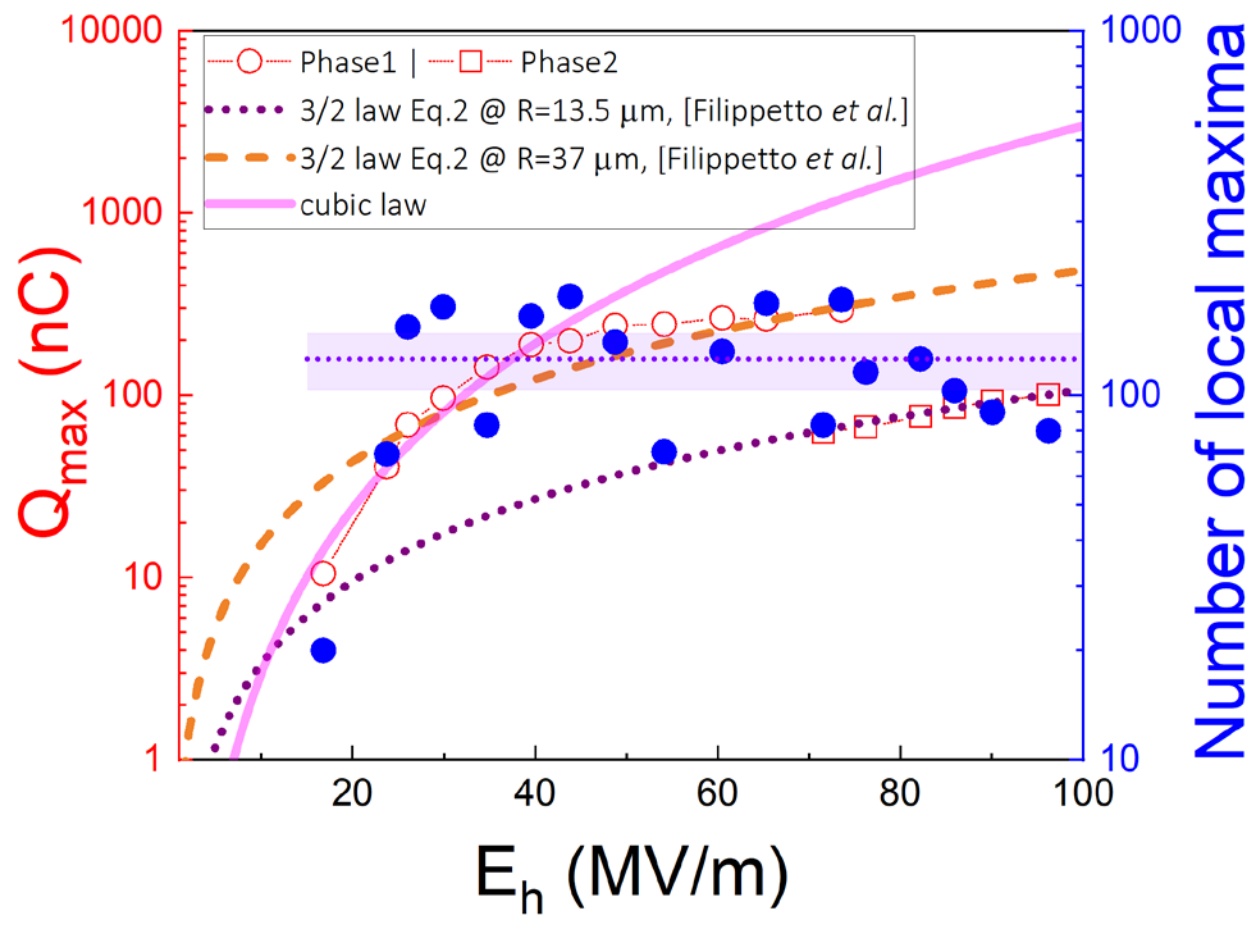


Figure 4.2.1 Maximum charge and the number of emitters determined at the maximum of every conditioning Q-E curve as functions of  $E_h$ . The purple horizontal area represents one standard deviation around the mean value of the emitter number count [33]. It is not necessary to obtain permission to reuse this article or its components as it is available under the terms of the <u>Creative Commons Attribution 4.0 International</u> license.

Combining the field emission Q-E characteristics with the emitter statistics presents clear evidence that the divergence from the classical FN regime is a result of space charge limited field emission. Confirmation that the emitter count is approximately constant while the charge grows as a function of Eh shows that the charge density is still growing throughout conditioning, though at a slower rate. The difference between the 1D Child-Langmuir law and 2D space charge limited emission, resulting from elongated beam due to a long launch phase window, is reinforced by the Millikan plot (a better way to visualize the space charge onset [20])

corresponding to 95 MV/m, as shown in Figure 4.2.2: the charge surpassed what the Child Langmuir limit predicts. A small parallel shift can be observed which is indicative of switching to space charge limited emission for high work function materials (>3.5 eV) [21]. In our experiment, the 1D limit was surpassed by a factor of 2. In a different version of a 2D space charge case, Luginsland et al. [13] demonstrated how the Child-Langmuir problem considered in 2D led to surpassing the classical 1D law of 2/3: 2D current was higher than 1D current by a factor of 4 where the 2D limit is extracted from the fitting to the Filippetto equation and the one-dimensional limit is extracted from the Millikan plot where our results intersect the one-dimensional Child Langmuir law as seen in Figure 4.2.2.

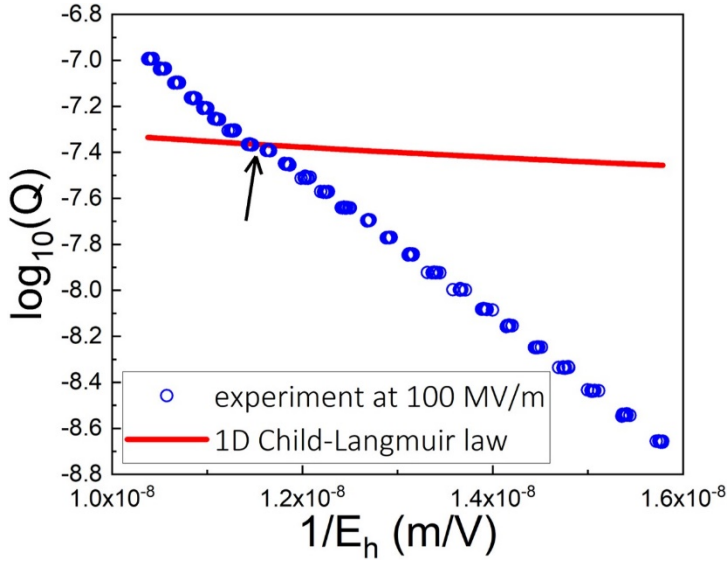


Figure. 4.2.2 Millikan plot for 100 MV/m (red) showing the parallel shift denoted with an arrow and is indicative of a space charge dominated regime that differs from the Child Langmuir law (blue). Additional Millikan plots can be seen in Appendix B. It is not necessary to obtain permission to reuse this article or its components as it is available under the terms of the Creative Commons Attribution 4.0 International license.

Additionally, the crossing point of the Child Langmuir limit is specific to this particular cathode. As a different cathode with different current density which is proportional to the number of emitters would have a different crossing point. Cathodes with different work functions

would also have a different behavior with respect to their Millikan plot behavior and could have a different slope on their pre-crossing point behavior. Thus, the next step as explored in CH5 would be to explore the different behaviors of material science on the crossing point in behavior of surpassing the Child Langmuir limit as a function of the cathode material parameters.

#### 4.2.1 Production of bright beams

Finally, we used the estimated effective emission radii (37 µm in Phase 1 at 70 MV/m and 13 µm in Phase 2 at 95 MV/m) obtained from Eq. 3 and corresponding charges per rf cycle (38 pC in Phase 1 at 70 MV/m and 13 pC in Phase 2 at 95 MV/m) to track the brightness evolution from the cathode surface to the gun exit and down the beamline all the way to YAG3. The summary plots in **Figure 4.2.3** include all the emittance components used in the brightness evaluations, namely space charge, intrinsic and rf emittances. The intrinsic emittance was evaluated from a previously measured mean transverse energy value of 100-200 meV [20]. The presented end-to-end beam tracking results further reinforce that, in the gun, the beam is dominated by the space charge force leading the transverse brightness to settle at approximately  $10^{14}$  A/(rad m)2, the gun brightness in both Phase 1 and Phase 2. Outside the gun, from 1 to 9 ns, the rf emittance takes over due to longitudinal beam stretching caused by the launch phase effect. With this drift to YAG3, the brightness quickly dropped to insignificant values. As stated before, this rf emittance growth is responsible for the YAG3 image streaking.

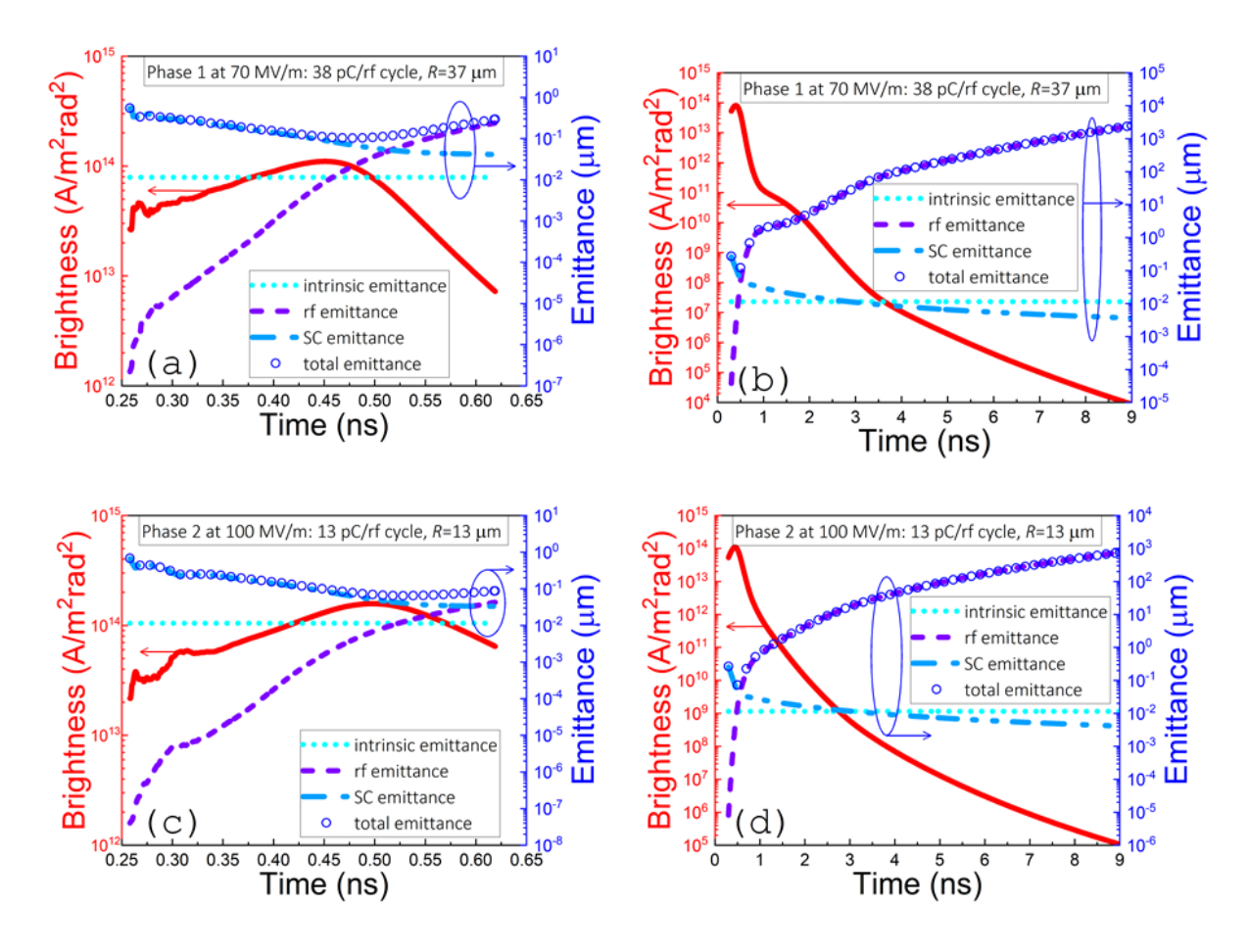


Figure. 4.2.3 Brightness dynamics inside the gun for (a) Phase 1 and (c) Phase 2 (0.45 ns timestamp corresponds to the physical end of the gun cavity) and along the entire beamline from the cathode to YAG3 for (b) Phase 1 and (d) Phase 2. For reference, the gun exit corresponds to the time stamp of 0.6 ns for all the figures [33]. It is not necessary to obtain permission to reuse this article or its components as it is available under the terms of the <u>Creative Commons Attribution 4.0 International</u> license.

The analytical calculations using the formalism presented in the Introduction section predict the gun brightness of  $\sim 10^{14}$  A/(rad m)<sup>2</sup> which is close to the exact metrics found in GPT. The same formalism suggests that suppressing the temporal emission window to a few or subpicoseconds would minimize the dominating factor of rf emittance within the drift space. Additionally, still by the same formalism, enabling cathode gradients between 300 and 500 MV/m could provide a practical path towards brightness well above  $10^{15}$  or near  $10^{16}$  A/(rad\*m)<sup>2</sup> for a C- or X-band injector family, which would be a technological breakthrough. Some practical

techniques for longitudinal suppression are 1) direct gating or frequency mixing in the gun [22], 2) obtaining a specialty multi-cell gun design, or compressing the beam with either [23] 3) an external TM10 cavity [24] or 4) a self-wakefield structure followed by ballistic bunching or chicane lensing [25]. While offering injector simplicity over photocathodes especially in high frequency systems, field emitters would be electron sources of choice for many applications if a certain level of coherent beams can be experimentally proven. The validity of these FECs will require knowledge of the interplay between the emitted charge and the emission area and, therefore, would require a detailed study. In this case, operation using planar field emitter geometries is required to avoid physical disruption of the cathode.

The next section builds upon the previous work with UNCD and uses micro diamond, which has a much lower charge, to probe the effects on field emission performance of the space charge and other field emission mechanism such as the ballast resistance. These micro diamonds were formed into individual pyramid geometries in a triangle array where differences in the growth process caused differences in the geometry and the materials properties of two different cathodes. This allowed for the evaluation of the effects of the material and the geometry on FEC performance. It was shown that the materials properties are dominant when compared to the effects of the geometry, verifying the hypothesis presented in CH2.

### 4.3 Effects of Geometry and Material Properties on Production of Transversely Shaped Beams using Diamond Field Emission Array Cathodes

To engineer a field emission cathode (FEC) best suited for a specific application, one must consider both the geometrical design and properties of the precursor material. The geometry remains the dominant ideology when useful designs are considered: the field enhancement factor which determines the FEC performance is viewed to be of a purely geometric nature [26,27,28].

This approach has two issues: 1) field enhancement factor is not a global constant for a FEC [1, 2] and 2) This approach becomes insufficient or rather fails when highly efficient planar FEC are attempted [16]. The FEC view that takes material properties has been limited to the search for the lowest work function. This limited arsenal is a result of the elementary Fowler-Nordheim (FN) equation ubiquitously utilized to describe any FEC as an ideal conductor that with only two properties: the field enhancement factor and the work function. Thus, FN does not consider realistic differences between metals, semiconductors (and doping effects), or dielectrics.

Recently, diamond field emission arrays (DFEAs) attracted significant attention due to their ability to produce transversely shaped electron beams. When combined with emittance exchange techniques, DFEAs represents a technology that is critical for the development of the next generation wakefield structure or plasma accelerators. Even though a triangular shaped beam was successfully demonstrated recently using a DFEA FEC, the mechanism behind why some DFEAs can produce a shaped beam while other geometrically similar DFEAs cannot remains elusive. Here, two DFEA FECs are tested in the same rf injector. By doing so, the effects of geometry and materials are systematically addressed. One cathode that had poorer geometry successfully produced the shaped beam while another one did not. Based on Raman spectroscopic mapping and in situ field emission imaging, a hypothesis was formulated to explain the major difference in the DFEA FEC performance.

In the tests described in this paper we used two diamond field emitter array cathodes that we will from now on refer to as a cathode A and cathode B. Both, cathode A and B were fabricated under the same growth conditions at the same time. DFEAs are periodic arrays of micron-scale nitrogen doped micro-diamond pyramids with sharp nanometer-scale tips. DFEAs on both cathodes were made in the form of a triangular pattern, multiple pyramids formed an equilateral

triangle with a side of 1.025mm $\pm$  50  $\mu$ m. Each diamond pyramid had a base of 25  $\mu$ m  $\pm$  1  $\mu$ m, and the height-to-base ratio of 0.7 to 1. The process to create a DFEA cathode is explained in previous

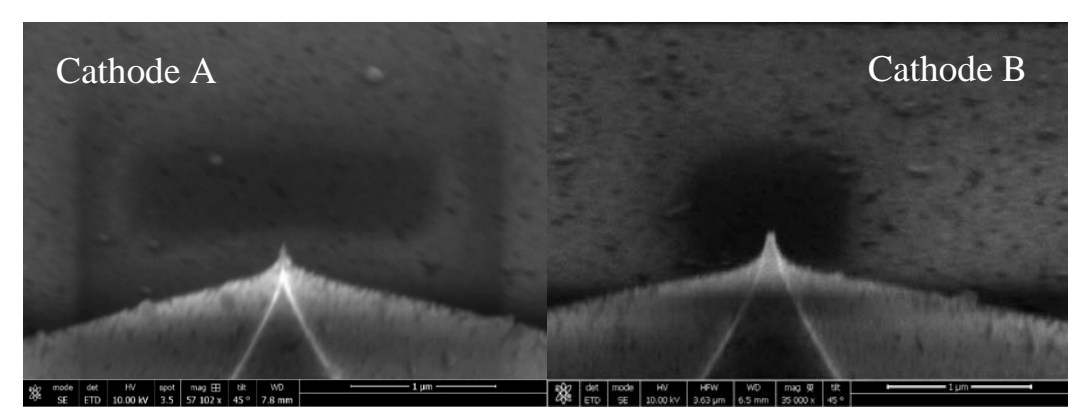


Figure. 4.3.1 SEM image of a single emitter pyramid showing the sharpness of the emitter tip for cathode A and cathode B.

works in Ref. [31]. Diamond is deposited into molds of inverse pyramid arrays lithographically etched in a silicon substrate. Diamond deposition was performed commercially at Advanced Diamond Technologies in Romeoville, IL. After the diamond growth is complete, the microlayer of diamond with pyramids is brazed onto a molybdenum substrate that becomes the actual cathode plug for the three-part assembly described in [3]. Small variations in the mold, such as sharpness of the edges and angles of the inverse pyramids, as well as the growth process for the diamond led to variations in both the material composition and the geometry for the two cathodes. Scanning electron microscopy (SEM) images of the two cathodes are shown in **Figure 4.3.1** and reveal that cathode A had much sharper, smaller diameter tips than cathode B.

The cathodes were tested and imaged in high gradient environment in the L-band Argonne Cathode Test-stand (ACT) with an rf pulse length of 6 µs at 2 Hz repetition rate in and at vacuum ~10<sup>-9</sup> Torr. Detailed description of the ACT can be found in CH2.1 .Based on the standardized conditioning procedure presented in great detail in Ref. [3], the turn-on fields were 22 MV/m for cathode A and 24 MV/m for cathode B. All conversions of raw data to the resulting Q-E curves were obtained using a custom pipeline called FEbeam [8]. This turn on field

is ~10 MV/m larger than the turn on field measures for previous diamond cathode diamond-based cathodes. Although the turn on field was detected using the *in situ* YAG imaging system, the first Q-E curve were obtained for 30 MV/m and 32 MV/m, respectfully, for cathode A and cathode B as the charge before this gradient was below the detection threshold of the Faraday cup circuitry. As **Figure 4.3.2** shows, both cathodes performed similarly, producing a maximum charge of ~0.5 nC per rf pulse and achieved a maximum field of 45 MV/m. Both the cathode started to decay in performance by having a decrease in charge at fields in excess of 42 MV/m which is consistent with other results using DFEA. Further on, the Q-E data can be represented in the FN coordinates, for rf environment it reads  $log_{10}(Q/E^{2.5})$  vs. 1/E.

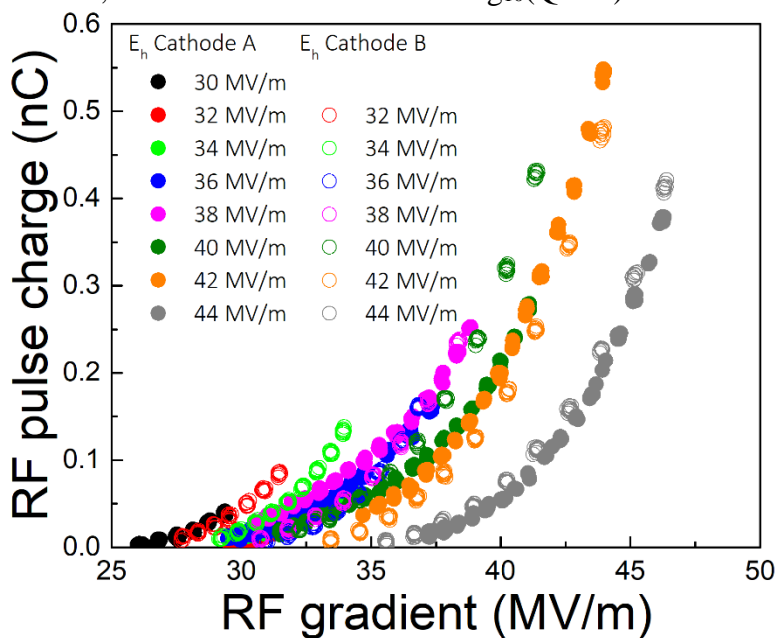


Figure. 4.3.2 QE curves for cathode A and cathode B respectfully.

From **Figure 4.3.3**, it is seen that the dependence is ideally linear, and therefore effects from space charge form CH 4.1 and current saturation CH 4.2 can be excluded.

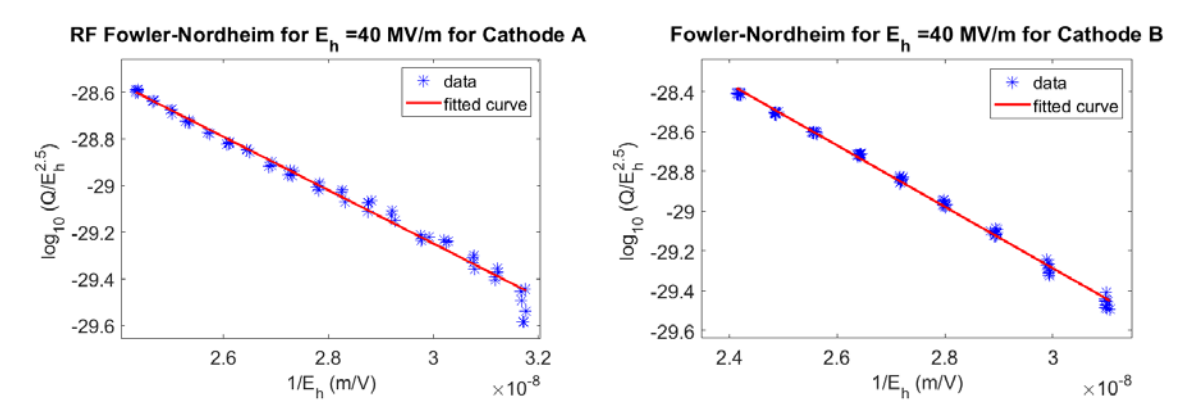


Figure. 4.3.3 FN plots for cathode A and cathode B both conditioned to 40 MV/m showing ideal linearity.

These results show even though both cathodes performed similarly with respect to maximum charge output and maximum achievable applied fields, they performed substantially different in terms of producing the shaped beam. *In situ* imaging of cathode A showed no shaped beam formation, and only a large electron halo-like cloud was found, as depicted in **Figure 4.3.4**, with no individual emitters resolved. On the other hand, cathode B clearly showed a triangle emission pattern. Since FN suggests no space charge force playing role, the observed difference

in performance merits further discussion. Geometrical and material properties are further evaluated to play major role in producing desired shaped beams.

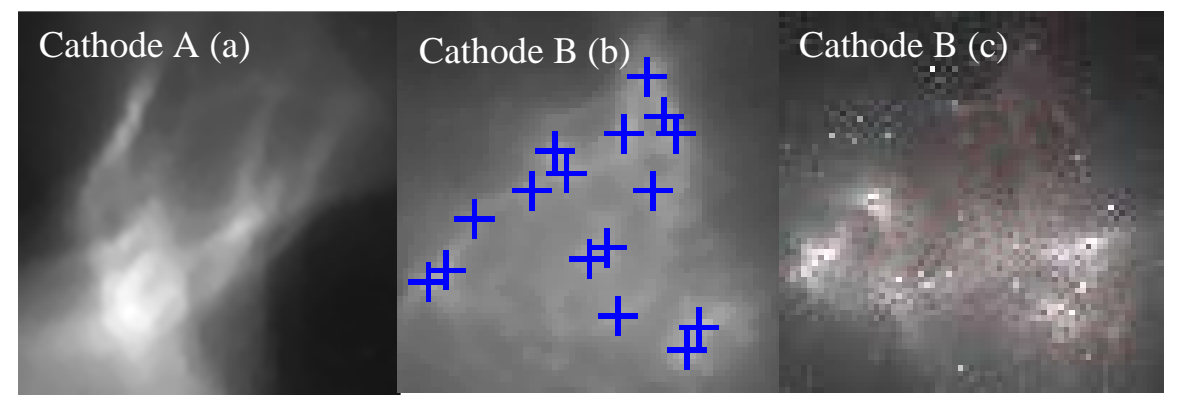


Figure. 4.3.4 Image taken on YAG3 at 40 MV/m for cathode A and cathode B. Cathode A showing no pattern beam and a large electron cloud due to space charge domination. Cathode B showed a pattern of emission and local maximum determined using FEpic blue crosses in center picture (not to scale); (c) Overlay of the initial DFEA pattern times a magnification factor of 12 (red dots) and the local maximums determined from FEpic (blue). Marker size is to scale at E<sub>h</sub>=30 MV/m.

#### 4.3.1 Evidence for negligible role of Geometry effects on FEC performance

Cathode B images were processed using a custom algorithm <u>FEpic</u> [16] which spatially detects emission center locations. It was found that the spacing between local maximum corresponded to integers of the initial spacing times the magnification factor. When overlaying with the initial DFEA SEM pattern, it can be seen that the emission pattern as well as the spacing between emitters was preserved (**Figure 4.3.4**). from this, it was found that the magnification was constant throughout the entire conditioning procedure, and magnification was 12±2. The constant magnification is because at the imaging plane of the ACT diagnostics beamline the emittance is dominated by the rf component. Since the rf emittance is a property of the accelerating structure, the magnification is a constant regardless of the cathode under test. Previous work has consistently shown magnification of ~10 [29]. The spacing downstream was approximately three pixels which

corresponded to length of 300 µm with an uncertainty of half a pixel, i.e., 300±50 µm. Since each identified emitter was only one pixel in length, it was determined that the effective emission size was 8.33±4.39 µm (0.33 is a repeating value). Capture ratio calculated using General Particle Tracking (GPT) environment aided by custom developed field emission particle generator <u>FEgen</u> [4] supports this result. **Figure 4.3.4** suggests no space charge. Therefore, capture ration should be close to 100 throughout the conditioning process.

From Figure 4.3.5 it can be found that it is possible if the emitting radius is ≥10 µm, otherwise the capture ratio drops, and the emitted charge does not leave the injector i.e., does not reach the Faraday cup. Together, the measurement and GPT simulation show that about half of the total pyramid shaped emitter actually emits electrons. This result is in stark contrast to the elementary FN approach implying that the emission comes from the very tip. The grown DFEAs are not intentionally doped and despite containing conducting sp² grain boundaries remain fairly large bandgap semiconductor. This result confirms the previous studies that showed no direct geometrical enhancement played role [29,31]. The field can completely penetrate into the material and the actual geometry should play minor role.

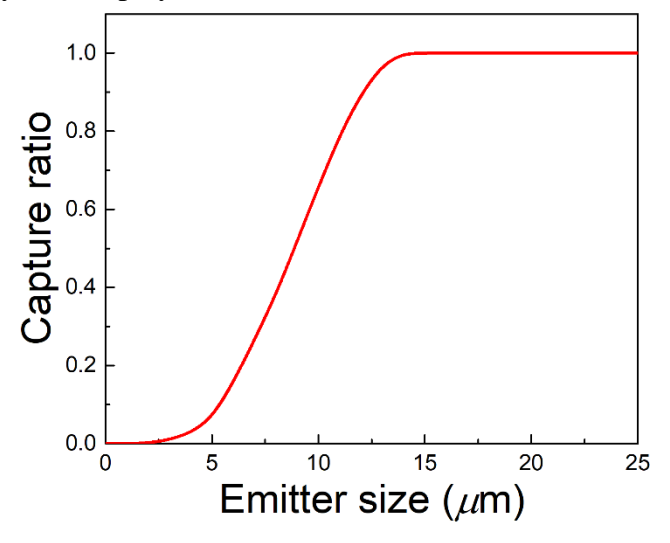


Figure. 4.3.5 Faraday cup capture ratio at Eh=40 MV/m as a function of emitting tip size.

#### 4.3.2 Materials Properties of FEC performance

Next, Raman spectroscopic mapping was deployed to gain insights into material itself and find if cathode A and B are similar or different. Assess the diamond across the array, Raman spectrum was taken on both tips and base to sample the pyramids on the edge, middle, and center. Figs. 6a and b show which tips for each pyramid were measured using Raman spectroscopy. The Raman spectra indicated that both DFEAs consisted of pyramids made out of microdiamond. Micro (and any other type of polycrystalline) diamond is defined as having a very narrow sp<sup>3</sup> peak which is centered at 1332 cm<sup>-1</sup> and called the D peak. Unlike single crystalline diamond, there is a large sp<sup>2</sup> peak called G peak which reflects the presence of carbon grain boundary phase [1]. Sampling the different pyramids across the array determined that cathode B (see Figure 4.3.6d) had a uniform quality across the array. On the other hand, as can be found from Figure 4.3.6c cathode A was shown to have a gradient in the diamond quality across the array. Cathode A was graphitized stronger: e.g., blue curve in Figure 5c, shows that the D peak is missing while the G peak is upshifted to 1600 cm<sup>-1</sup> which indicated that location to be a polycrystalline (likely nanographite). All locations across cathode A showed that G peak is located between 1585 and 1600 cm<sup>-1</sup>, while G peak for cathode B is at 1570 with no visible variation. Lower wavenumber position of G peak of cathode B suggests that the grain boundary phase is more amorphous.

Together with obviously larger diamond content, it means that cathode B should have a much (factor 100 to 1000) higher resistivity than cathode A.

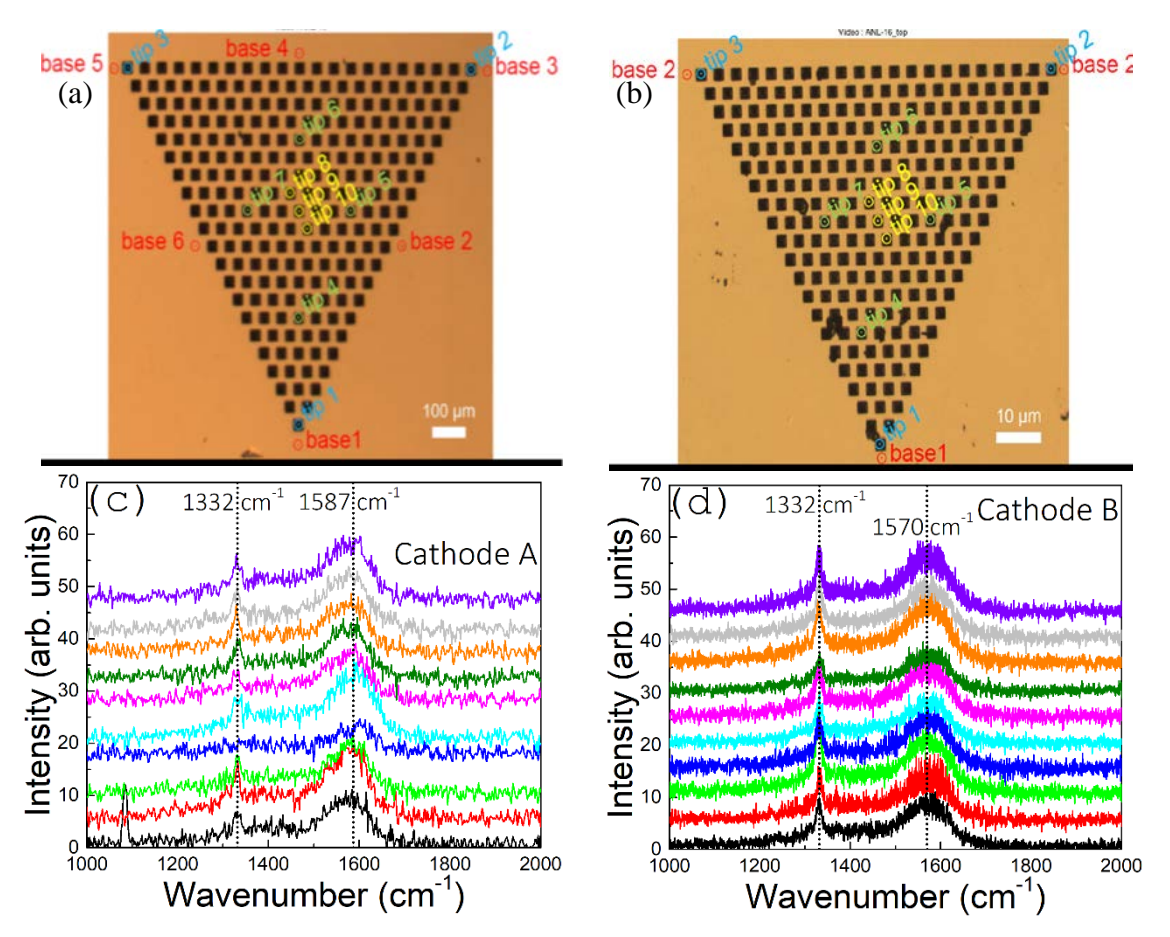


Figure. 4.3.6 Raman spectrum comparison between cathode A and cathode B, locations of tips (a) measured for Raman spectrum seen in (c) for cathode A. Likewise locations of tips (b) measured for Raman spectrum seen in (d) for cathode B.

Summarizing, the effects of geometry and material properties on production of transversely shaped beams using diamond field emission array cathodes were evaluated. It was shown that emission is not localized to the tip but instead a larger (100×) portion of the entire emitter can generate and emit electrons. DFEA that produced shaped beam (cathode B) has a better emission uniformity across the array that is driven by better material quality uniformity and (maybe more importantly) has larger resistivity translating to a larger resistance if geometry is nearly identical. This result is known in field emission designs and is called built-in ballast

resistance effect [25] that can stabilize operating point, i.e., make diode emission characteristic locally more uniform.

**Figure 4.3.7** illustrates this effect in more detail. Four diode exponential curves represent the difference between the emitter tips in the DFEA array. In the load line representation, the ballast resistance can be seen as a negative slope line, where the line angle is the reverse of the resistance.

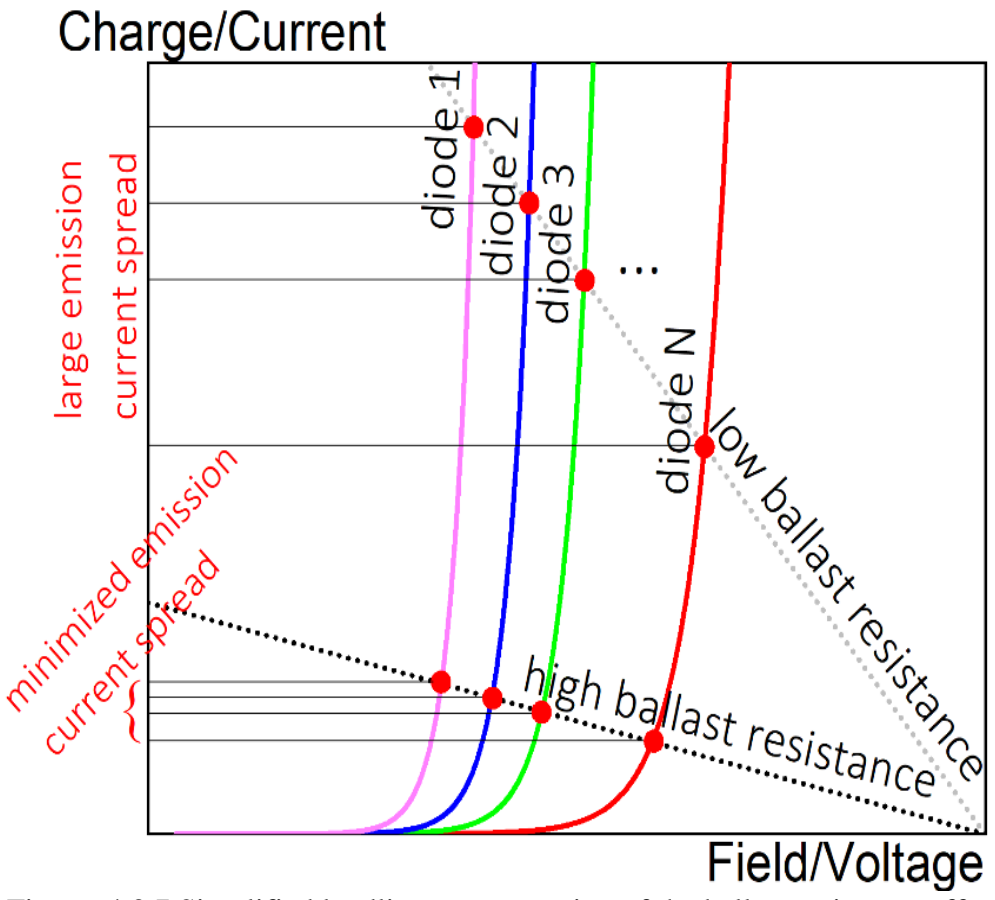


Figure. 4.3.7 Simplified loadline representation of the ballast resistance effect.

For the low ballast resistance (cathode A), the line crosses the diode characteristics such as the current spread is large. In extreme case with no ballast resistance, at low voltage/field diode 1 would turn on and emit all the current. As the field would progress to grow, other diodes would start turning on but the current from diode 1 would be extraordinarily high and it would likely to quickly extinguish due to thermal damage. On the contrary, cathode B with higher

ballast resistance allows for smaller current/charge per tip but all the tips work coherently providing in total large amount of current/charge. This is consistent with the Q-E and imaging results that show the same output charge but different number of emitters across DFEA contributing to the resulting charge and emission profile.

If geometry plays role, this appears to be a minor role. This result is consistent with pioneering results by Jarvis et al. [32] who showed that DFEAs showed best performance after conditioning process that would turn initially sharp tips to dull. Given new understanding, new modifications, and future work to the DFEA geometry and material will allow use of these sources for bright beam and emittance exchange applications for advanced accelerator concepts.

This ballast resistance model matches with the ongoing studies of this group to understand the field emission dynamics beyond classical Fowler Nordheim. Recent DC measurements have shown that when there is transport limited emission which caused a

deviation from the Fowler Nordheim as is mentioned previously in the introduction (see **Figure 4.3.8**).

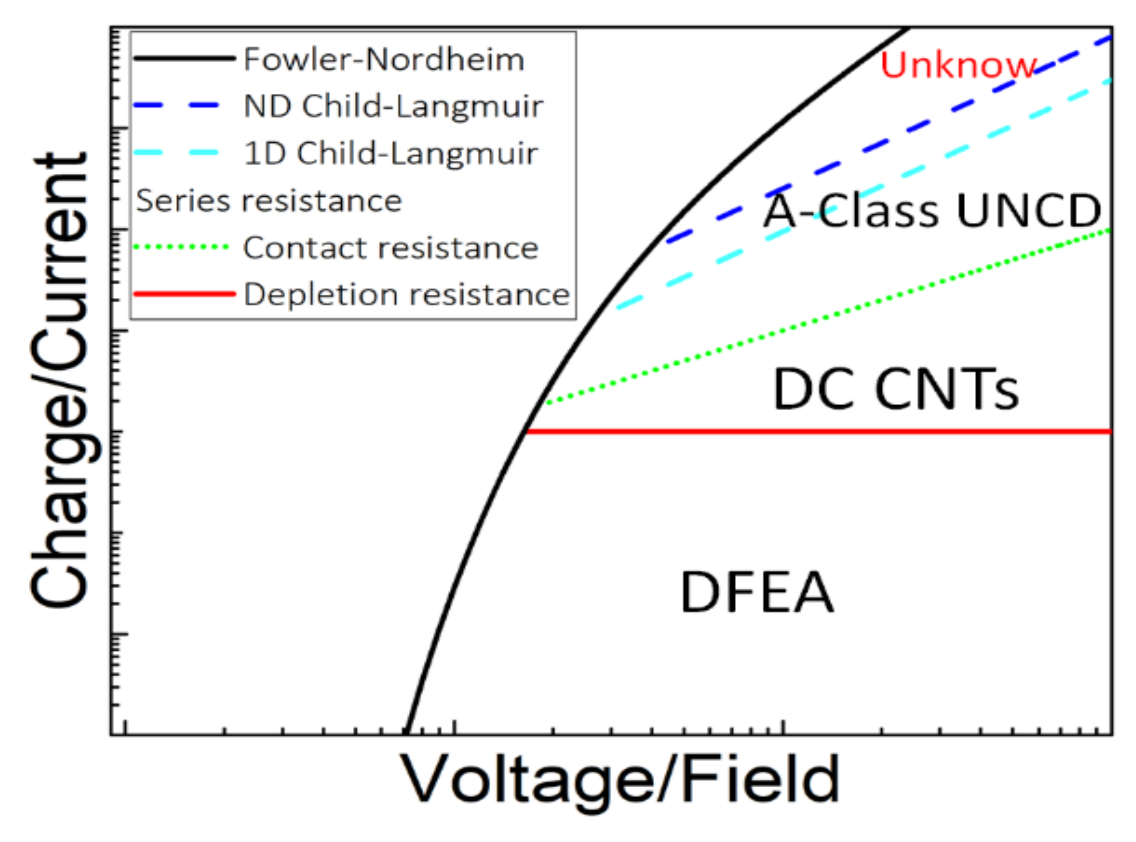


Figure. 4.3.8 Concept map showing the different regions of field emission dynamics under high charge high gradient conditions.

Explaining this deviation is not the purpose of this report and can be seen in work from Taha Posos. On the Black line, the work using DFEA showed no deviation from Fowler Nordheim and thus can be defined as classical Fowler Nordheim with a low ballast resistance contribution which describes the possible effects between the two different cathodes. There is also ongoing research for pulsed power community that does not surpass the Child Langmuir limit but is extremely space charge dominated and resembles a diode like behavior. Finally, this work presents space charge dominated Fowler Nordheim which is not Child Langmuir limited but shows its severe deviation from classical Fowler Nordheim behavior.

With an understanding of field emission dynamics beyond classical Fowler Nordheim, the next step in building high power injectors is to explore the regions beyond Child Langmuir. The particle dynamics at this point would not deviate from Fowler Nordheim and would start to trend back to a classical regime. However, reaching this unexplored region is only possible through the creation of new injectors. These higher frequency injectors (C though W band) would utilize the ultrahigh gradients beyond the limitations of current L band (i.e., 100 MV/m). The next chapter discusses the ongoing work in developing high gradient C band accelerating structures and the possibility of building the next generation of high gradient injectors.

# **APPENDICES**

**APPENDIX A:** Processed images indicating the number of local maxima found for each image from FEpic

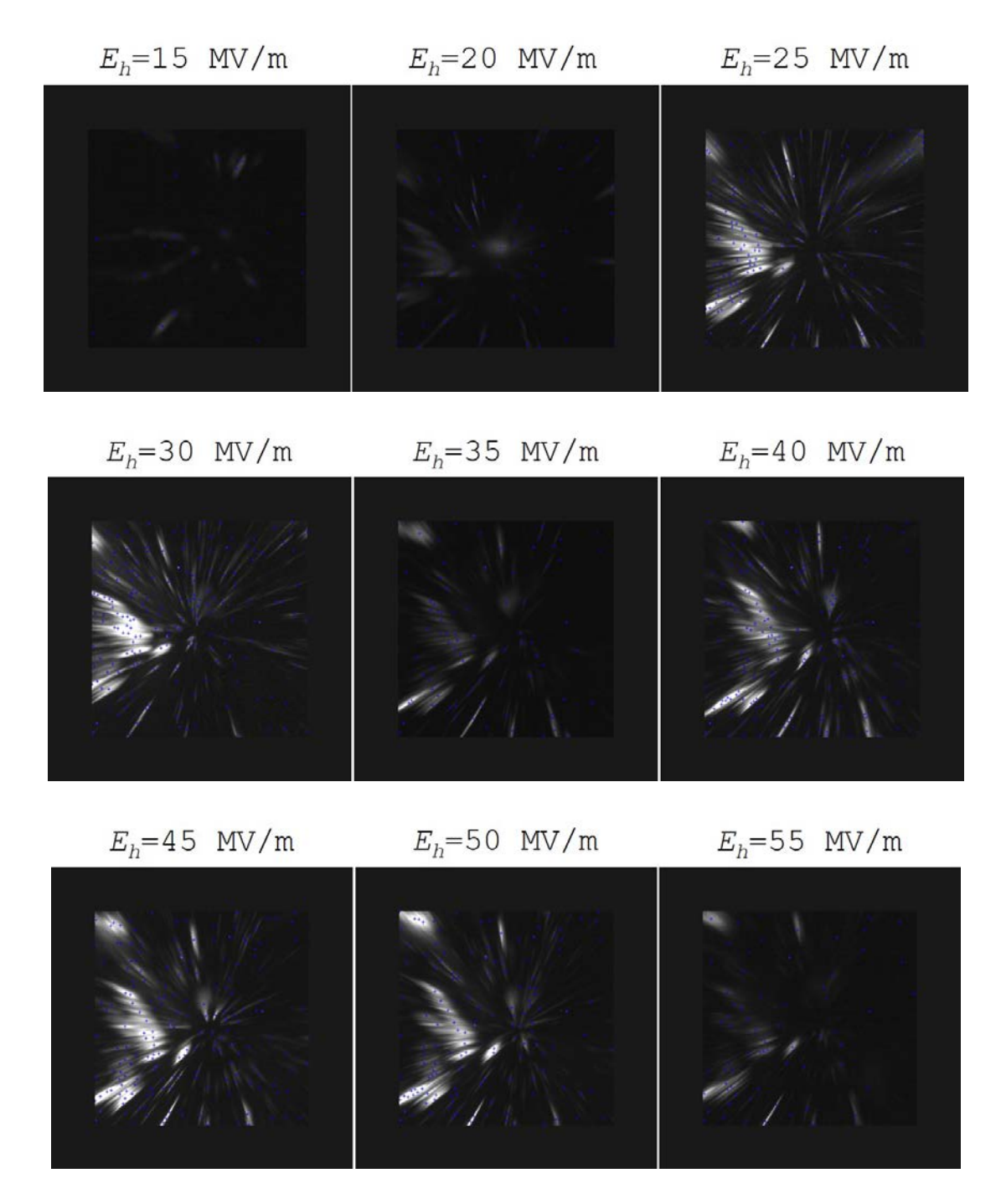


Figure A 1 Processed images indicating the number of local maxima found for each image from  $E_h$  15 to 55 MV/m from FEpic.

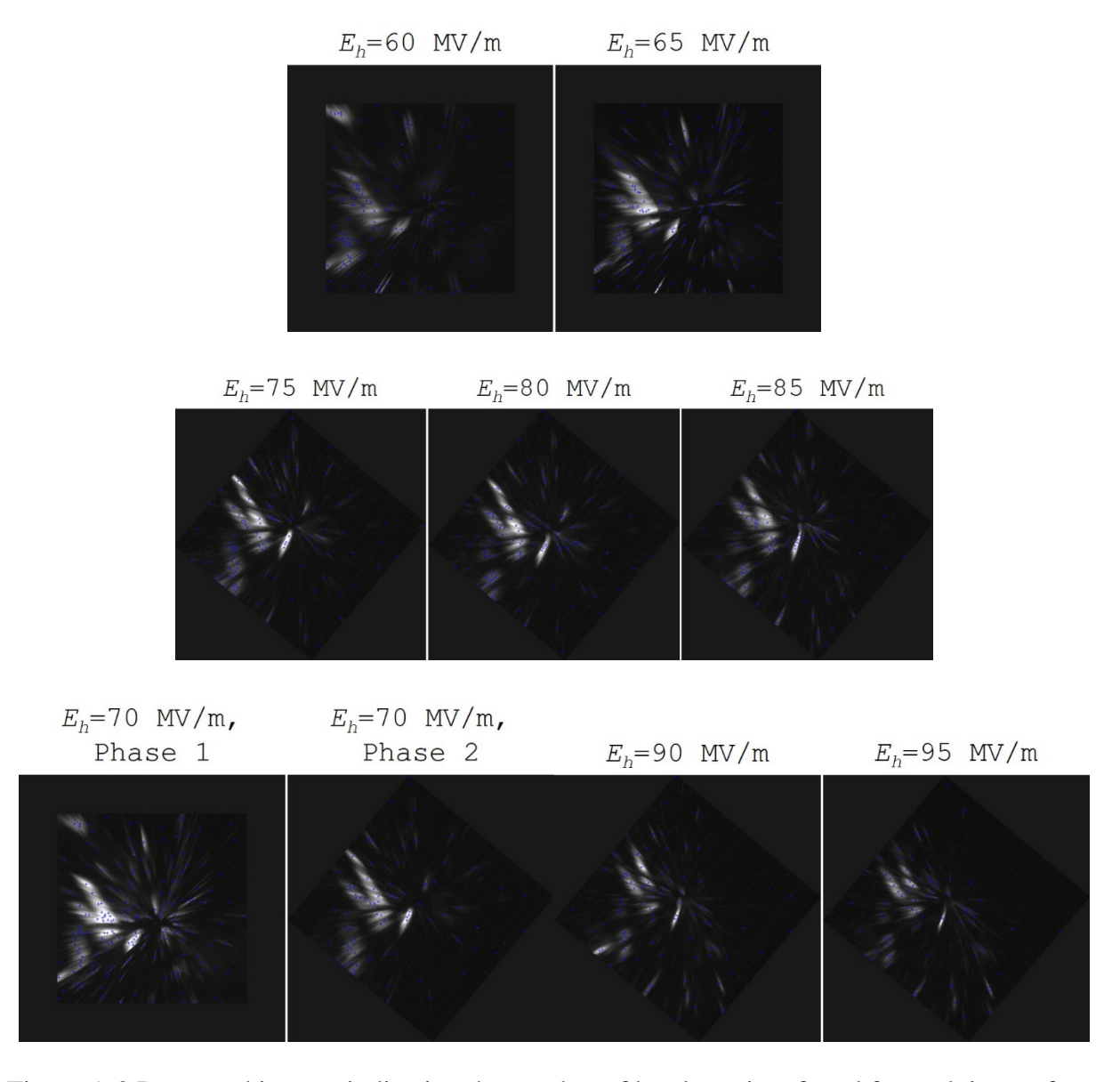


Figure A 2 Processed images indicating the number of local maxima found for each image from  $E_h$  60 to 95 MV/m from FEpic.

### APPENDIX B: Fowler Nordheim plots, knee point decision plots, and Millikan plots

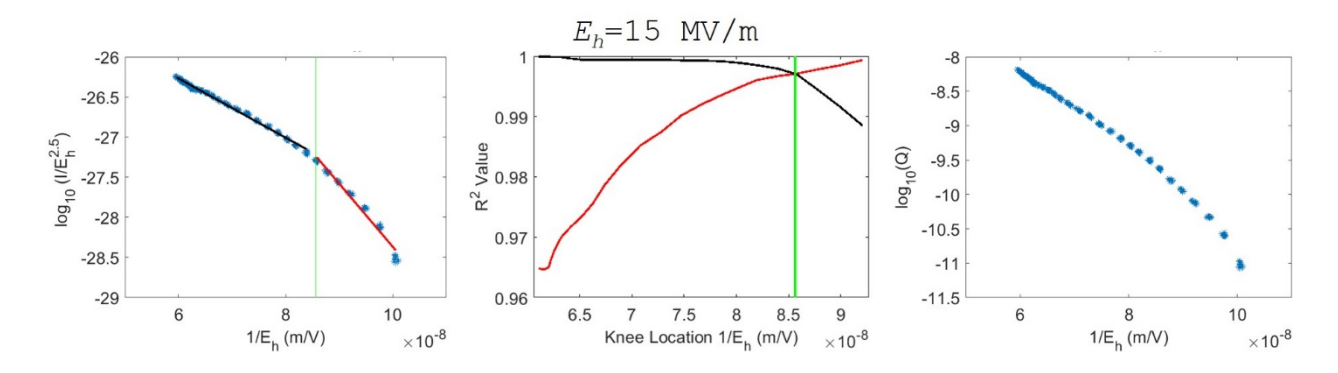


Figure B 1 E<sub>h</sub>-15 MV/m Fowler Nordheim plots, knee point decision plots, and Millikan plots.

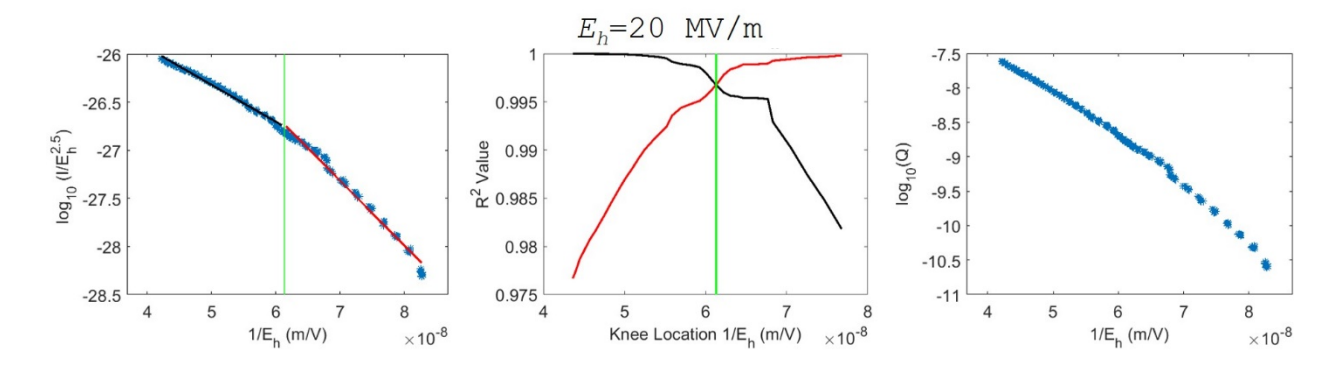


Figure B 2 E<sub>h</sub>-20 MV/m Fowler Nordheim plots, knee point decision plots, and Millikan plots.

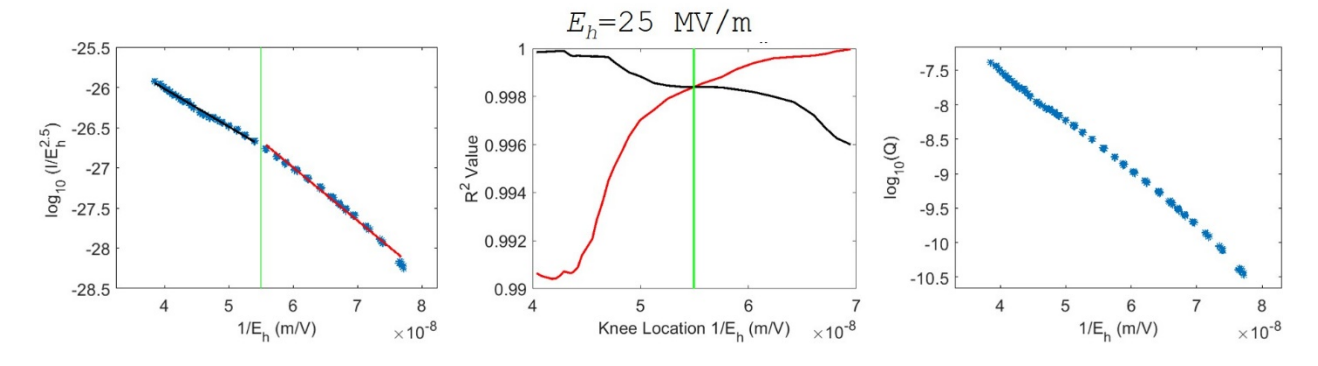


Figure B 3 Eh-25 MV/m Fowler Nordheim plots, knee point decision plots, and Millikan plots.

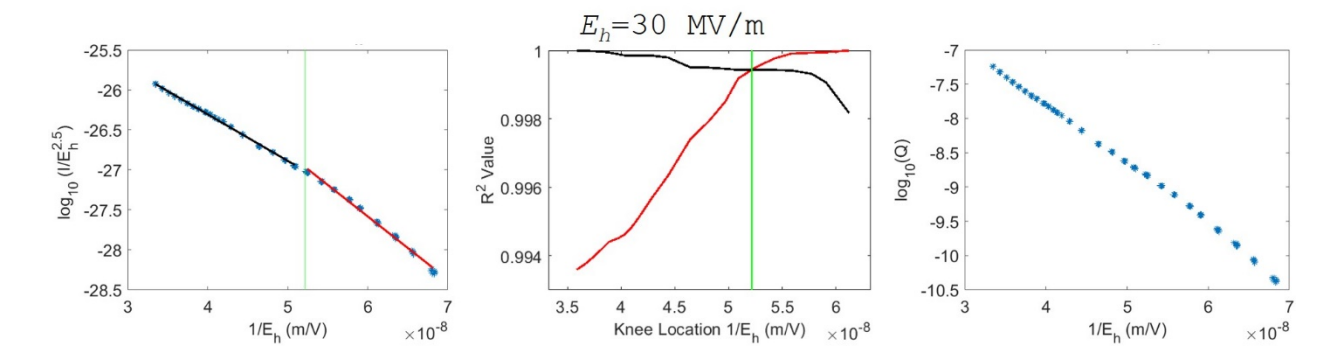


Figure B 4 *E*<sub>h</sub>-30 MV/m Fowler Nordheim plots, knee point decision plots, and Millikan plots.

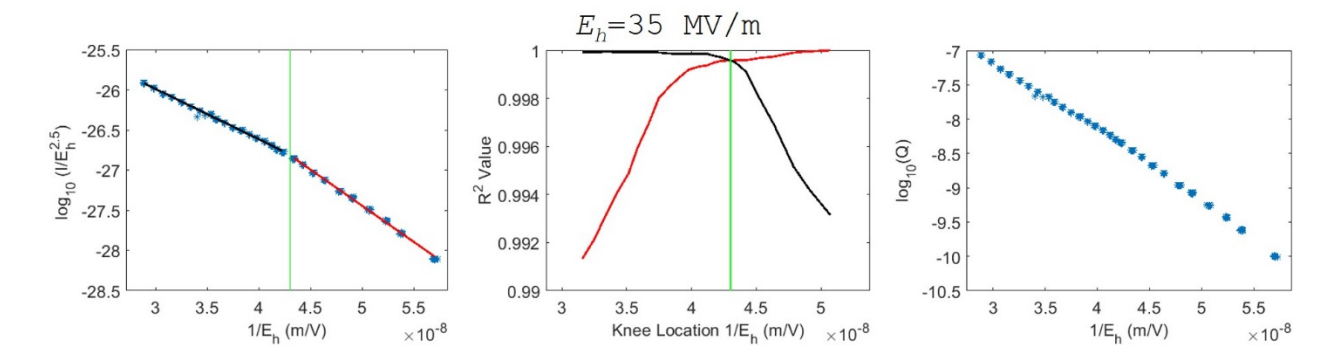


Figure B 5 *E<sub>h</sub>*-35 MV/m Fowler Nordheim plots, knee point decision plots, and Millikan plots.

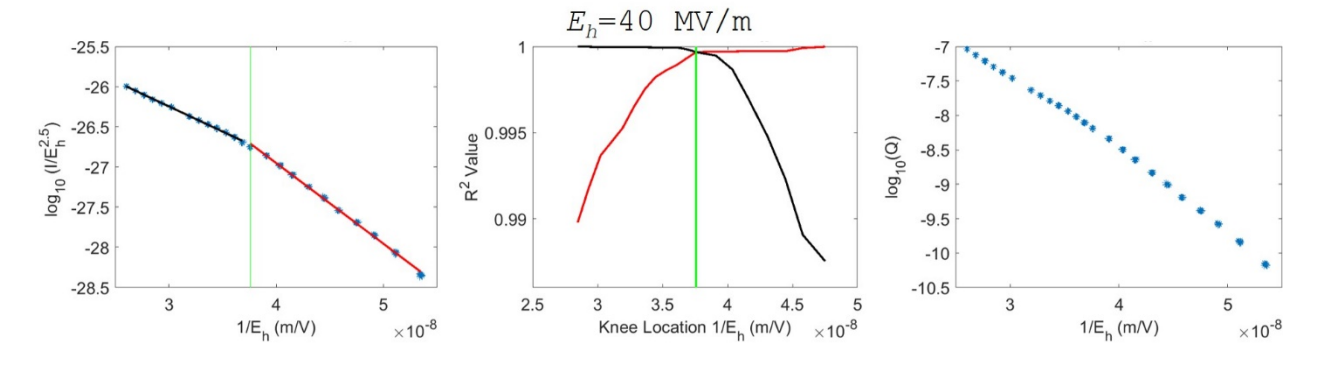


Figure B 6 E<sub>h</sub>-40 MV/m Fowler Nordheim plots, knee point decision plots, and Millikan plots.

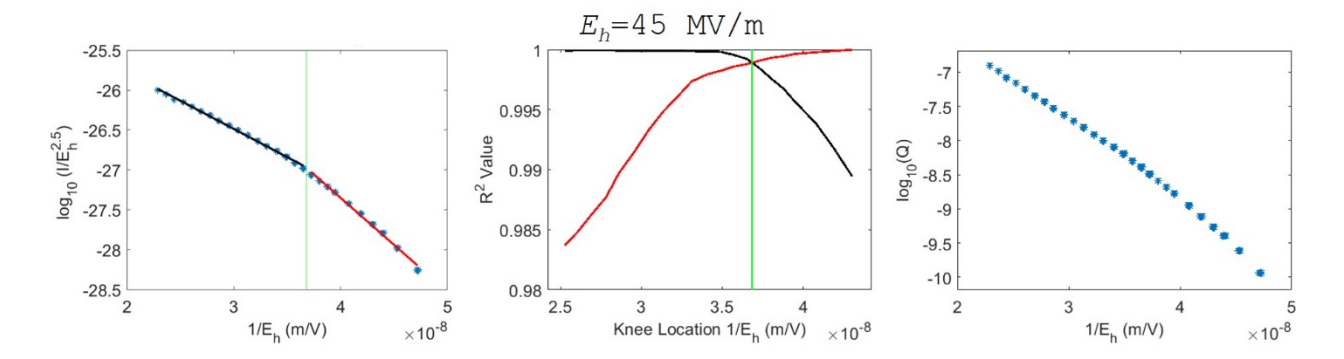


Figure B 7  $E_h$ -45 MV/m Fowler Nordheim plots, knee point decision plots, and Millikan plots.

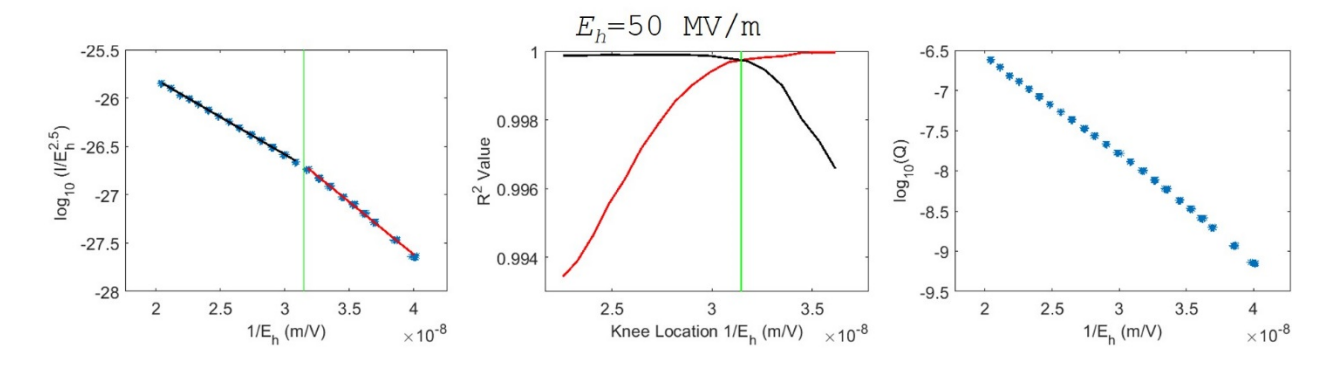


Figure B 8 *E<sub>h</sub>*-50 MV/m Fowler Nordheim plots, knee point decision plots, and Millikan plots.

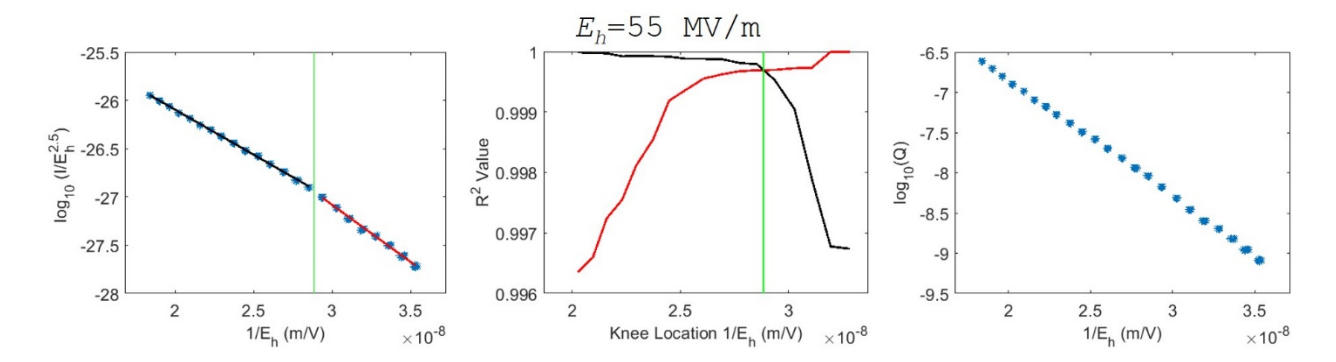


Figure B 9 E<sub>h</sub>-55 MV/m Fowler Nordheim plots, knee point decision plots, and Millikan plots.

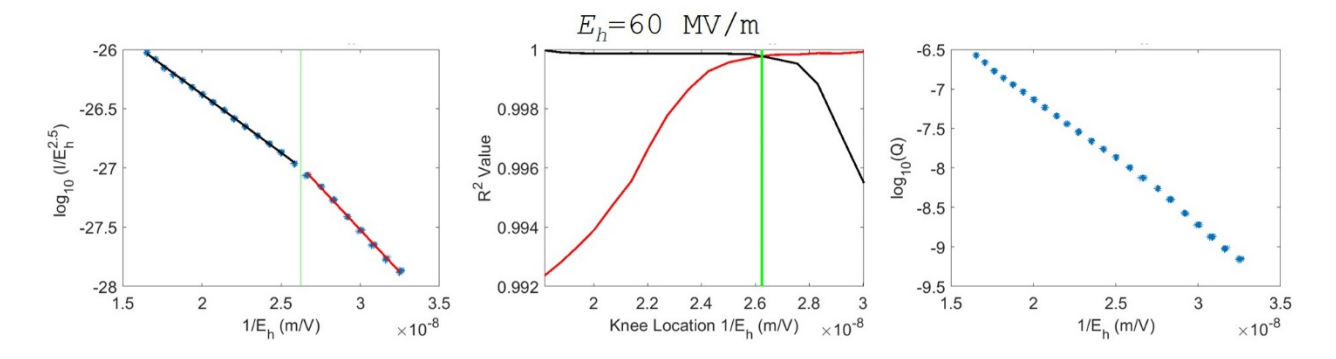


Figure B 10  $E_h$ -60 MV/m Fowler Nordheim plots, knee point decision plots, and Millikan plots.

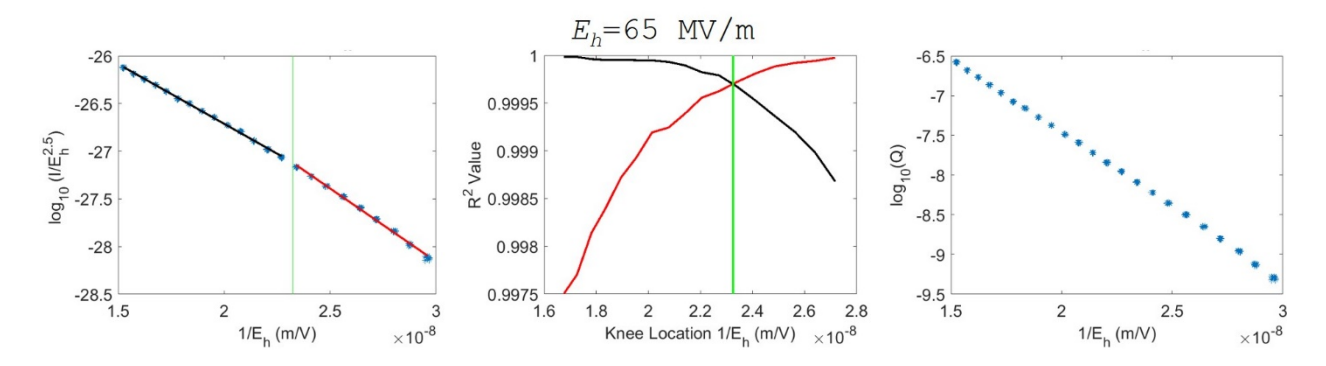


Figure B 11  $E_h$ -65 MV/m Fowler Nordheim plots, knee point decision plots, and Millikan plots.

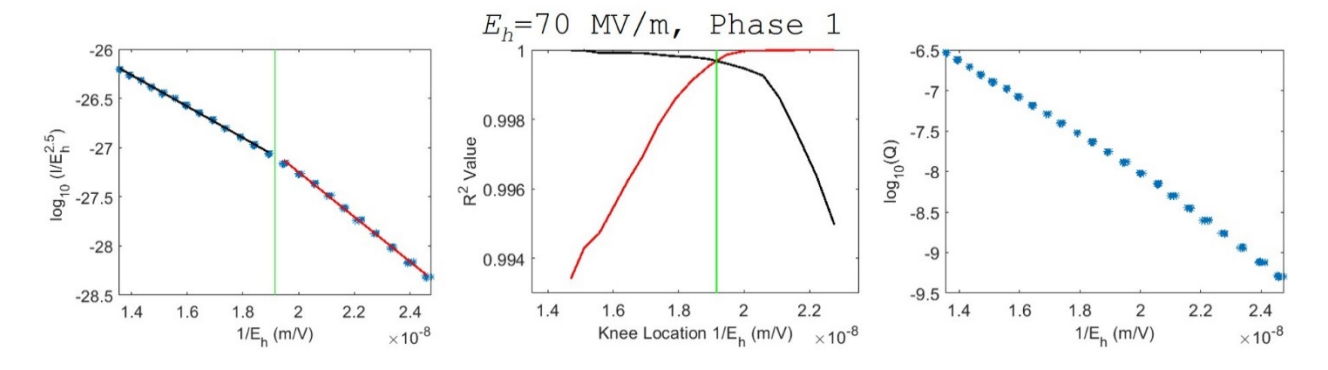


Figure B 12  $E_h$ -70 MV/m Fowler Nordheim plots, knee point decision plots, and Millikan plots.

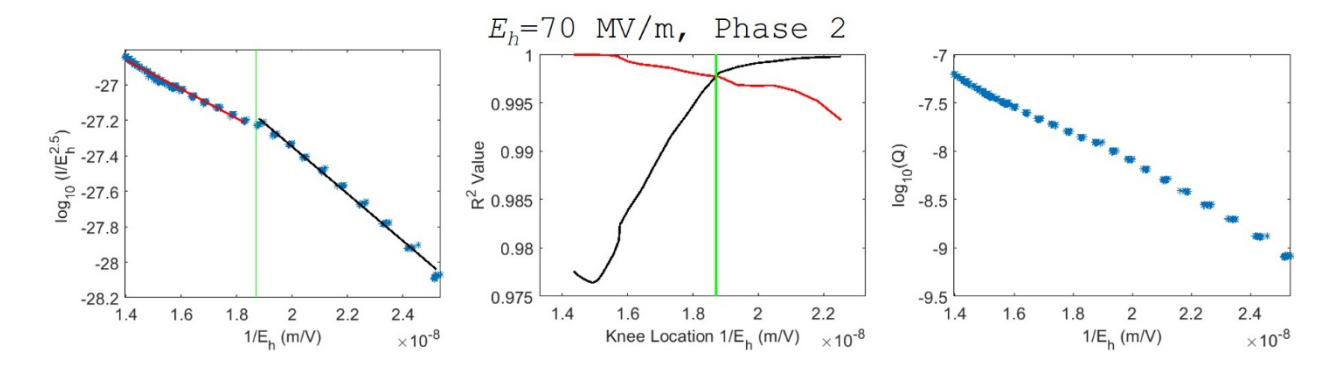


Figure B 13  $E_h$ -70 MV/m Fowler Nordheim plots, knee point decision plots, and Millikan plots.

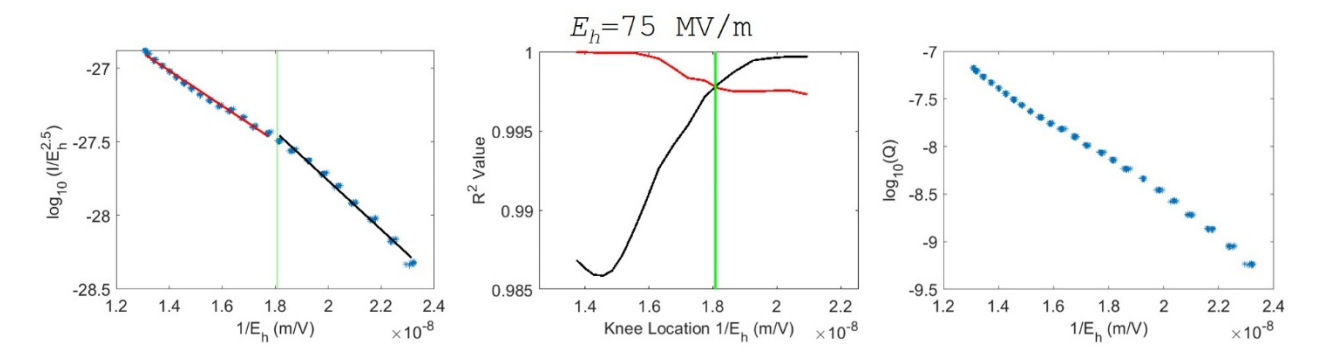


Figure B 14  $E_h$ -75 MV/m Fowler Nordheim plots, knee point decision plots, and Millikan plots.

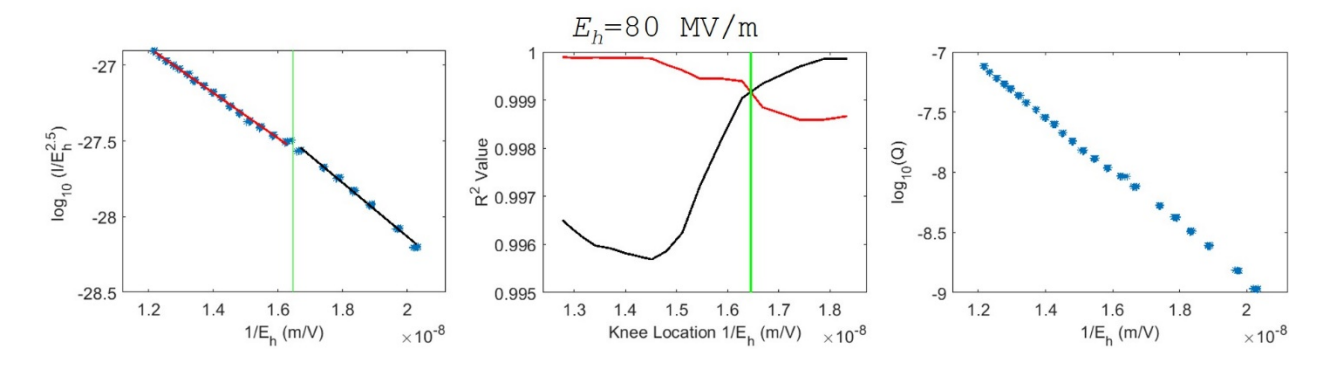


Figure B 15  $E_h$ -80 MV/m Fowler Nordheim plots, knee point decision plots, and Millikan plots.

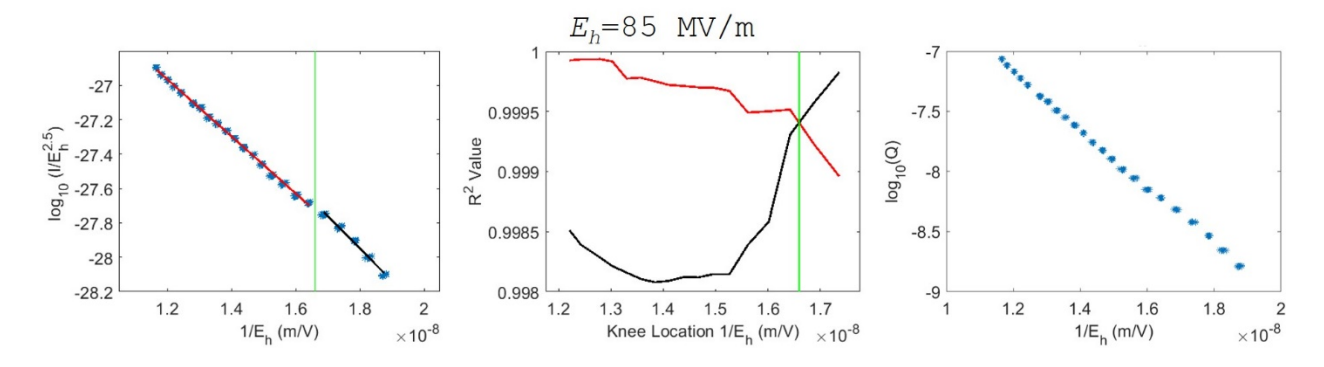


Figure B 16 E<sub>h</sub>-85 MV/m Fowler Nordheim plots, knee point decision plots, and Millikan plots.

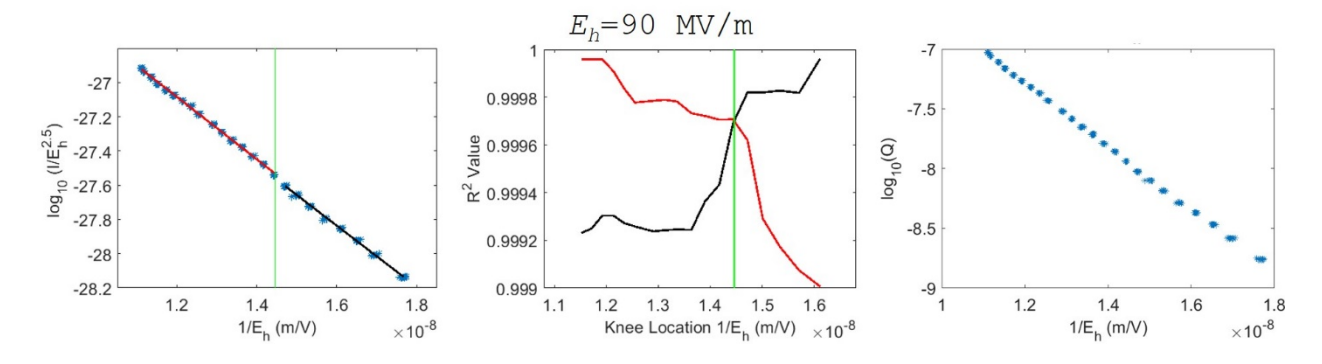


Figure B 17 E<sub>h</sub>-90 MV/m Fowler Nordheim plots, knee point decision plots, and Millikan plots.

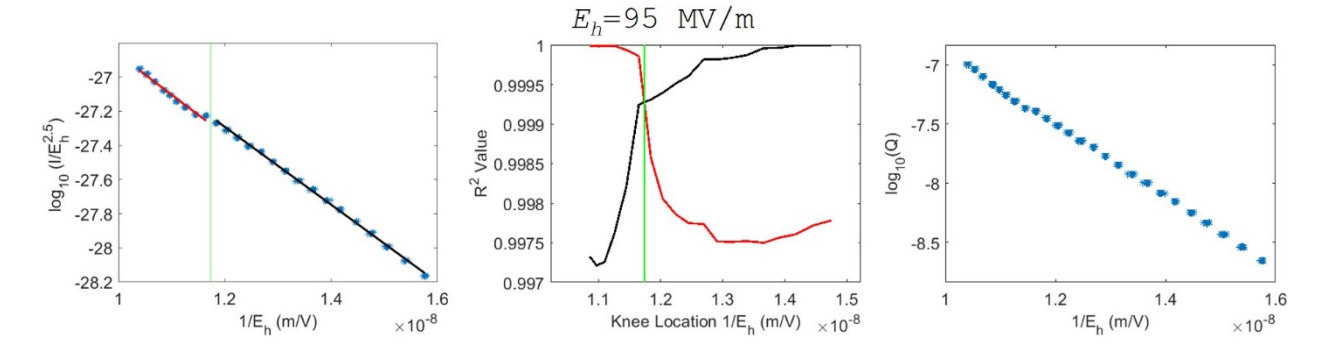


Figure B 18  $E_h$ -95 MV/m Fowler Nordheim plots, knee point decision plots, and Millikan plots.

# **REFERENCES**

#### REFERENCES

- [1] T. Nikhar, R. Rechenberg, M. F. Becker, and S. V. Baryshev, Journal of Applied Physics **128**, 235305 (2020)
- [2] J. Asmussen, T. A. Grotjohn, and T. Schuelke, "Chapter 2 advances in plasma synthesis of uncd films," in Ultananocrystalline Diamond (Second Edition) (Oxford: William Andrew Publishing, 2012) pp. 53–83.
- [3] J. Shao, M. Schneider, G. Chen, T. Nikhar *et. al*, Phys. Rev. Accel. Beams **22**, 123402 (2019)
- [4] E. Jevarjian, M. Schneider, and S. V. Baryshev, arXiv:2009.13046 [physics.acc-ph] (2020),
- [5] G. Chen, G. Adhikari, L. Spentzouris, K. K. Kovi, S. Antipov, C. Jing, W. Andreas Schroeder, and S. V. Baryshev, Applied Physics Letters **114**, 093103 (2019).
- [6] O. Chubenko, S. S. Baturin, K. K. Kovi, A. V. Sumant, and S. V. Baryshev, ACS Applied Materials & Interfaces 9, 33229 (2017).
- [7] T. Y. Posos, S. B. Fairchild, J. Park, and S. V. Baryshev, Journal of Vacuum Science & Technology B **38**, 024006 (2020)
- [8] M. Schneider, E. Jevarjian, J. Shao and S. V. Barnyashev Review of Scientific Instruments **92**, 053305 (2021)
- [9] S. V. Baryshev, E. Wang, C. Jing, V. Jabotinski *et. al*, Applied Physics Letters **118**, 053505 (2021)
- [10] J. Wang and G. Loew, "Tech. Rep. (Stanford Linear Accelerator Center, 1997).
- [11] A. Kyritsakis, M. Veske, K. Eimre, V. Zadin, and F. Djurabekova, "Journal of Physics D: Applied Physics **51**, 225203 (2018).
- [12] S. S. Baturin, T. Nikhar, and S. V. Baryshev, "Journal of Physics D: Applied Physics **52**, 325301 (2019).
- [13] J. W. Luginsland, A. Valfells, and Y. Y. Lau, Applied Physics Letters **69**, 2770 (1996).
- [14] J. P. Barbour, W. W. Dolan, J. K. Trolan, E. E. Martin, and W. P. Dyke, Phys. Rev. **92**, 45 (1953).
- [15] P. Zhang, S. B. Fairchild, T. C. Back, and Y. Luo, AIP Advances 7, 125203 (2017)

- [16] T. Y. Posos, O. Chubenko, and S. V. Baryshev, arXiv:2012.03578 [physics.app-ph] (2020).
- [17] O. Chubenko, S. S. Baturin, and S. V. Baryshev, "Journal of Applied Physics **125**, 205303 (2019).
- [18] J. Shao, J. Shi, S. P. Antipov, S. V. Baryshev et. al, Phys. Rev. Lett. 117, 084801 (2016)
- [19] D. Filippetto, P. Musumeci, M. Zolotorev, and G. Stupakov, Phys. Rev. ST Accel. Beams **17**, 024201 (2014)
- [20] T. Nikhar, S. V. Baryshev, G. Adhikari, and A. W. Schroeder arXiv:2011.00722 [physics.acc-ph] (2020)
- [21] J. P. Barbour, W. W. Dolan, J. K. Trolan, E. E. Martin, and W. P. Dyke, Phys. Rev. **92**, 45 (1953).
- [22] J. W. Lewellen and J. Noonan, Phys. Rev. ST Accel. Beams 8, 033502 (2005).
- [23] X. Li, M. Li, L. Dan, Y. Liu, and C. Tang, Phys. Rev. ST Accel. Beams **16**, 123401 (2013).
- [24] T. van Oudheusden, P. L. E. M. Pasmans, S. B. van der Geer, *et. al*, Phys. Rev. Lett. **105**, 264801 (2010).
- [25] F. Lemery and P. Piot, Phys. Rev. ST Accel. Beams 17, 112804 (2014)
- [26] R. Miller, Y. Y. Lau, and J. H. Booske J. Appl. Phy. **106**, 104903 (2009)
- [27] K. L. Jensen, and A. K. Ganguly, J. Appl. Phy. **73**, 4409 (1993)
- [28] C. H. Moore, A. K. Jindal B. Ezra, et al. (No. SAND2019-10509C). Sandia National Lab. (SNL-NM), Albuquerque, United States (2019)
- [29] J. Shao "investigations on our breakdown phenomenon in high gradient structures" Springer (2018)
- [30] A. Degiovanni, W. Wuensch, J. Navarro J Comparison of the conditioning of high gradient accelerating structures. Phys Rev Accel Beams **19**, 032001 (2016)
- [31] D. Kim, H. L. Andrews, B. K. Choi, E. I. Simakov, 2018 IEEE Advanced Accelerator Concepts Workshop (AAC). (2018)
- [32] J. D. Jarvis, "Development of high-brightness electron sources for free-electron lasers". Vanderbilt University (2009).
- [33] M. Schneider, E. Jevarjian, J. Shao, T. Nikhar, T. Posos, M. Conde, and S. V. Baryshev. Ampere-Class (N)UNCD Field Emission Cathode for RF Guns, in submission as preprint

at arXiv:2102.00071. (2021) (Accepted to Phys. Rev. ST Accel. Beams on 11/15/21 for 12/21 issue)

# CHAPTER 5 DISCUSSION: PATHWAY TOWARDS A FIELD EMISSION ACCELERATOR FACILITY BEAMLINE

The preceding work describes comprehensively the advancements towards describing field emission sources in a variety of different operating conditions for RF injectors and the necessary analysis toolkits and conditioning procedure needed to obtain optimal performance. This discussion section will outline the continuing efforts that should be undertaken based on this thesis to inform the next generation of research projects and theses for future young scientists. The intent of this chapter is to inspire future students to build upon the work presented here with the ultimate goal of developing a large-scale field emission injector capable of producing bright beams with an ultra-high current density source. As the advisor at the beginning of this project stated so elegantly, a person who can understand and design a better source ultimately designs a better accelerator; the rest the beam line is consequential to the source.

The following four sections represent topics that should be of great interest for future PhD research. The preliminary studies that the author has done set up these research opportunities. Each of the following four segments can be taken as an independent study and do not need to be done in any order. These four sections should not be taken as a comprehensive list of the ongoing research needed to achieve the goal of field emission large-scale accelerator facilities.

This chapter will be laid out as the following: Sec 5.1 UNCD cathode engineering, Sec 5.2 Development of field emission diagnostics capable of measuring cathode emittance, Sec 5.3 Development of next generation custom-built field emission injectors beyond L band, and Sec 5.4 Theoretical work beyond Fowler-Nordheim like field emission models.

The next immediate step should be to explore the cathode engineering (Sec. 5.1) described in the conclusion of CH4. This work was originally planned to be part of this thesis but

circumstances, primarily due to constraints caused by the Covid 19 pandemic, prevented completion. There is an opportunity for another student pick up this torch.

#### **5.1 UNCD Cathode Engineering**

As the work in CH4 alluded to, the material science properties of the field emission cathode are the dominant factor determining its electron source characteristics. Therefore, the next step for this research is to vary material parameters in such a way to explore and engineer the ideal cathode materials properties for electron emission sources. This would build off of the work presented in Tanvi Nikhar's thesis which explored the effects of temperature, pressure, and nitrogen concentration on the grain size and diamond-to-graphite ratio of (N)UNCD cathodes [1]. This is important as the grain boundaries determine the number of emitters and thus a cathode with the most grain boundaries per unit area will have the most emissions [2,3]. Note, if the grain boundaries are too small, the ballast resistance will be low and thus will not perform uniform emission as seen in CH 4 [4]. This study should be done by testing a series of (N) UNCD cathodes with a variety of different diamond to graphite ratio. Suggestions for the difference in diamond to graphite ratio are: 5%, 10%, 25%, 50% and 75% graphite. These cathodes would be tested under the same conditions as in CH4.1 to determine the variation in the charge, downstream imaging, number of emitters, and maximum achievable field to determine the ideal diamond to graphite ratio. A second study should test the nitrogen concentration which affects the grain size thus will determine the ideal grain size. It is important to do this at the ACT to make a direct apples-to-apples comparison between the different cathodes.

Following this, the next phase of research would be to test different types of dopant in the UNCD lattice. Currently, the dopant is nitrogen and does not affect the diamond quality but does affect the diamond grain boundaries size and shape. It would be interesting to explore other types

of dopant of UNCD such as boron [5], sulfur [6, 7] to see how the bandgap engineering of these other dopants would change the FEC performance. Currently, nitrogen acts as an N typed dopant and so would sulfur, but boron would be a P typed dopant. There are important dynamics when using a P type or an N typed doping.

#### 5.2 Development of Field Emission Emittance Teststand

A project that can be done in tandem with the material science studies is developing an emittance test stand specially built for field emission sources. The large energy spread of the field emission source, due to the RF energy spread which can be in excess of 20%, has made the ability to measure the emittance of field emission sources in an RF environment nearly impossible up to this point. The brightness results presented earlier in this report used modeling to estimate that the brightness was on the order of  $10^{14}$  A/(m rad)<sup>2</sup> [8]. To experimentally verify these measurements, an emittance test stand needs to be developed. The first step to do this is to develop a pinpoint cathode: a cathode that is very small on the molybdenum substrate of the ACT, on the order of 1 mm. This smaller cathode will produce less charge but most of the electrons will be generated as close on axis as possible. This results in the smallest divergence angle and the best capability to be transported downstream with a fairly small beam radius. Previous research using a 20 mm cathode showed the downstream imaging after focusing of the solenoids resulted in a beam radius on the order of about 2 inches. This is not ideal when using non-solenoid focusing such as a dipole needed to measure the energy spread and emittance of the beam. Preliminary simulations have shown that using a conventional dipole magnet can produce magnetic fields up to about 0.1 T and would have a transmission through the dipole of less than 50 %. Another consequence of this is when one applies a split after the dipole magnet, the energy range of the particles is not mono energetic but instead poly energetic. This must be avoided as,

when measuring the emittance, the energy spread must be approximately mono energetic out of the slit. This allows not only the energy spread to be measured, but also the emittance as a function of the energy spread. This project will include beam dynamics simulations for developing diagnostics capable of dealing with the large energy spread intrinsically associated with RF field emission sources. This project would most likely entail building custom magnetic designs, such as alpha magnets or other variations on that theme, to control the energy spread of the field emission source to operate with low emittance.

#### 5.3 Development of next generation custom-built field emission injectors beyond L band

The capability of the current state-of-the-art L band testing facility beamline in the ACT is maxed out by the experiments presented here. An additional problem with the ACT is that it was never designed to be an injector test stand but was designed as a breakdown imaging test stand. This causes the RF emittance of the ACT to be dominant downstream. The ACT is also a single cell injector, meaning that the emission and the acceleration happen in the same chamber. An advancement on this would be using a multi-cell injector with frequency mixing or gating. By combining a better gun design with higher frequency injectors, the space charge force can also be mitigated at high gradient. This work is already underway as stated previously in the introduction by groups at SLAC [9] and LANL [10, 11]. These new injectors will use the cathodes technology developed in this work.

#### **5.4** Theoretical work beyond Fowler Nordheim

Considering all field emission sources to behave under classical Fowler Nordheim is no longer an appropriate methodology as there are multiple divergences, from ballast resistance as well as the spatio-temporal space charge effects. This work presents the experimental evidence but not theoretical efforts. One of the next works should be a theoretical project to incorporate

other known models of field emission physics such as Murphy-Good for temperature dependence, and the Stratton's equations for semiconductor effects [12,13]. Beyond the known models, there is additional effects that must be considered such as the skin depth, the surface potential, as well as accounting for non-uniform work function across the cathode surface.

More work should also be done on deriving the three-dimensional Child-Langmuir law and defining an analytical expression for the field enhancement factor that considers the materials parameters as well as the geometry. This will greatly enhance theoretical validity of experimental results in current cutting-edge field emission research and is needed for advanced accelerator concepts.

## 5.5 Field emission cathodes for advanced accelerator applications

The preceding sections on field emission technology are the first steps toward wide adoption at large-scale accelerator facilities. Ampere-class UNCD opens the door to being able to derive the bright beam field emission sources with high current density needed for fusion engines and compact medical isotope and radiotherapy accelerators [8]. DFEA work is already being considered to produce intrinsically patterned beams for emittance exchange beamlines [14]. High current density sources are also be needed for the next generation of high-power terahertz radiation sources, with a preliminary study completed that can be seen in Ref [15]. This thesis presents a roadmap of feasible field emission technology development over the next 10 years to enable field emission injectors to be an integral part of the next generation of accelerators at national or international facilities.

# **REFERENCES**

#### REFERENCES

- [1] T. Nikhar, Revisiting Effects of Nitrogen Incorporation and Graphitization on Conductivity
- [2] L. Y. Zhou, J. Shi, D. Wang, W. Gai, H. Chen, Proceeding from 8th Int. IPAC'17 (2017)
- [3] F. Sakamoto, M. Uesaka, K. Dobashi, A. Fukasawa, T. Yamamoto, et al., J. Korean Phys. Soc. 49, 286 (2006)
- [4] J. D. Jarvis, "Development of high-brightness electron sources for free-electron lasers". Vanderbilt University (2009).
- [5] D. Y. Kim, B. Merzougui, and G. M. Swain. Chemistry of Materials, **21** (13), 2705 (2009).
- [6] S. Koizumi, T. Teraji, and H. Kanda, Diamond Relat. Mater. 9, 935 (2000)
- [7] I. Sakaguchi, M. N-Gamo, Y. Kikuchi, E. Yasu, and H. Haneda, Phys. Rev. B **60**, 2139 (1999)
- [8] M. Schneider, E. Jevarjian, T. Nikhar, T. Y. Posos, W. Liu, J. Shao, S. V. Baryshev available as preprint arXiv:2102.00071(2020)
- [9] S. M. Lewis, A THz-Driven Electron Gun, thesis University of California at Berkeley (2020)
- [10] D. V. Gorelov, R. L. Fleming, S. K. Lawrence, J. W. Lewellen *et al* Proceedings from 12<sup>th</sup> International Particle Accelerator Conference (IPAC2021), Campinas, SP, Brazil (2021)
- [11] The International Linear Collider technical design report (2013) Technical report, ILC
- [12] E. L. Murphey and R. H. Good, Physical Review **12** (6) 1464
- [13] O. Chubenko, S. S. Baturin, and S. V. Baryshev, Journal of Applied Physics **125**, 205303 (2019).
- [14] G. Ha, J. Power, M. Conde, D. Doran, et *al.* In Proceedings of 38th International Free Electron Laser Conference (2018)
- [15] M. E. Schneider, E. Jevarjian, B. Sims, A. Altmark, B. v. der Geer, S. V. Baryshev available as preprint arXiv: 2107.02855 (2021)